3-30-2010

Corrosion of Dual Coated Reinforcing Steel with Through-Polymer Breaks in Simulated Concrete Pore Solution

Adrienne Accardi
University of South Florida

Corrosion of Dual Coated Reinforcing Steel with Through-Polymer Breaks in Simulated Concrete Pore Solution

by

Adrienne Accardi

A thesis submitted in partial fulfillment
of the requirements for the degree of
Masters of Science in Mechanical Engineering
Department of Mechanical Engineering
College of Engineering
University of South Florida

Major Professor: Alberto A. Sagüés, Ph.D.
Delcie Durham, Ph.D.
Autar Kaw, Ph.D.

Date of Approval:
March 30, 2010

Key Words: Zinc, Impedance, Disbondment, Epoxy, Polarization

Acknowledgements

The author would like to sincerely thank Dr. Alberto Sagüés for his continued guidance and encouragement during this project. She would also like to thank the members of the committee, Dr. Delcie Durham and Dr. Autar Kaw, for their valuable suggestions.

The author would like to thank her colleagues in the Corrosion Lab, Ezeddin Busba, Margareth Dugarte, Mersedeh Akhoondan, and Andrea Sanchez for providing such a wonderful support system during times of stress. The author would like to thank Kingsley Lau especially for providing valuable insight into the project and guidance since the author first came to work in the lab as an undergraduate.

The author would like to thank her family and wonderful fiancé Alex Gady for being patient while long nights were spent at the lab. They provided understanding and encouragement that allowed for the completion of this project.

Finally, the author would like to thank Gerdau Ameristeel for the financial support that made this project possible. The findings and opinions presented in the manuscript are those of the author and not necessarily those of the sponsoring organizations.

Table of Contents

List of Tables

List of Figures

Corrosion of Dual Coated Reinforcing Steel with Through-Polymer Breaks in Simulated Concrete Pore Solution

Adrienne Accardi

ABSTRACT

This investigation is an examination of the behavior of dual coated reinforcing steel (DCR) with defects in the polymer coating exposing the only zinc layer in simulated concrete pore solution with and without chlorides. The intentional defects simulated the condition typically experienced by the rebar in service. Specimens were tested at open circuit potential, +100 mV, -500 mV, and -1000 mV for 30 to 100 days. The results were compared with that from previous DCR investigation with to-steel defects and epoxy-coated rebar (ECR). DCR with to-zinc defects had extensive corrosion damage when under strong anodic polarization and exposed to chlorides and was similar to that seen for DCR with to steel defects. The freely corroding (OCP) to-zinc DCR specimens in solutions both with and with no-chlorides experienced initially very active dissolution which ended after ~1 day. The zinc exposed at the coating breaks was not completely consumed even after 100 days and there was no visible corrosion product accumulation. This may be due to the formation of a calcium hydroxyzincate passive film and shows that the zinc passivates in alkaline solutions without the benefit of a crevice environment. The DCR with to-steel defects and the DCR with to-zinc defects had similar amounts of

disbondment for all test conditions. Notable disbondment was seen only in highly anodic polarization regime with chlorides and was due to large amounts of solid corrosion product formation. These results suggest then that the overall process of zinc wastage in DCR in concrete pore water is not likely to be rapid, which would be beneficial to extending the period in which the barrier and galvanic properties of the zinc are maintained.

Chapter 1
Introduction

Corrosion is a significant concern to today's economy, costing the United States $137.9 billion in 2002. This cost can be broken down into five industry sectors as is shown in Figure 1. Infrastructure alone costs $22.6 billion which is 16.4% of the total cost. Of that, $8.3 billion (37%) is spent to repair corrosion in highway bridges. The indirect costs due to traffic delays and lost productivity caused by bridge repairs are estimated to be 10 times that of the direct cost of corrosion repairs. Of the estimated 583,000 bridges in the United States, 235,000 (~40%) are steel reinforced concrete bridges and ~15% of these have been determined to be structurally deficient due to corrosion related problems (Koch, et al. 2002). Developing corrosion resistant reinforcing steel would have a large impact on reducing the amount spent to repair corrosion damage in bridges.

Reinforced Concrete

Concrete is a commonly used building material worldwide. It is typically composed of mortar and aggregate. Although it can handle large compressive loads, it is not strong in tension. The concrete must be reinforced in order to handle tensile and shear forces. Steel reinforcing bar, or rebar, is embedded in the concrete to handle these loads. Rebar is typically made of plain carbon steel (e.g. 0.5 wt% of carbon). In order to transfer the loads from the concrete to the steel reinforcement, the rebar must be bonded to the concrete. For that reason, most rebar in use is ribbed to provide a stronger mechanical bond than steel rod to concrete (Parker 1968).

Corrosion of Steel in Concrete

Passivity is defined by (Fontana and Greene 1978) as the loss of reactivity of a metal under particular environmental conditions. This is typically due to the formation of a thin oxide surface film that protects the metal surface from corrosion. This film is usually stable at high pH values ($9 < pH < 14.5$). Concrete pore water tends to have concentrations of calcium, sodium, and potassium oxides that combine with water to form hydroxides, creating a high pH (minimum of ~12.5 for Portland cement (Derucher, Ezeldin, and Korfiatis 1994)) environment (Broomfield 1998). As a result, steel is typically passive in concrete.

Two environmental changes can break down the passive film: carbonation of the concrete and chloride attack. Carbonation of the concrete can decrease the pH to 8 or 9 causing the passive film to become unstable and decompose. Chloride ions do not seriously affect the pH of the pore water, but instead attack the passive layer and accelerate the corrosion process (Derucher, Ezeldin, and Korfiatis 1994) (Broomfield 1998). Chloride concentration above a threshold value, C_T, typically of more that 0.2% by mass of Portland cement may, be enough to destroy the protective film when the pH is greater than 11.5 (Derucher, Ezeldin, and Korfiatis 1994).

Reinforcing steel in bridges pilings in marine environments or bridge decks subjected to seasonal deicing salts is susceptible to corrosion due to the penetration of chloride ions into the concrete and ensuing passivity breakdown. Chloride ions usually travel slowly by diffusion through the concrete or more quickly along cracks in the concrete.

The corrosion process, after the breakdown of the passive layer, is comprised of two simultaneous reactions: the oxidation or anodic reaction and the reduction or cathodic reaction. The oxidation reaction produces electrons while the reduction reaction consumes electrons. These two reactions must occur at the same rate and time on the surface of the metal for corrosion to take place. The anodic reaction, which consumes the

iron that makes up ~97% of the reinforcing steel, can be expressed as (Fontana and Greene 1978):

$$Fe \rightarrow Fe^{2+} + 2e \qquad \text{(Eq. 1)}$$

The equation for the cathodic reaction that typically takes place in high pH solutions such as concrete pore water is:

$$O_2 + 2H_2O + 4e \rightarrow 4OH^- \qquad \text{(Eq. 2)}$$

These reactions can be combined as:

$$2Fe + 2H_2O + O_2 \rightarrow 2Fe(OH)_2 \qquad \text{(Eq. 3)}$$

where $Fe(OH)_2$ is a corrosion product (Fontana and Greene 1978). The $Fe(OH)_2$ can be oxidized further to $Fe(OH)_3$, the corrosion product typically referred to as rust. These corrosion products are more voluminous than the steel (up to 600% of the original metal volume (Derucher, Ezeldin, and Korfiatis 1994)). This increase in volume causes tensile stresses that, in turn, cause the concrete to crack and spall resulting in the loss of structural integrity. It is noted that very small amounts (~3 to 4% reduction of cross-sectional area of the rebar (T. Ohta 1991)) of corrosion can cause enough internal stress to crack the concrete. Hence, it is very important to minimize the corrosion of reinforcing steel.

Corrosion Control

Many systems have been developed to prevent or slow down the corrosion of steel in concrete. Some of these prevention systems concentrate on the concrete condition. An increase in the thickness of the concrete cover forces chloride ions to travel through more concrete before reaching the steel. Also, using a lower water to cement ratio (to as little as 0.32) minimizes the connectivity of the concrete pore network. These two practices combined with following proper casting and curing specifications can delay

corrosion initiation by slowing down chloride transport and consequently extending the period of time required to increase the Cl^- concentration up to the C_T of the rebar surface. Physical barrier, such as painted coatings, are sometimes added to the surface of the concrete to block chloride ions from diffusing through the concrete. Corrosion inhibitors that increase C_T can be added to the concrete mix and chemically delay the onset of corrosion.

Cathodic protection is another commonly used corrosion control system. This system works by supplying the metal intended to be protected with electrons (cathodic polarization), which hinders the metal dissolution described in Eq. 1. Two types of cathodic protection are used: impressed current and sacrificial anode. Both systems act to drive the potential of the protected metal to a more negative value, creating cathodic polarization. The sacrificial anode system relies on a galvanic couple where the protected metal is electrically connected to a metal that is more susceptible to corrosion. This metal corrodes, sending electrons to the protected metal. Zinc and magnesium are commonly used materials for anodes. This system operates until the anode is consumed (Fontana and Greene 1978).

Finally, many types of corrosion resistant reinforcing steels are being increasingly used. These include but are not limited to stainless steel, stainless steel clad carbon steel, galvanized and epoxy coated rebar.

Epoxy-Coated Reinforcing Steel

Epoxy-coated reinforcing steel, or ECR, is a surface-abraded carbon steel rebar coated with a layer of fusion bonded epoxy polymer that acts as a physical barrier between the steel and the environment. Control of coating imperfections is essential for adequate performance (Manning 1996) (Yeomans 1994). The product has been in use for almost 40 years, being introduced in the 1970's (Sagüés 1989), typically in environments where chloride induced corrosion is likely.

ECR has, with relatively few exceptions, been reported to perform well in bridge decks where deicing salts are used. Bridge decks were reported to be in good overall condition, with corrosion seen only in cracked concrete locations (Smith and Virmani 1996) (Fanous and Wu 2000). However, it was reported that coating adhesion loss could occur in as little as four years after construction, well before chloride ions reach the rebar (Pyć, Weyers, Weyers, Mokarem, and Zemajtis 2000). This adhesion loss makes the ECR vulnerable to corrosion when the chloride threshold is reached. It was shown that this disbondment occurs in good quality concrete with ECR that complies with specifications (Pyć, Weyers, Weyers, Mokarem, and Zemajtis 2000).

There have been notable corrosion incidents in bridge substructure exposed to a marine environment affecting several major bridges. ECR was especially susceptible in the tidal zone where chloride concentrations tend to be higher (Griffith and Laylor 1999). This is especially evident in the Florida Keys were several bridges experienced severe corrosion damage relatively shortly after construction (~6 years) and continued to deteriorate at ~0.1 spall per bent (pier) per year for 25 additional years with no indication of slowing down (Sagüés, Powers and Kessler 2009). It was noted in the literature that in instances where ECR performed well, concrete cover was also deeper and the concrete quality was better, which would increase the time to corrosion initiation greatly regardless of the type of rebar (Manning 1996) (Clear 1992). There is an instance where ECR performed well in a marine substructure, despite high chloride concentration. (Cui, Lawler, and Krauss 2007) reported on a bridge built in 1987 that had no evidence of spalling or large spread corrosion even though the chloride concentration was on average greater than 0.079 % per weight of concrete, the epoxy coating was of substandard thickness, and adhesion loss was present (Cui, Lawler, and Krauss 2007). This report also stated that one ECR sample contained corrosion, but the chloride concentration at this site was 0.251 % per weight of concrete, which in ~10 pcy, a relatively high concentration (Cui, Lawler, and Krauss 2007).

Typical failure mechanisms of ECR seen in the field are loss of coating adhesion and macrocell formation. The loss of coating adhesion, which is caused by water absorption by the coating (Manning 196), anodic blistering, and cathodic delamination (Nguyen and Martin 1996) (Nguyen and Martin 2004), resulted in coating that blistered and cracked (Clear 1992). This was seen in northern and southern United States bridge decks and southern bridge substructures with bars that had passed inspection. Macrocell formation most often occurred in bars with coating holidays and larger damage, with some already experiencing undercoating corrosion (Clear 1992).

Galvanized Reinforcing Steel

Galvanized reinforcing steel is a carbon steel rebar coated with a layer of zinc and has been used as a means of corrosion protection since the 1930's (Yeomans 2004). The zinc is applied in a variety of ways including hot-dipping, thermal spraying, electro-deposition, and diffusion. Hot-dipping, where the zinc becomes metallurgically bonded to the steel (Langill and Dugan 2004), is most commonly used for the manufacture of galvanized rebar.

During the hot-dipping process, several zinc-steel alloy layers form on the surface of the carbon steel rebar. Typically four layers develop: gamma (inner layer), delta, zeta, and eta (outer layer), however, all of the layers are not created every time. The layers are shown in Figure 2. The number of layers as well as the thickness of the layers depends on several factors including the composition of the base carbon steel, the surface texture of the base steel, the temperature of the zinc bath, the amount of time the rebar is immersed in the zinc bath, and the speed at which the rebar is removed from the zinc bath. The layers and their characteristics are listed in Table 1. Note that as the layer gets closer to the steel, the more iron that is present in the alloy. The amount of corrosion protection is typically dependent on the zinc coating thickness, rather than the crystal structure of the alloy layers (Langill and Dugan 2004).

Galvanized steel has been shown to withstand chloride concentration 2.5 times that of bare steel rebar and delay the time to corrosion by 4-5 times (Yeomans 2004). Despite this, there are notable examples where galvanized rebar has not performed well in the field. (Pianca and Schell 2005) reported that there was significant corrosion related concrete damage in three Ontario bridge decks when the C_T for black steel was surpassed.

The zinc coating acts as both a sacrificial anode, much like a cathodic protection system, and a physical barrier. The zinc corrodes over time and the rate of corrosion depends on the pH of the environment. Zinc is relatively stable at pH values between 8 and 12.5, as seen in the Pourbaix diagram, Figure 4. Above pH 12.5 the corrosion rate of the zinc increase as the pH increases and below pH 6 the corrosion rate of zinc increases as the pH decreases. This is illustrated in Figure 3, which shows the corrosion rate of zinc versus pH. At a certain range of pH values, zinc corrosion products can act as a physical barrier, creating a passive layer. This typically occurs at pH values between 12.5 and 13.3. At pH values above 13.3, the corrosion products tend to create larger crystals which do not form a cohesive passive film. Therefore, at pH values above 13.3, the zinc corrodes readily, eventually leaving the steel unprotected (Bentur, Diamond, and Berke 1997). Other authors report a transition pH of ~13.1 (Andrade and Alonso 2004).

When galvanized steel comes into contact with freshly cast concrete, as in during the construction process of reinforced concrete structures, typically less than ~10um of the outermost eta zinc layer corrodes in a short time, and then corrosion tends to stop. Zinc oxide product forms first (Andrade and Alonso 2004):

$$Zn + 2OH^- \rightarrow ZnO + H_2O + 2e^- \quad \text{(Eq. 4)}$$

and is then further oxidized into zinc hydroxide (Andrade and Alonso 2004):

$$ZnO + H_2O + 2OH^- \rightarrow Zn(OH)_4^{2-} \quad \text{(Eq. 5)}$$

Both zinc oxide and zinc hydroxide are white, powdery corrosion products and do not form a protective oxide layer. However, in a strong alkaline environment where calcium is present, such as concrete pore water, the zinc hydroxide further oxidizes to calcium hydroxyzincate:

$$2Zn(OH)_4^{2-} + Ca^{2+} + 2H_2O \rightarrow Ca(Zn(OH)_3)_2 \cdot 2H_2O + 2OH^- \qquad \text{(Eq. 6)}$$

which forms a passive oxide layer on the zinc surface. This passive layer increases the C_T of the zinc to about twice that of carbon steel (Andrade and Alonso 2004).

When a structure with galvanized rebar is placed in service with exposure to external chloride and the C_T of the zinc is eventually reached, breakdown of the zinc passive film takes place. The zinc oxides that form then tend to be less voluminous than the iron oxides formed when plain carbon steel rebar first corrodes and, therefore, create less of the internal stresses that would to cracks and spalls in the concrete. Thus, at least the early stages of galvanized rebar active corrosion are expected to be less damaging to the concrete structure than plain carbon steel rebar. It is noted that this interpretation has been disputed by (Hime and Machin 1993). Their investigation concluded that in concrete with large chloride concentration, another zinc corrosion product, zinc hydroxychloride II ($Zn_5(OH)_8Cl_2 * H_2O$), formed on galvanized bar which was more voluminous than iron oxides, expanding to 3.5 times the volume of original zinc. The authors concluded that this may be the reason for varying reports, noted earlier, of the behavior of galvanized rebar in the field.

Dual Coated Reinforcing Steel

Dual coated reinforcing steel, or DCR, has been developed relatively recently. DCR is composed of a carbon steel rebar core with a thermally sprayed zinc layer and a polymer epoxy coating over the zinc. ASTM Standard A1055 (2008) states that the zinc layer must be >0.035 mm and the total coating thickness (zinc and epoxy polymer) must

be between 0.175 and 0.4 mm. Several corrosion evaluations of DCR have been conducted, including tests in concrete and tests in simulated concrete pore solution (SPS).

Tests in concrete (Clemeña 2003), which followed the ASTM G-109 standard, resulted in estimated time to corrosion of ~530 days for specimens with defects extending through the polymer and zinc layers exposing steel, ~640 days for specimens with defects exposing only the zinc layer and >~740 days for specimens with no intentional defects (Clemeña 2003). The lowest time to corrosion for DCR was ~6 times that for black bar. The estimated C_T noted in that investigation was ~4460 ppm for specimens with defects exposing steel and >~5200 ppm for specimens with no intentional defects (Clemeña 2003). The lowest C_T for DCR was ~9 times that of black bar. Other tests in concrete (Darwin, Browning, Locke, and Nguyen 2007) concluded that the zinc acted as a sacrificial barrier in both cracked and uncracked concrete. This was true for bars with defects extending through the epoxy and defects extending through both epoxy and zinc. The conclusions for this test, however are preliminary and the authors are awaiting the completion of additional tests to evaluate the long term performance of DCR (Darwin, Browning, Locke, and Nguyen 2007).

The experiments conducted in SPS solution (Lau and Sagüés 2009) evaluated DCR specimens with defects through the epoxy and zinc layers, directly exposing steel and ECR specimens with defects exposing steel. Frequent reference is made to this investigation in the following for comparison purposes and detailed results of that investigation are presented in detail in Table 4. The conclusions from that investigation are as follows (Lau and Sagüés 2009):

- The DCR coating adhesion depended on the strength of the zinc layer. For all polarization regimes and solutions, the adhesion loss experienced by DCR was less than or equal to that experienced by ECR.
- ECR and DCR both experienced extensive corrosion for the +100 mV chloride exposure tests; however the damage to ECR was greater. This

was concluded to be due to greater amounts of corrosion product produced by ECR causing more coating disbondment.

- The ECR open circuit chloride exposure specimens developed a negative potential and corrosion product. The DCR open circuit potential, OCP, specimens in both solutions began at very negative potentials which increased to ~-400 mV. They developed no visible corrosion products. The lack of steel corrosion was concluded to be due to corrosion prevention from the galvanic coupling of the steel in the defect and the rim of zinc around the edge of the defect.
- For OCP DCR in both solutions, the zinc was consumed very actively upon immersion and then slowed consumption to a low rate.
- DCR with no-chloride exposure at medium (-500 mV) and strong (-1000 mV) cathodic polarization produced cathodic current less than those for ECR. It was concluded that DCR under these polarization regimes would not support corrosion macrocells greater than ECR.

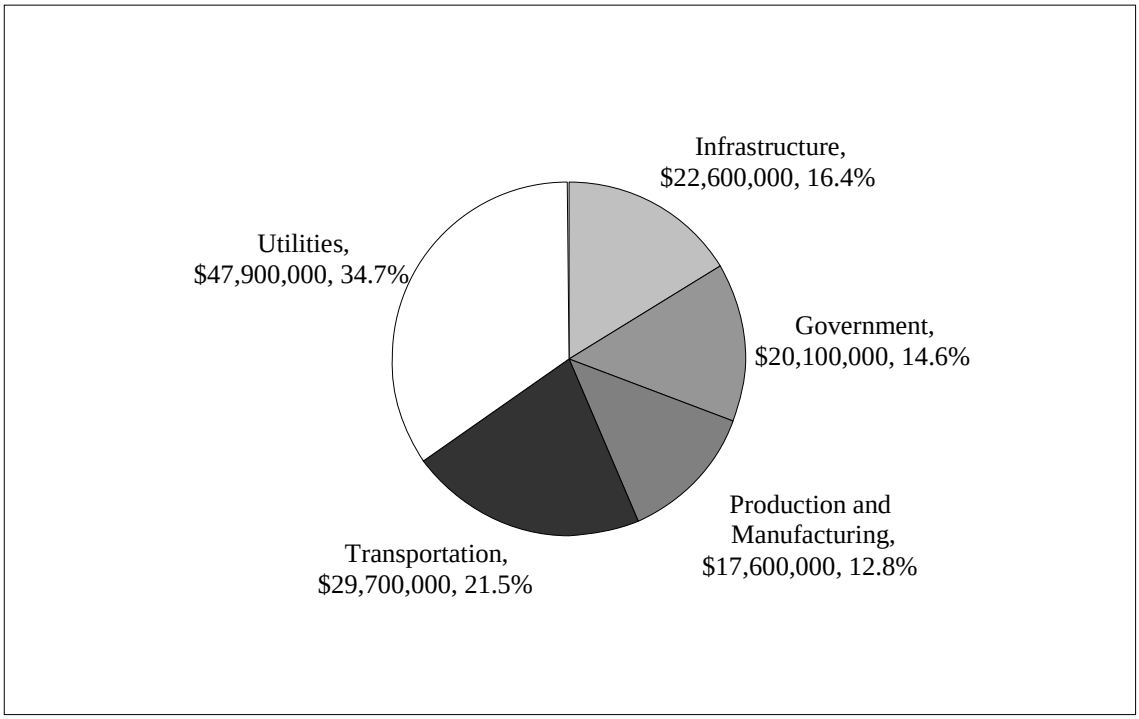

Figure 1: Annual Cost of Corrosion for the Five Government Sections. (Adapted from (Koch, et al. 2002).)

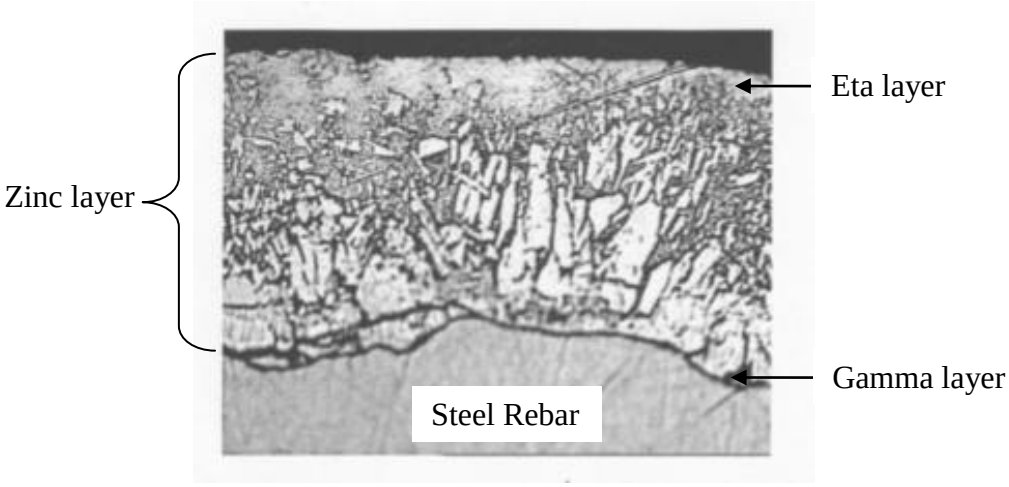

Figure 2: Microstructure of the Zinc Layers of Galvanized Rebar. This sample was exposed to wet concrete for 2 years. The picture is 175 µm in height. (Adapted from Moreno and Sagüés 1996)

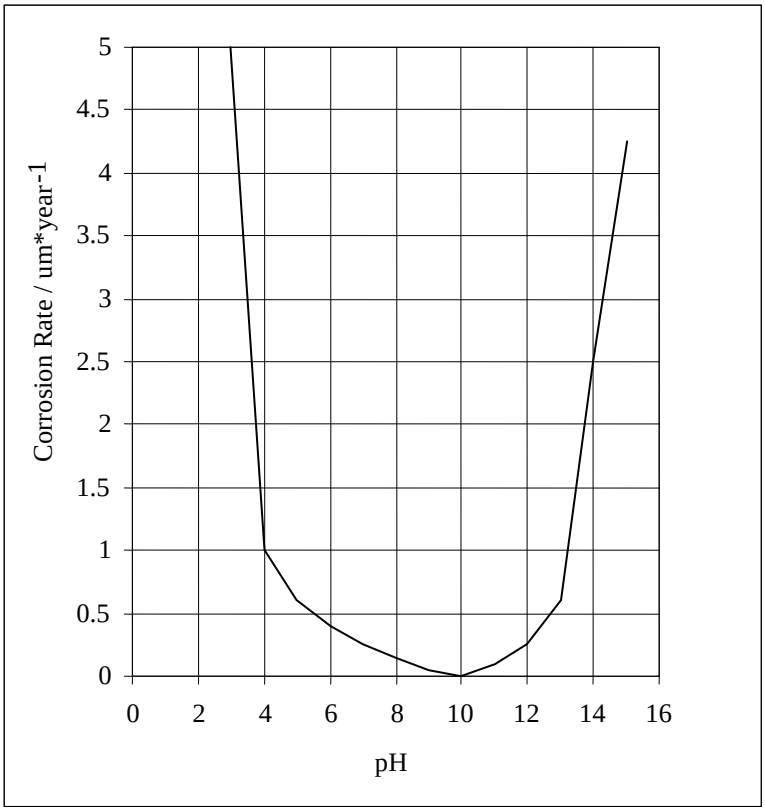

Figure 3: Dependence of Corrosion Rate of Zinc on pH. (Adapted from (Bentur, Diamond, and Berke 1997).)

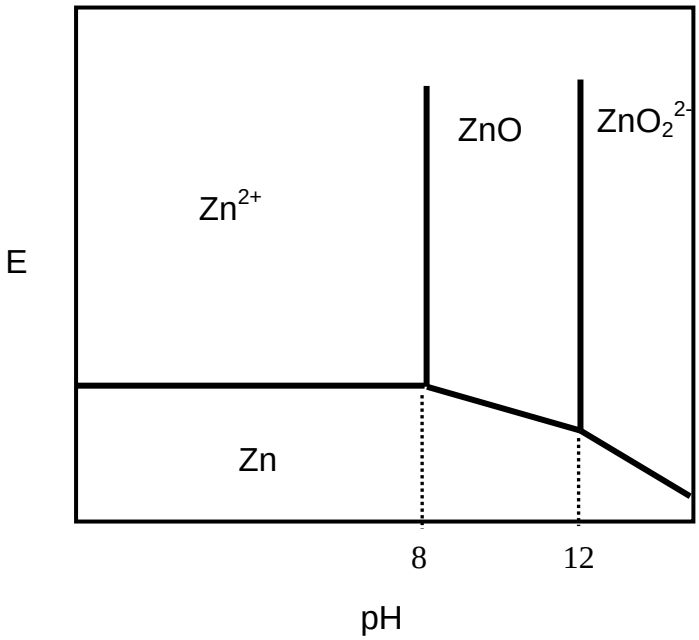

Figure 4: Pourbaix Diagram for Zinc. (Adapted from (Pourbaix 1974).)

Table 1: Hot-Dipped Galvanized Rebar Coating Layers and Characteristics. (Adapted from (Langill and Dugan 2004))

Layer	Alloy	Composition (%Fe)	Melting Point (^{o}C)	Crystal Structure	Hardness (DPN)	Characteristics
Eta	Zinc	0.03	419	Hexagonal	70-72	Soft, ductile
Zeta	$FeZn_{13}$	5.7-6.3	530	Monoclinic	175-185	Hard, brittle
Delta	$FeZn_{7}$	7-11	530-670	Hexagonal	240-300	Ductile
Gamma	$Fe_{3}Zn_{10}$	20-27	670-780	Cubic	N/A	Thin, hard, brittle
Base Carbon Steel	Carbon Steel	98-99	~1530	Cubic	150-175	Ductile

Chapter 2
Objective and Approach

Objectives

The objectives of this investigation are:

- To evaluate the corrosion behavior of DCR with defects simulating moderate coating damage most likely to be seen in the field.
- To compare the behavior of DCR with moderate coating damage to that previously observed with severely damaged DCR and ECR.

Experimental Approach

To address the first objective, the corrosion behavior of DCR was evaluated through electrochemical and coating adhesion loss testing. Electrochemical tests were conducted over a period of time at various polarization values. Two testing solutions were used, simulated concrete pore solution and simulated concrete pore solution with NaCl addition. Adhesion loss testing was conducted after the DCR had been immersed in solution and polarized for the period of time. Intentional defects, which extended through the polymer coating exposing the zinc layer, were made in the DCR. These defects represent typical coating damage seen on DCR where normal field handling practices are followed. Supplemental exposure tests were run to ensure the reproducibility of the OCP no-chloride results.

For the second objective, the results were compared with those from a previous investigation conducted to explore the behavior of DCR and ECR with extensive coating damage, simulated by intentional defects that extended through polymer and zinc coating layers or the polymer layer, respectively, to expose steel.

Chapter 3
Methodology

Dual coated rebar stock, 1.6 cm in diameter, was obtained from the manufacturer and test sample bars, 23 cm in length, were cut from this stock. The two cut ends of the sample bar were patched with Valspar Yellowbar Touchup Components A and B (part number 920Y966) an epoxy patch compound provided by the DCR manufacturer. The two components were mixed together in equal parts, as per the instructions. The coating quality of these samples was assessed through coating thickness (polymer and zinc) measurements performed with an Elektro-Physik S/N Mikrotest magnetic coating thickness gage (model number 014400) and the presence of holidays and mechanical coating damage was assessed by visual observation and the use of a Tinker and Razor Model M-1 holiday detector. For the holiday detection, a small sponge wetted in water with Kodak Photo-Flo 200, as suggested on the Tinker and Razor website, was attached to a detecting wand. The wand with sponge was passed along the bar from top to bottom four times, rotating the bar 90^{o} each time. If a holiday was detected, the detector would beep. This resulted in a failure and that bar was not used in testing. An exception was made if the holiday was detected along the top edge of the sample where the end of the bar had been patched with polymer epoxy patch compound. In this case, a second thin coat of epoxy polymer was added to the top of the bar and was then retested for holidays. Bars that passed were used in testing. If it failed after repatching, the bar was not used for testing. The magnetic gage was used by placing the magnetic probe on the surface of the bar, between ribs. The measuring wheel was turned slowly until the magnet no longer held onto the surface. The thickness measurement denoted by the wheel was then recorded. Coating thickness measurements were made in triplicate. The average of the three measurements was calculated and taken as the coating thickness at that particular site. Intentional coating defects, 1.6 mm in diameter, were introduced by locally melting

the polymer and mechanically removing it with a 40 watt soldering iron. This procedure ensured that the defect extended only through the polymer coating layer to expose the zinc layer, but without melting or removing it. Analysis with an optical microscope and metallographic analysis (Figure 5) verified that this method removed nearly all of the epoxy layer with about 2/3 of the zinc exposed and the rest of the defect area covered only by a thin epoxy residue. Defects were located between the ribs of the reinforcing bar. Each bar sample had eight defects, four defects on two opposing sides of the bar. Each defect had an area of ~2 mm^2, so the total exposed area of metal per bar was ~0.16 cm^2. One end of the bar was cast to a depth of 2 cm into a metallographic epoxy cylindrical base. The purpose of this epoxy base was to protect the end from corrosion and to serve as a way for the bar to stand upright. A 6-32 stainless steel screw was tapped on the other end of the bar to serve as an electrical connection. Connectivity was tested with a multimeter between the screw and all intentional defects. A diagram of the sample bars is presented in Figure 6.

Exposure Testing

All potentials in this document are given in the saturated calomel electrode (SCE) scale.

The DCR sample bars were exposed to two simulated concrete pore solutions (SPS): one contained a 3.5 % by weight addition of NaCl and the other had no NaCl addition. The chemical composition of both solutions is presented in Table 1. The samples were partially immersed with the top ~2 cm, including the stainless steel screw, above the solution, leaving ~19cm, including all eight defects, to be exposed to solution. The test tanks were made two 10 gallon glass fish tanks, each containing 8 samples and ~26 L of solution each. The tanks were topped with a Plexiglas cover sealed with weather stripping in order to prevent carbonation of the solution. The solution was kept at lab ambient temperature, 22 ± 2 °C.

Four polarization regimes were used for each sample group: +100 mV, -500 mV, -1000 mV, and open circuit potential (OCP). These values are comparable to those used in similar tests (Lau and Sagüés 2009). These experiments were conducted with duplicate specimens. These potentials were maintained with a multi-potentiostat, capable of maintaining multiple polarization values, and measured regularly with a SCE that was temporarily inserted into the tank. The potentiostat works by maintaining a specified potential difference between the working and reference electrode with an operational amplifier (Orazem and Tribollet 2008). In a multi-potentiostat, several operational amplifiers are used to maintain multiple samples at their set potentials at the same time. The potential differences were adjusted by potentiometric resistors controlling each operational amplifier. Potentials were adjusted regularly to maintain the desired values within ± 5 mV. There was one multi-potentiostat for each tank. For each multi-potentiostat, a common activated titanium mesh counter and a common activated titanium rod reference electrode (Castro, Sagüés, Moreno, and Genesca 1996) were used. Each reference electrode was calibrated regularly with respect to the SCE at the time of potential measurements. The duration of exposure for each test specimen ranged from 55 to 102 days as listed in Table 2. Also listed in Table 2 are the identifiers for each test specimen which begin with either YG or YB.

The current produced by each bar sample was measured and recorded regularly. Cumulative charge was calculated by approximating the area under the current versus time curves using the trapezoidal rule of integral approximation. Visual observations of the defects were noted throughout the test. The approximate pH of the solution was determined at the beginning and end of the testing period with pH paper.

Electrochemical Impedance Spectroscopy

Electrochemical impedance spectroscopy (EIS) can be used to elucidate the electrochemical behavior of a corroding electrode by measuring the time-dependent current response of the electrode to a small alternating potential applied across the interface. This is achieved by using a three electrode cell, shown in Figure 7. In this

investigation, an activated titanium electrode is used as reference and an activated titanium mesh acts as the counter electrode. The impedance (Z(ω)) of the system is defined by (Jones 1996):

$$Z(\omega) = \frac{V(t)}{I(t)} \quad \text{(Eq. 7)}$$

where V(t) is the alternating potential (in complex form i.e. $V = V_o e^{j\omega t}$) being applied to the system, I(t) (in complex form $I = I_o e^{j(\omega t+\Phi)}$) is the current response of the system, ω is the angular frequency given by:

$$\omega = 2\pi f \qquad \text{(Eq. 8)}$$

where f is frequency in hertz, and Φ is the phase angle. Impedance can be separated into real and imaginary components (Jones 1996):

$$Z(\omega) = Z'(\omega) + Z''(\omega) \qquad \text{(Eq. 9)}$$

where Z'(ω) is the real component and Z"(ω) is the imaginary component.

Some electrochemical processes that occur at the surface of the corroding electrode take some time to respond to changes in the applied potential, manifested by a finite value of Φ which is also a function of ω. An example of such a process is the charging and discharging of the interfacial capacitance (Orazem and Tribollet 2008). The electrical response of the interface can be represented by equivalent circuits containing resistors and capacitors (Jones 1996).

Impedance measurement results are customarily displayed in two graphs, the Bode diagram and the Nyquist diagram. The Bode diagram is a plot of log |Z| versus the

frequency. The Nyquist diagram is a plot of the real impedance component versus the imaginary impedance component.

Information about the system is gained when software is used to determine the equivalent circuit that best matches the electrical response of the system. The values assigned to the components in the equivalent circuit represent different aspects of the system that are related to the corrosion rate and the interfacial and coating capacitances (Jones 1996). For example, for the case of uncoated metal under simplified conditions, the equivalent circuit is as shown in Figure 8, where R_s is the ohmic electrical resistance between the reference electrode and the metal/electrolyte interface (Figure 9). C_M is the interfacial capacitance, and R_p is the polarization resistance. The latter is a key element in the EIS interpretation as it is related to the corrosion current by the Stearn-Geary equation:

$$I_{corr} \cong \frac{B}{R_p} \qquad \text{(Eq. 10)}$$

where B is equal to:

$$B = \frac{\beta_a \beta_c}{2.3(\beta_a + \beta_c)} \qquad \text{(Eq. 11)}$$

The β values are the Tafel slopes for the cathodic and anodic reactions. These are typically approximated to be 0.118 V which gives an approximate value of 0.026 V for B, found to be representative of many corroding systems (Jones 1996). Thus, an electrochemical measurement of R_p can be used to obtain an approximate value of the rate at which the metal is being consumed. The corrosion current is related to the rate at which the metal is consumed (moles / second) by the Faradaic conversion:

$$\frac{dm}{dt} = \frac{I_{corr}}{nF} \qquad \text{(Eq. 12)}$$

where dm/dt is the consumption rate, n is the valence (2 for zinc), and F is the Faradaic constant (96,500 Coulombs/equivalent). In terms of cumulative metal thickness lost (T), the corrosion current density, i_{corr} (corrosion current divided by the area affected) can then be converted into mass of metal lost with (Jones 1996):

$$T = \frac{A_w i_{corr} t}{nF\rho} \quad \text{(Eq. 13)}$$

where A_w is the atomic weight of the metal, A is the area affected, ρ is the metal density, and t is time.

In the case of a coated metal, corrosion happens mostly at the coating breaks (Figure 9) and the coating acts as a capacitor. In an impedance test, part of the alternating excitation current flows through the electrolytic resistance of the breaks to the metal interface exposed at the breaks and the other part through the coating capacitance. The equivalent circuit used for this case reflects the current partition among the two paths and is shown in Figure 10, where the C_c is this coating capacitance and R_b is the resistance associated with the break. The interfacial and coating capacitances typically display non-ideal behavior such that their admittance (inverse of impedance) is not jωC as an ideal capacitor, but instead can be represented by the admittance of a constant phase element (CPE) given:

$$Z_{CPE}^{-1} = Y_o (j\omega)^n \quad \text{(Eq. 14)}$$

where Y_o and n are the two parameters defining the CPE (Orazem and Tribbolet 2008).

EIS measurements were taken regularly for the OCP specimens in both solutions. Scans were run at a frequency range of 100,000 Hz to 10 mHz with an amplitude of 10 mV. The choice of equivalent circuit used to analyze the EIS results is detailed in Chapter 4.

Metallography

At least one defect for each polarization regime and solution was analyzed metallographically. A ~2.5 cm long section of the bar around the defect was first cut with a hack saw. A cut was then made down the middle of the defect with a slow speed cutter and diamond blade. One half of the resulting cross-section revealing the defect was set in metallographic epoxy. Rough polishing was conducted with water on Struers MD-Piano resin bonded diamond grinding discs of 120, 600, and 1200 grit. Water free fine polishing was conducted to ensure that little or no zinc was corroded during polishing. The first step of fine polishing was done on Struers MD-Dac cloth using Struers 3 um DP-Paste P polycrystalline diamond paste with Streur alcohol base blue lubricant. The final polishing step was conducted with Struers MD Floc cloth with Beuhler 0.05 um Alumina powder in ethanol. After polishing, samples were examined with a Reichart metallographic microscope and pictures of the defect, which are shown in Appendix II, were taken at a 15x magnification.

Coating Disbondment Testing

After being exposed to solution for the indicated amount of time, the specimens were removed and assessed for corrosion and coating disbondment. Upon removal from solution, the pH of any solution maintained on the surface of the metal on the defect surface was measured with pH paper. If anodic blistering (which affected only +100 mV chloride exposure samples) had occurred, the pH of the solution under the disbonded coating was measured with pH paper as well. The samples were then lightly dried with absorbent paper. Pictures were then taken of each defect. The procedure for measuring the disbondment radius and qualitative disbondment ratings was conducted immediately following the drying and photographing of the sample.

The coating disbondment was assessed in three ways: by the measured length of disbondment from the defect, by qualitative disbondment ratings given to coating sections near the defect, and by pull-off tests conducted near the defect sites.

The procedure for evaluating the length of disbondment from the defect was as illustrated in Figures 12 and 13. A 3 mm wide strip of epoxy was scribe-cut between the ribs on each side of the defect. Two more 3 mm wide strips were scribe-cut above and below the defect across the ribs at a ~90° angle from the ribs, as shown in Figures 12 and 13, forming a skewed cross. The scribe-cuts were made through the epoxy layer to the metal using a sharp, thin blade. After the four strips were scribe-cut, the knife was used to detach a small corner of one of the epoxy strips from the metal at the defect edge. This corner was grasped with precision tweezers and pulled until the epoxy strip broke. The distance from the defect edge to the location where the coating strip broke was then measured and recorded. The same procedure was followed with the remaining three epoxy strips. Four defects on each sample were analyzed in this way. The measurements for each sample bar were then averaged and recorded. This method is similar to that used in (Lau and Sagüés 2009).

Qualitative ratings describing the adhesion level of the coating, listed in Table 3, were used to denote the ease of coating separation. The sections peeled with the precision tweezers in order to define the disbondment radius, were given a rating of 1 or 2. The remaining portion of the 1 cm strip of epoxy, beyond the disbondment radius was cut into 3 mm segments and removed with the knife and tweezers. Each section was given a rating from Table 3 and recorded. The qualitative adhesion ratings of each sample bar were averaged and recorded. The procedure for determining the disbondment radius and qualitative adhesion loss ratings is illustrated in Figure 13.

The pull-off strength of the coating was measured with a mechanical device designed for this specific use (Sagüés, et. al 1994) and is shown in Figure 16. A 6 mm diameter dolly was attached with cyanoacrylate adjacent to a defect. For each polarization regime in both chloride and no-chloride solution, one of the bars used had as part of its surface on one side the rolled-in bar size and make designation. This offered more space between deformation ribs and markings to attach the pull-off dollies. A diagram of these particular samples is seen in Figure 14. The surface of the dolly had

been contoured to match the curvature of the bar. Before attachment the epoxy coating was lightly sanded and degreased by wiping the surface with ethanol to improve adhesion. The epoxy coating around the perimeter of the attached dolly was removed (Figure 15) using a rotating dental drill bit. The testing device slowly pulled the dolly with a universal joint in a direction normal to the bar's surface until the dolly was separated from the bar. This set up is seen in Figure 16. The pull-off force was then divided by the dolly area and recorded as the nominal pull-off strength. This procedure was used in several other investigations (Sagüés, et. al 2009) (Sagüés and Powers 1996).

Supplemental OCP Test Exposures

An additional open circuit experiment was conducted to ensure reproducibility of the test method. Two DCR samples were prepared in the way explained previously and shown in Figure 6. They were immersed in SPS solution, with 19 cm of the bar exposed to the solution. The test chamber was a ~14 cm diameter ~30 cm tall Plexiglas cylinder with square Plexiglas pieces used to seal the top and bottom. The square pieces were attached to the cylinder with silicon gel. The container held ~3L of solution. The specimens were sealed inside the test chamber to prevent carbonation of the solution. The top square piece contained holes for wires and electrodes which were plugged with rubber stoppers. The open circuit potentials of the specimens were measured regularly with a SCE.

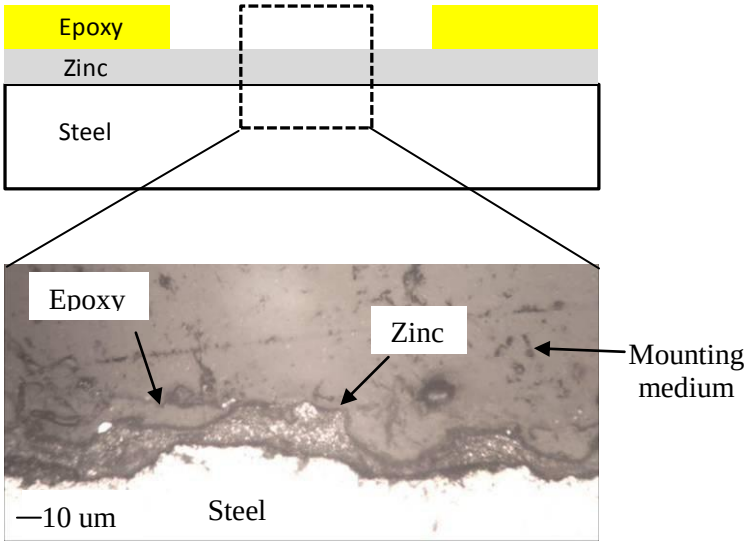

Figure 5: Metallographic Cross-Section of Intentional Defect Showing Removal of Much of the Epoxy Coating.

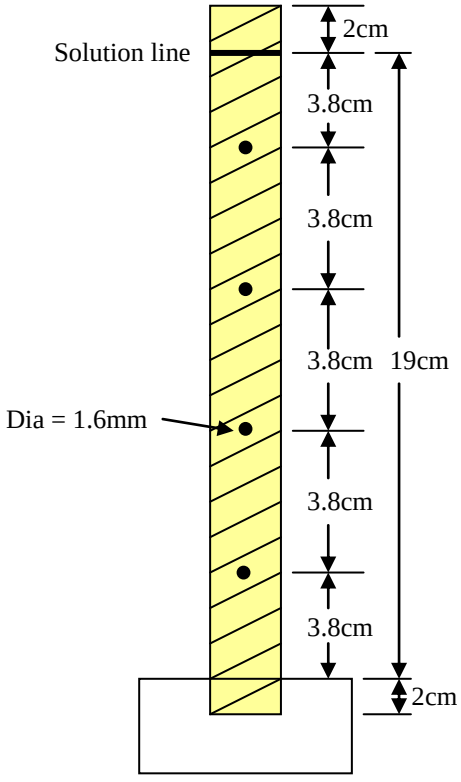

Figure 6: Diagram of DCR Test Sample.

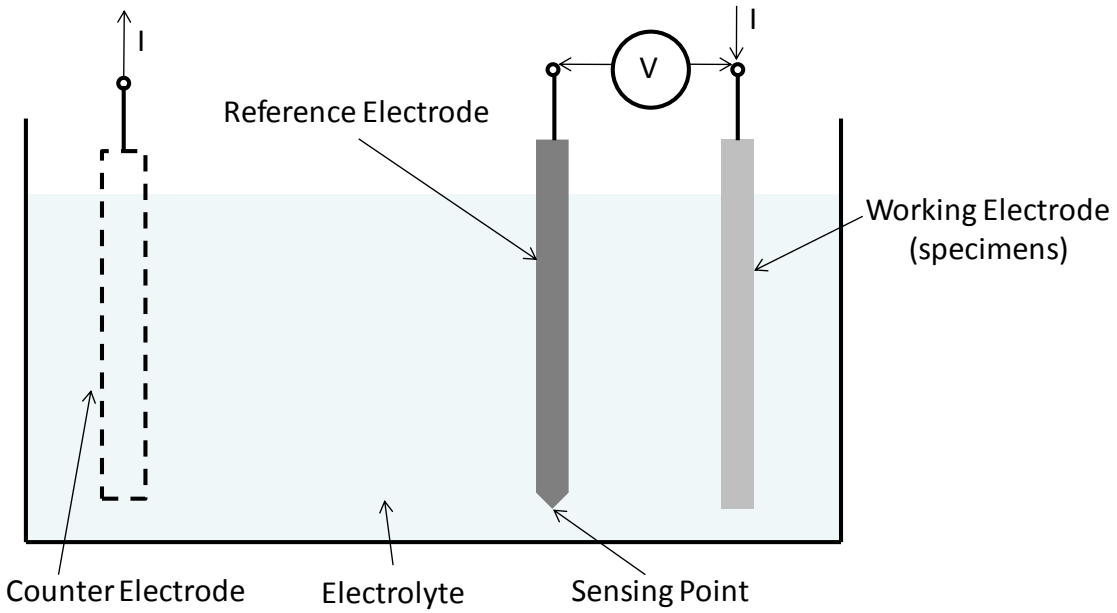

Figure 7: Conceptual Diagram of a 3 Electrode Cell. V is the applied potential and I is the resulting current. An external instrument (potentiostat) makes the necessary current-potential control adjustments so that the necessary amount of current, I, is introduced to obtain the desired value of V. The counter electrode serves to provide a return path to the excitation current.

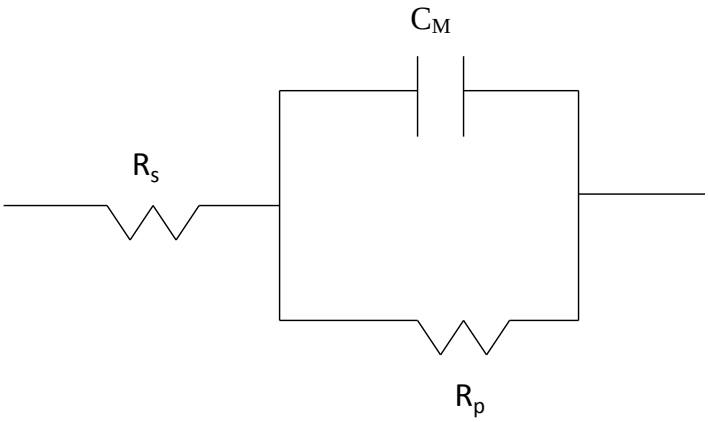

Figure 8: Simplified Equivalent Circuit for Uncoated Metal.

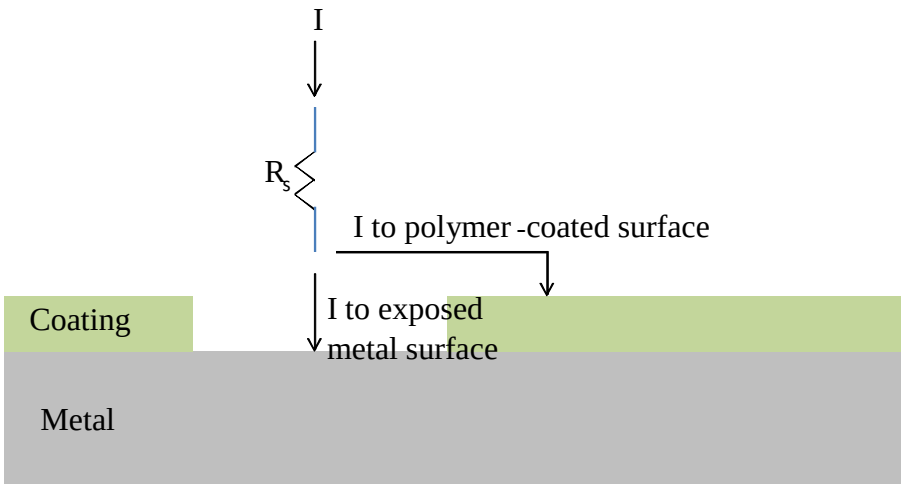

Figure 9: EIS Excitation Current Paths for a Coated Metal with a Coating Break.

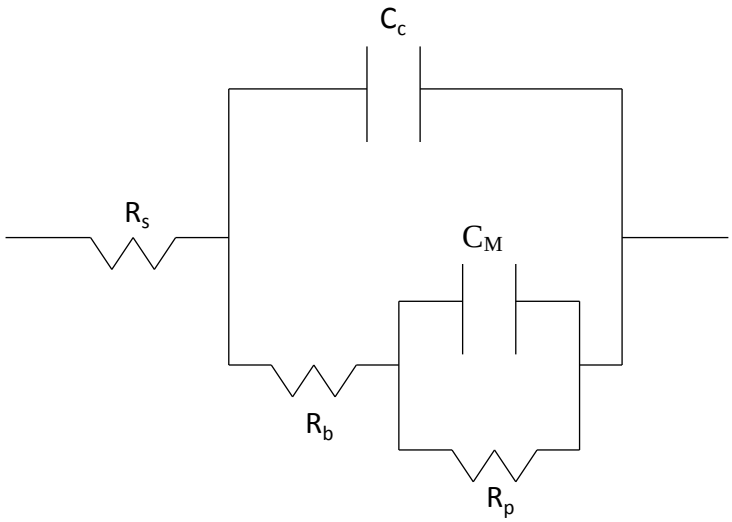

Figure 10: Equivalent Circuit for Coated Metal – Ideal Capacitance.

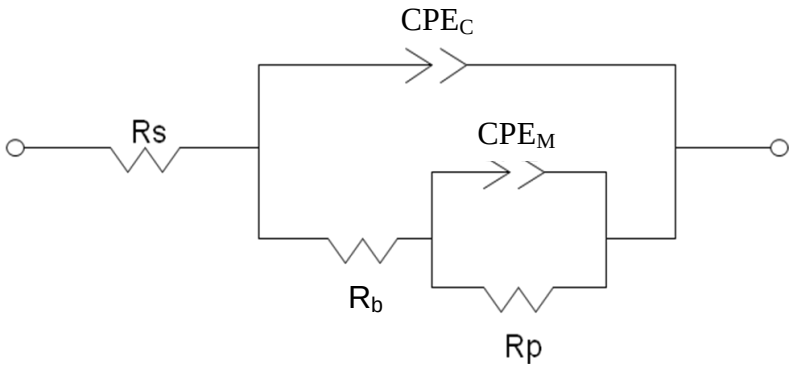

Figure 11: Equivalent Circuit for Coated Metal with Capacitors Replaced by CPEs. (Orazem and Tribollet 2008)

Figure 12: Specimen Subjected to the Disbondment Measurement Procedure. Specimen was polarized to -500 mV with no-chloride exposure.

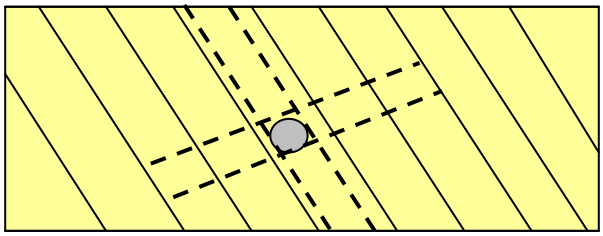

Step 1: Scribe epoxy strips.

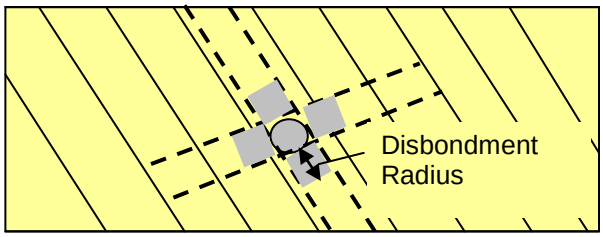

Step 2: Peel epoxy strips. Measure disbondment radius and assign qualitative ratings.

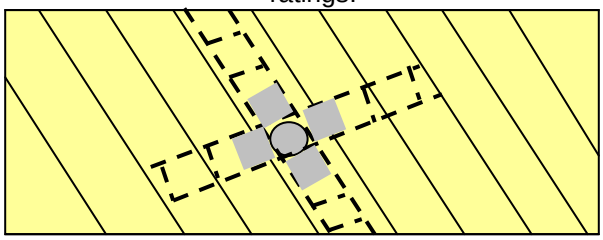

Step 3: Scribe 3mm epoxy sections and peel. Assign qualitative ratings to sections.

Figure 13: Procedure for Quantifying Adhesion Loss through Disbondment Radius Measurement and Qualitative Disbondment Ratings.

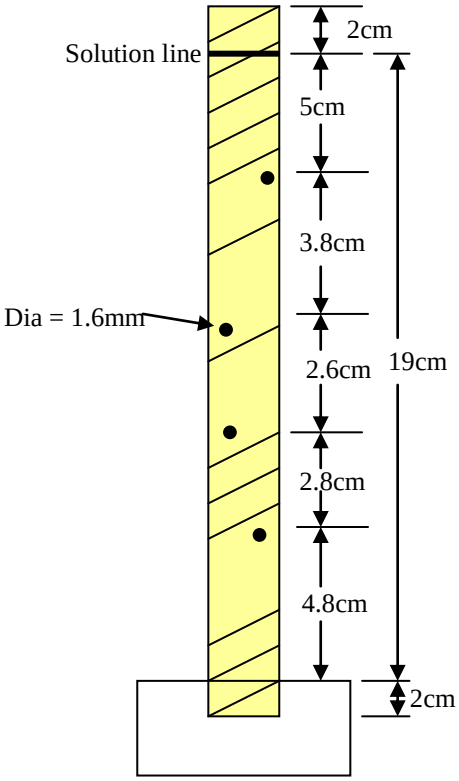

Figure 14: Diagram of DCR Sample Used for Pull-off Test. This figure shows one side of the bar. The opposite side is the same as that shown in Figure 2.

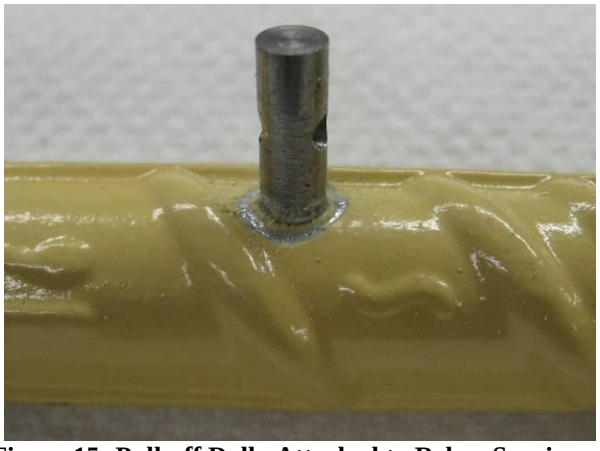

Figure 15: Pull-off Dolly Attached to Rebar Specimen.

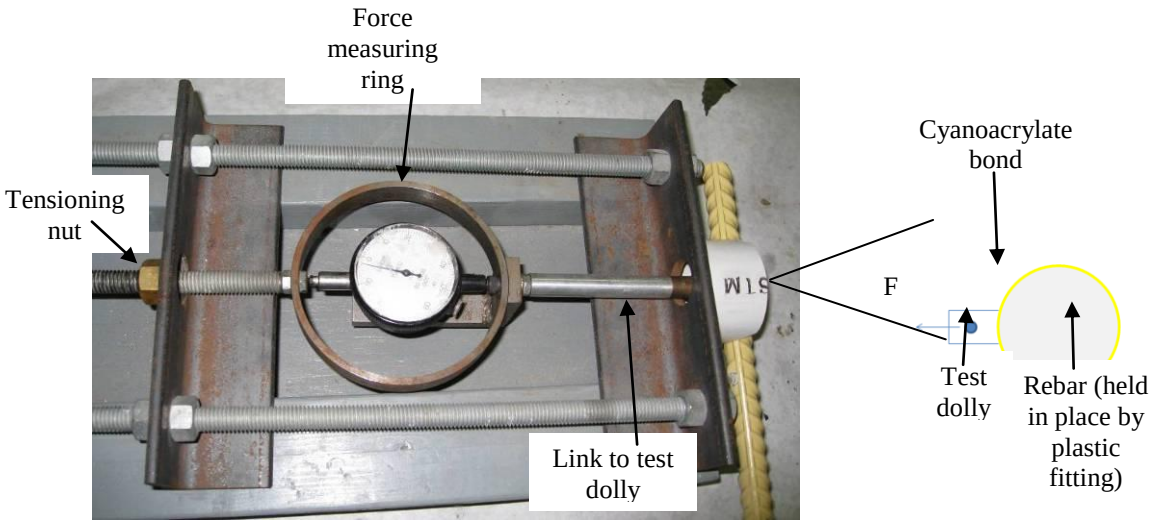

Figure 16: Rebar Specimen and Pull-off Testing Device.

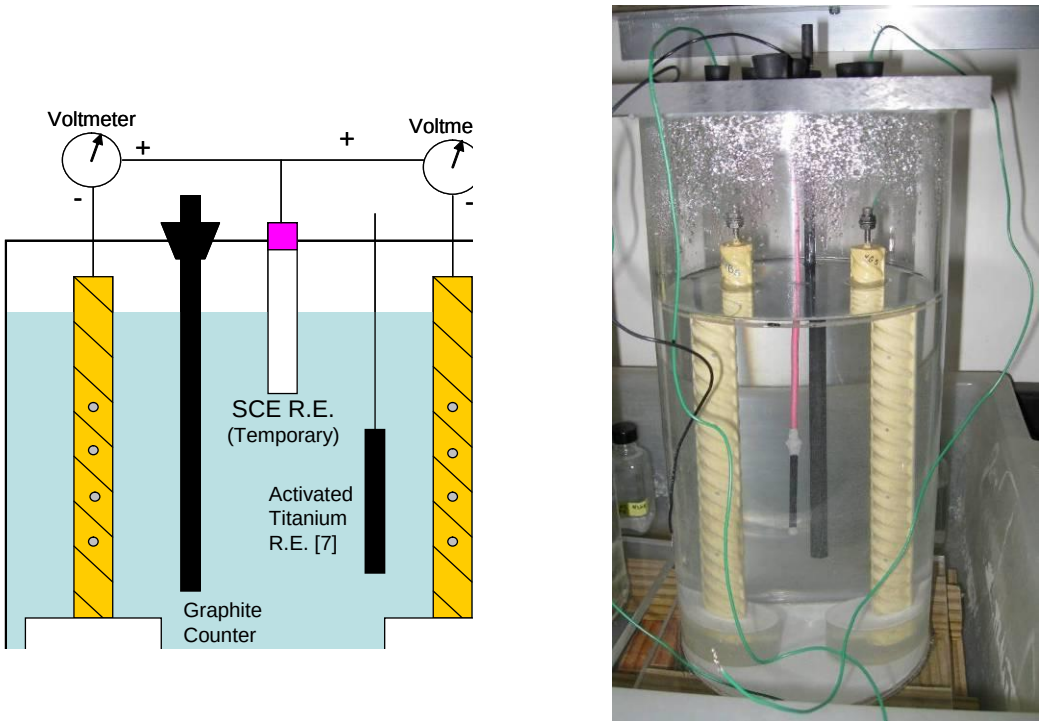

Figure 17: Supplemental OCP No-chloride Exposure Test Cell.

Table 2: Chemical Preparation and Composition of Test Solutions.

Solution Type	KOH		NaOH		$Ca(OH)_2$*		NaCl		DI Water	pH
SPS	0.19M	20.9g	0.09M	7.4g	0.03M	4.2g	N/A	N/A	2L	13.3
SPS + NaCl	0.19M	20.9g	0.09M	7.4g	0.03M	4.2g	0.6M	70.0g	2L	13

* Amount in solution.

Table 3: Time of Solution Exposure (days) for Each Test Sample Designated by its Identifier.

Potential (mV vs. SCE)	SPS				SPS + NaCl			
OCP	YB14	101	YG7	101	YG21	86	YG6	86
+100	YG15	67	YG2	65	YG17	55	YG3	62
-500	YG14	67	YG4	71	YG22	88	YG11	89
-1000	YG9	82	YG18	102	YG20	88	YG8	89

Table 4: Description of Qualitative Adhesion Ratings

Qualitative Adhesion Rating	Characteristics of Adhesion Loss
1	Coating is easily removed.
2	Coating is disbonded but some force is needed to remove.
3	Coating is disbanded but a large amount of force is required to remove. Some parts of coating remain on metal surface.
4	Coating is not disbanded.

Chapter 4
Results and Discussion

Note: In the following, frequent reference will be made to the (Lau and Sagues 2009) paper "Corrosion of Epoxy- and Polymer/Zinc- Coated Rebar in Simulated Concrete Pore Solution" for comparison purposes. That investigation will be referred to as the "Phase 1 investigation". A detailed summary of the comparisons between the results of the Phase 1 investigation and this investigation is shown in Table 5.

As Received DCR Condition

The combined polymer plus zinc coating thickness was on average ~0.28 mm and the standard deviation was ~0.03 mm which meets the ASTM A1055 specification. The cumulative fraction of coating thickness measurements is shown in Figure 18. The zinc thickness was on average ~0.028mm which also meets the specification. The bars selected contained no visible coating defects. Those specimens used in the test were concluded to be representative of the average product produced by the manufacturing company.

Visual Observations

During the period of immersion, only the +100 mV chloride exposure specimens showed corrosion product formation. The oxide was reddish brown in color, indicating an iron oxide, likely oxidized to Fe^{3+}, which formed tubercles that extended outward from the defects (Figure 19 and 20). Corrosion products developed on one specimen after ~1 day and, on the duplicate specimen, after ~3 days of immersion. This oxide formation had developed in all eight defects on each of the two samples by the termination of the test. In contrast, in the Phase 1 investigation, oxide formed on ECR and DCR +100 mV chloride exposure specimens in less than an hour, so this stage seems to be delayed in the

DCR with defects exposing only zinc. It was also noted in the Phase 1 investigation that corrosion products developed on ECR +100 mV and -500 mV chloride exposure specimens in locations other than the intentional defect sites as well. The authors concluded this was caused by anodic blistering and subsequent cracking of the polymer coating. On the contrary, in this study, anodic blistering was noted only in the +100 mV chloride exposure specimens and no solid steel corrosion developed under the coating. Moreover, solid white zinc corrosion product was not apparent on samples for any of the polarization regimes in either solution as seen in Figure 20. This suggests the development of a zinc hydroxide which dissolves in an alkaline environment to $HZnO_2^-$ and ZnO_2^{2-} (Pourbaix 1974).

Electrochemical Measurements

Open Circuit Specimens

The open circuit potentials for specimens in both solutions are shown in Figure 21. All six specimens were at very negative potentials (-1400 mV) immediately after immersion, but increased after ~1 day to ~600 mV, where the potentials remained relatively stable for the remainder of the immersion period. There was no significant difference between the OCP values of samples with and without chloride exposure. These potential values are similar to those noted with bulk zinc in similar solutions (Videm 2001) suggesting that the bulk zinc in the defects corroded initially and then approached passive behavior.

EIS analysis was conducted with two types of equivalent circuits. The impedance diagram of coated metals with behavior that can be approximated by the circuit in Figure 11 shows two loops, corresponding to the effective time constants associated with the combination of CPE_C-R_b and CPE_M-R_p respectively (Orazem and Tribollet 2008). If corrosion at the break is very slow, as when the metal exposed by the break is in a near passive condition, Rp becomes very large. In that case the loop associated with CPE_C-R_b becomes less apparent and the combination of CPE_M-R_p tends to dominate the impedance spectrum, at least at low frequencies. In that case, the low frequency impedance behavior

tends to resemble that of the circuit in 8, with a CPE (CPE_M with parameters YoM and nM) instead of the ideal capacitance C_M. Thus as a working approximation, the circuit in Figure 11 was used to fit the experimental EIS data for the initial part of the exposure, when the metal exposed at the breaks was in the active condition (potentials more negative than ~ -900 mV), and the impedance diagrams exhibited two clearly defined loops. This condition is apparent in Figures 35 to 36, 48 to 50, 61 to 64, and 88 to 91 in Appendix 1. When a near passive regime developed (considered to be manifested by potentials more positive than ~ -900 mV), the circuit shown in Figure 8 with the capacitance replaced with CPE_M was used instead. Again, a working approximation was implemented consisting of using only the four lowest frequency data points (10 mHz to 100 mHz) for the fitting procedure as that frequency range was deemed to be most representative of the impedance behavior dominated by the polarization resistance of the system. It is noted that the value of R_s obtained in that case is only a nominal parameter and is not further considered. After the value of R_p was obtained for each test, it was used to estimate the apparent corrosion current (Eq. 10) and estimated metal consumption rate (Eq. 12). The corrosion current was then divided by the area of metal exposed at the coating breaks to obtain the corrosion current density. The metal thickness loss as function of immersion time was calculated using this current density (Eq. 13).

The EIS experiments provided additional insight on the behavior of the OCP specimens. It is noted, however, that EIS-estimated corrosion rates are subject to considerable uncertainty (Orazem and Tribollet 2008) especially considering the uncertainty associated with the working approximations noted above. Consequently, the EIS analysis results obtained here are presented mainly for comparison purposes. In the following the expression “corrosion current density” when it is estimated for EIS measurements, denotes only an apparent or nominal corrosion current density and it is understood that future analysis using more sophisticated methods may yield updated results.

The EIS analysis results are summarized in Figure 26. The corrosion current density (calculated by assuming for simplicity that all the corrosion took place at the surface area directly exposed at the intentional defects) of OCP specimens, both in chloride and no-chloride exposure, started at a high value (~1E-4 A/cm^2) which quickly dropped to less than 1e-6 A/cm^2 . Those results were summed by trapezoidal integration, after application of Eq. 13, to calculate the nominal zinc thickness consumed as function of time. The result is displayed in Figure 27. The nominal metal loss was in all cases less than that of the average zinc thickness that was determined by direct metallographic observation (denoted by the red line in Figure 27). Considering the aforementioned uncertainty inherent to the EIS estimates of metal loss, these results are in good agreement with the observation of significant amounts of zinc remaining at the defects after exposure (Figures 20 and 30), as well as the potential evolution evidence of early onset of passive or otherwise very slow corrosion of the zinc at the OCP.

While all of the OCP DCR specimens in this investigation showed a trend toward passive behavior, their EIS-estimated corrosion current density was somewhat higher than those reported for similar exposure in the to-steel defects of the Phase 1 specimens. Moreover, the OCP potential in this investigation tended to stabilize at about -600 mV compared to ~-400 mV in Phase 1. These differences may be due to different passivation mechanisms. The Phase 1 specimens experienced crevice corrosion (Fontana and Greene 1978) of the zinc between the carbon steel bar and the epoxy polymer coating (Lau and Sagüés 2009) (Accardi 2009). The zinc corrosion equations (Eq. 4 and 5) show that during dissolution, OH^- ions are consumed. Because this occurs in a crevice the occluded geometry promotes accumulation of reaction products, as shown schematically in Figure 28. As a result, the solution immediately adjacent to the corroding zinc tends to acidify slightly as indicated by the blue arrow in Figure 29. Also, because of the occluded geometry, the concentration of zincate ions may appreciably increase in the crevice which shifts the boundary line on the Pourbaix diagram separating active and passive regions to the right (red arrow in Figure 29). The combination of increasing zincate ion concentration and a dropping pH shifts conditions to the passive region of the Pourbaix

diagram. The authors concluded also that passivation due to calcium hydroxyzincate formation should not be discounted, but it was noted that the calcium ion concentration in the solution was very low.

The OCP crevice conditions were less likely to be predominant in this investigation as the DCR specimens here had defects were the zinc was freely exposed to solution instead of being present only at the edges of the defect. As indicated earlier, upon removal from the solution, there was still abundant zinc present on the surface of the defects and between the polymer and the steel around the rim of the defect (Figure 30) so crevice conditions had not developed. Nevertheless, passive behavior of the freely exposed zinc appears to have developed here even in the absence of the in-crevice beneficial factors noted in Phase 1. A possible explanation is that because there is calcium in the solution, calcium hydroxyzincate may have formed on the surface (per Eq. 6) and passivated the zinc. This passivity may however by imperfect. As noted before, high pH solutions tend to create larger calcium hydroxyzincate crystals which may not form protective enough films (Andrade and Alonso 2004) and a pH 13.1 or 13.3 protection may be substantially compromised. The SPS solution used here is very close to that transition pH range, so it is possible that a completely cohesive passive layer is not present. This may explain the apparent terminal dissolution rate here being somewhat higher than that observed in Phase 1.

Polarized Specimens

For the no-chloride exposure tests, all polarization regimes initially exhibited high anodic current (e.g. >1mA), indicating active corrosion of zinc. Later on, the +100 mV samples had small anodic current (~0.5 μA) for the majority of the testing time. Both the -500 mV and the -1000 mV regimes resulted in small cathodic currents, ~0.5 μA and ~1.5 μA, respectively. These results are shown in Figure 22.

For the chloride exposure tests, the +100 mV specimens demanded high anodic currents (>1 mA) initially and stabilized over a couple of days to a regime of continuing

corrosion at 200 and 700 μA, which was confirmed by the observation of solid corrosion product on the defects. After initial high anodic currents, the -1000 mV and -500 mV specimens stabilized to a very small cathodic current (~1 μA) and values in the range of ±0.3 μA, respectively. The high initial current and subsequent decrease to very small values suggest an initial period of active zinc corrosion followed by the development of a near passive regime possibly by a mechanism similar to that discussed earlier.

The cumulative charges for the +100 mV chloride and no-chloride exposure samples were ~1000 coulombs and ~6 coulombs, respectively. This indicates that the chloride exposure specimens sustained considerably more corrosion damage than the no-chloride exposure specimens. This is consistent with visual observations. Using Eq. 12 and 13 and assuming corrosion occurred only in the area exposed by the coating breaks, the zinc thickness lost was calculated from the cumulative charge. The estimated thickness lost for the chloride and no-chloride exposed specimens was 3mm and 20 um, respectively. This estimate for the no-chloride specimens indicates that not all of the zinc in the defect was consumed. The estimate for the chloride specimens is clearly too large, indicating that the assumption made that corrosion only occurred in the defect area is not valid for these specimens as is evidenced by the anodic blistering of the coating. A more appropriate analysis that takes into account corrosion in the zone around the defect is presented in the Coating Disbondment section.

As shown in Table 4, the electrochemical results for the Phase 1 DCR specimens and the DCR specimens in this investigation are, for the most part, very similar. There is, however, one notable difference. The Phase 1 open circuit potentials exposed to both solutions follow a similar pattern to this investigation, starting at a very negative value upon immersion and increasing to a relatively stable higher value. However, the potentials for the Phase 1 investigation are more positive, starting at -1000 mV and stabilizing at -400 mV. The potential trends for both defect types suggest an approach to passive behavior. The difference in potential values may be due to different passivation mechanisms as discussed earlier.

The Phase 1 ECR chloride exposure results differed extensively from the results of the DCR in this investigation. The +100 mV Phase 1 ECR specimens demanded over a comparable exposure period a cumulative anodic charge of 6000 C, which is 6 times that of DCR in both Phase 1 and in the present investigation, showing a tendency for ECR to corrode to a greater extent in this testing scheme. Also, the ECR -500 mV specimens in Phase 1 corroded actively, demanding ~ 1 mA of anodic current. The comparable DCR specimens demanded a high initial anodic current (>1 mA) but quickly stabilized to ~0.75 μA of anodic current, indicating a near passive regime. The ECR open circuit potentials in Phase 1 were initially slightly negative and decreased during the test, indicating a transition from passive to active behavior. The DCR samples behaved in the opposite manner, transitioning from active to near passive behavior over the period of immersion.

The Phase 1 ECR no-chloride exposure specimens behaved under most test conditions similarly to the DCR specimens in this investigation with one notable exception. As in the chloride exposure tests, the Phase 1 and present investigation open circuit DCR transitioned from active to passive behavior during the test. In contrast, the open circuit ECR remained at an only slightly negative potential for the entire immersion period, indicating a continuous passive state.

Coating Disbondment

Figures 31-33 show the disbondment test results for the chloride and no-chloride exposure specimens. The results were similar for most of the polarization regimes and solutions, averaging at ~5 mm disbondment radius, ~13 MPa pull-off strength, and ~1.75 qualitative disbondment rating. The +100 mV chloride exposure tests showed very different results, with ~10mm disbondment radius, ~1 qualitative disbondment rating, and negligible pull-off strength. This high amount of coating disbondment surrounding the defects is a direct result of active corrosion and anodic blistering.

For the +100 mV chloride exposure specimens, a discolored area surrounding each defect under the coating was observed as exemplified in Figure 34. A similar

observation was noted during Phase 1 (Lau and Sagüés 2009). The average diameter of this discolored area in eight defects examined was ~1.7 cm. It was assumed that the zinc was entirely consumed in that region and the corresponding Faradaic charge was calculated using Eq. 12 and 13. The average charge calculated was ~1100C. While this estimate is subject to uncertainty as the entire discolored region was not revealed completely in all cases, the value is in approximate agreement with the cumulative charge calculated for these specimens from the current output of the system. This observation supports the assumption of near complete consumption of the zinc in the discolored region.

The Phase 1 DCR specimens for all polarization regimes in both solutions had comparable disbondment results to those observed in this investigation, although somewhat less disbondment was observed in the present study in the -500 mV and -1000 mV chloride exposures. The conclusions on disbondment behavior relative to that of ECR consequently remains generally comparable to those noted in the Phase 1 investigation.

Implications on Anticipated Performance of DCR

This investigation showed that when defects reached only through the polymer layer and expose the underlying zinc, it reacted initially at a fast rate with the highly alkaline simulated pore water environment. However, the reaction slowed rapidly approaching a passive regime with very low nominal corrosion rate, even in the presence of chloride ions. The length of time that the system could sustain this regime cannot be accurately projected at this time, but specimens exposed for up to 100 days still retained much of the initial zinc layer. This finding is encouraging in demonstrating an ability of the zinc layer to withstand the nominally highly aggressive alkaline test medium used here, even when the layer was freely exposed. These findings supplement the Phase 1 findings that zinc consumption was slow in the crevice surrounding a to-steel defect, which would simulate the conditions prevalent after all the freely exposed zinc was consumed. These results suggest then that the overall process of zinc wastage in DCR in

concrete pore water is not likely to be rapid, which would be beneficial to extending the period in which the barrier and galvanic properties of the zinc are maintained.

The disbondment and anodic/cathodic behavior of DCR with to-zinc defects was similar to that observed for to-steel defects in Phase 1, in that it was comparable to or less severe than for ECR. Thus the defect mode examined here, more representative of expected in-service surface condition, does not appear to introduce further vulnerability. .

The accelerated evaluation in this work needs to be supplemented by longer term exposure testing in concrete and field structures. Investigations to that effect are in progress by Florida DOT and elsewhere (Darwin, et. al 2007).

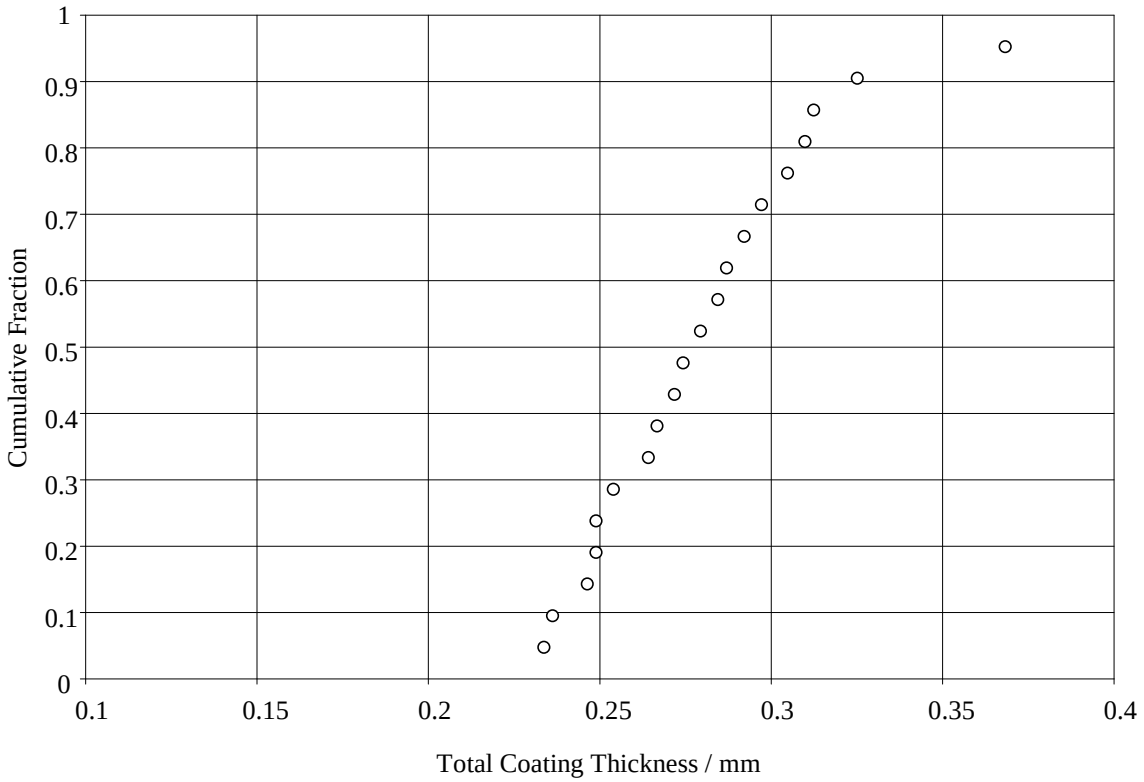

Figure 18: Combined Polymer and Zinc Coating Thickness Distribution.

Figure 19: Solid Corrosion Product that Developed on +100 mV Chloride Exposure Specimens. Specimen YG3

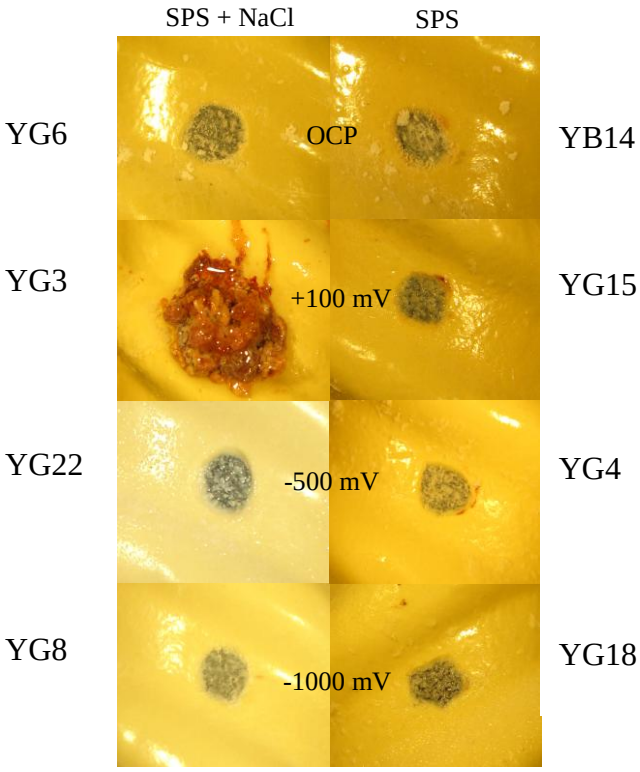

Figure 20: Appearance of Defects after Immersion Period.

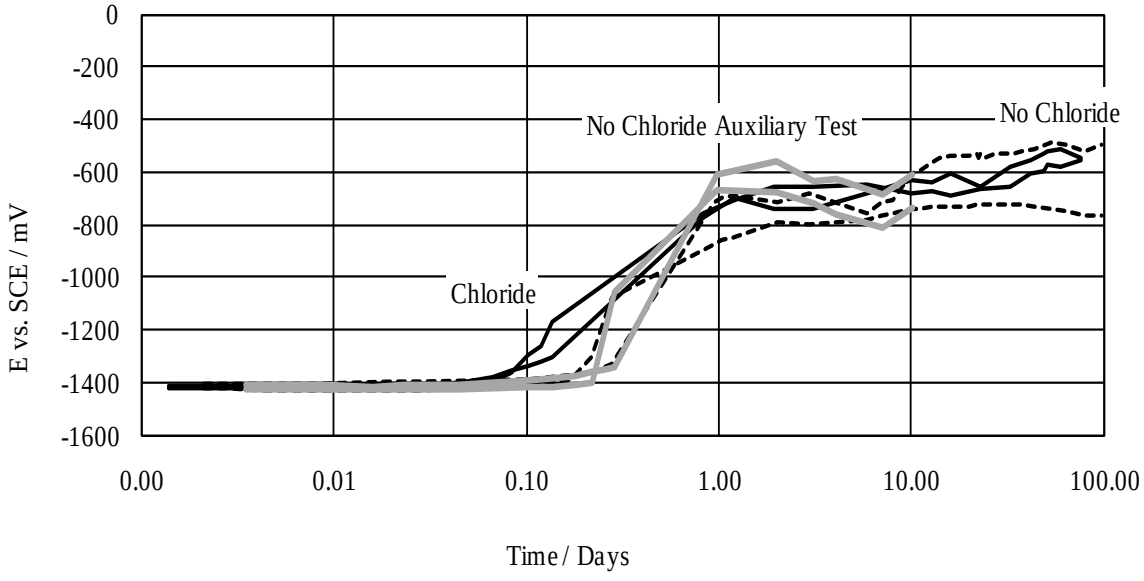

Figure 21: Open Circuit Potential as Function of Time for Chloride (Solid Black Line), No-chloride Exposure OCP (Dashed), and No-chloride Auxiliary OCP (Gray) Duplicate Specimens

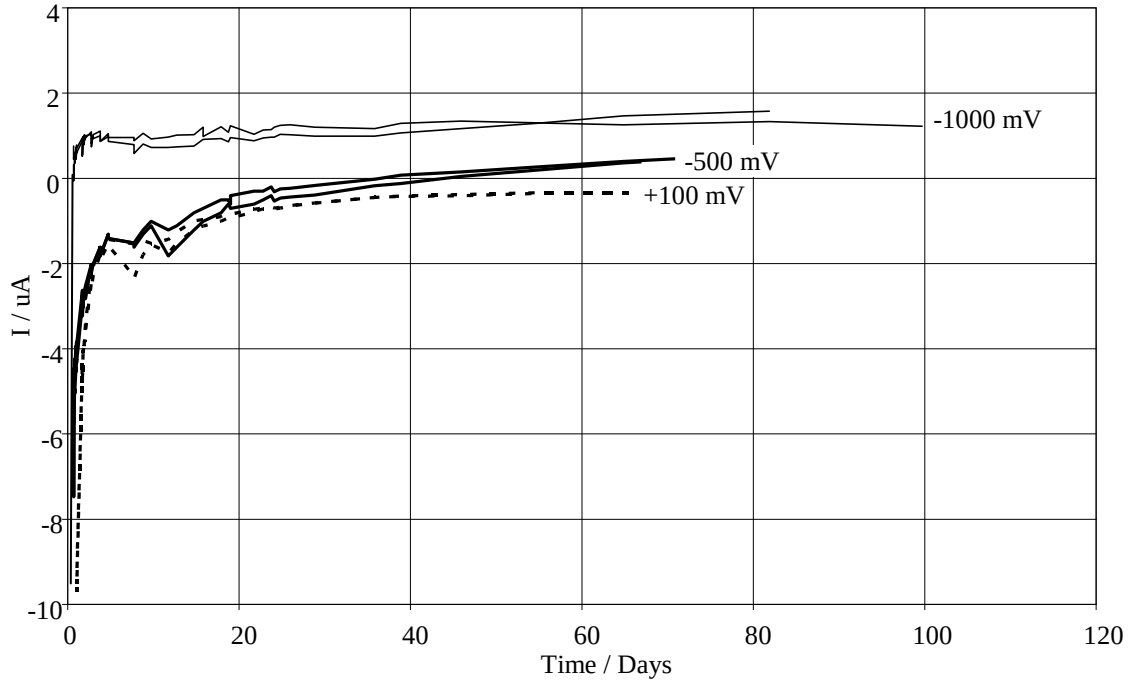

Figure 22: Polarization Current Evolution with Time for No-Chloride Exposure Duplicate Specimens.

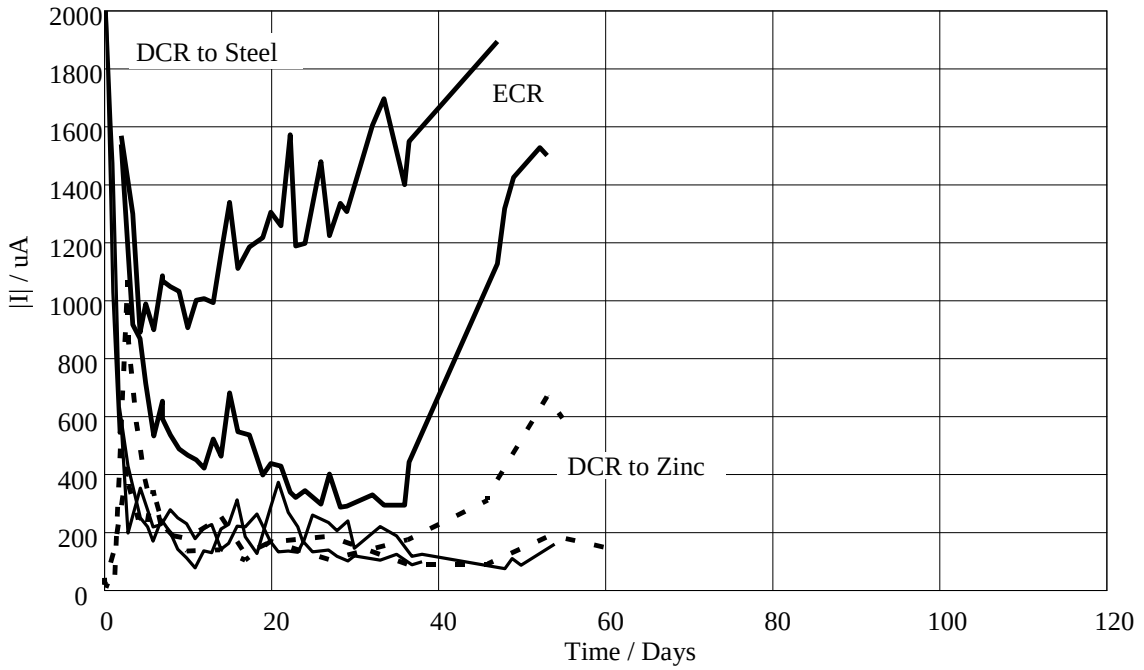

Figure 23: Polarization Current Evolution with Time for +100 mV Chloride Exposure Duplicate Specimens. This figure includes results from the Phase 1 investigation and this investigation.

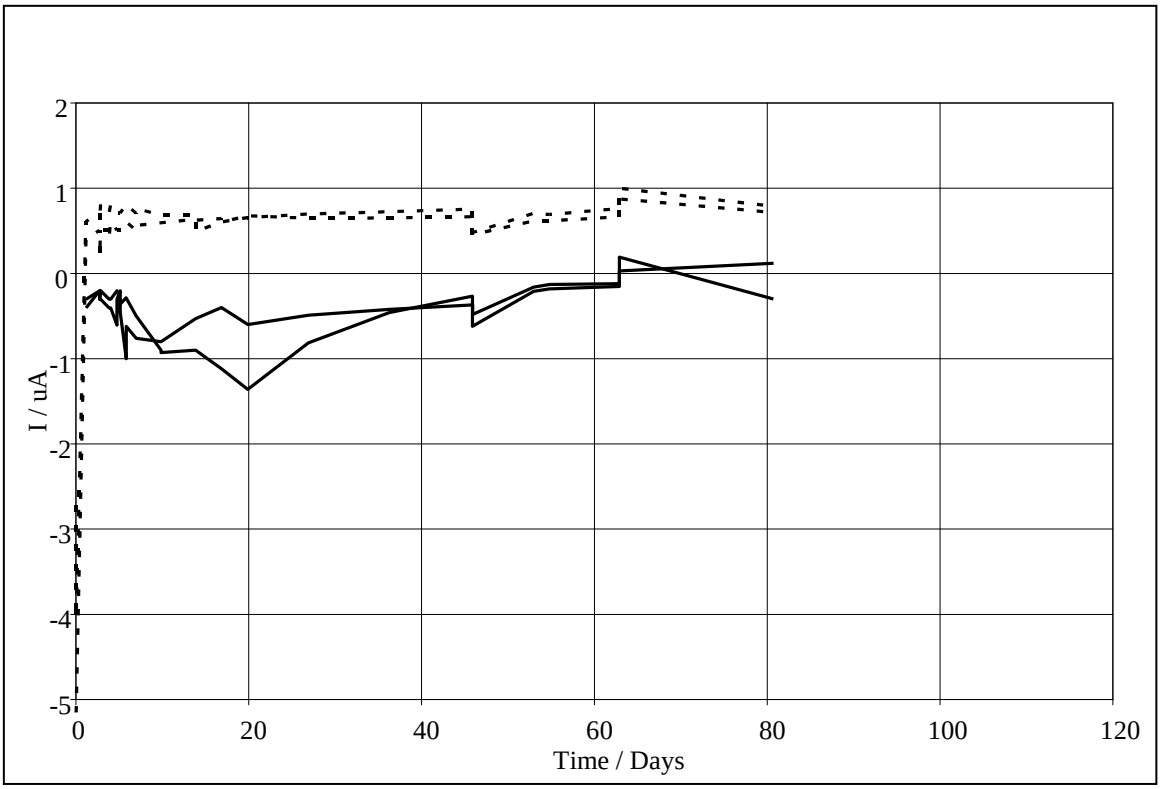

Figure 24: Polarization Current Evolution with Time for -500 mV and -1000 mV Chloride Exposure Duplicate Specimens.

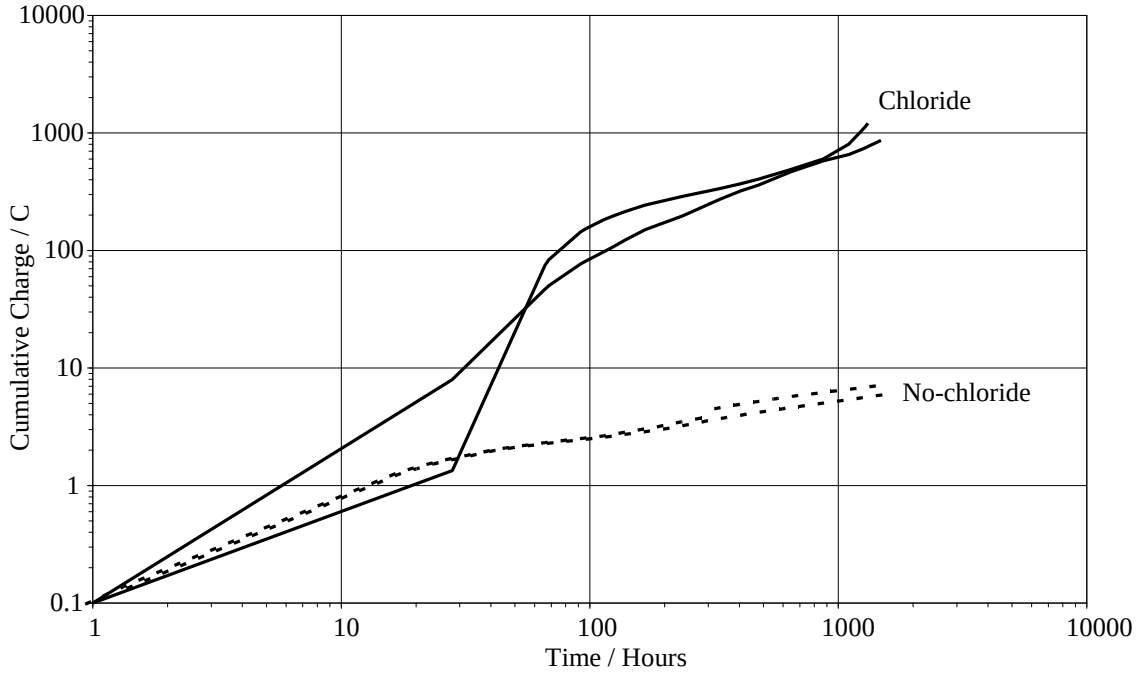

Figure 25: Cumulative Anodic Charge for +100 mV Chloride and No-chloride Exposure Duplicate Specimens.

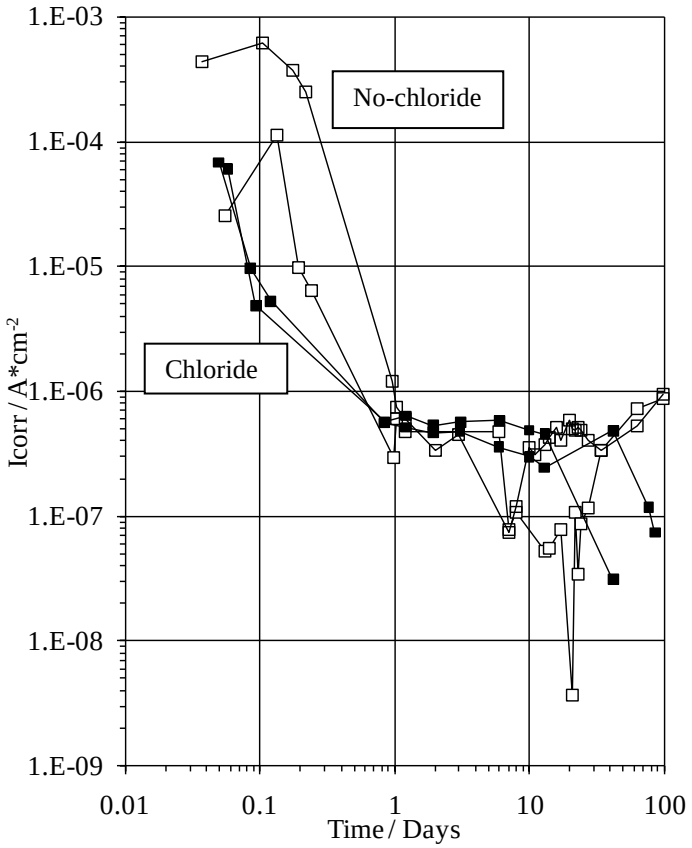

Figure 26: Nominal Corrosion Current Density from EIS Measurements of Duplicate OCP Specimens as a Function of Exposure Time. Chloride exposure: filled symbols. No-chloride exposure: open symbols.

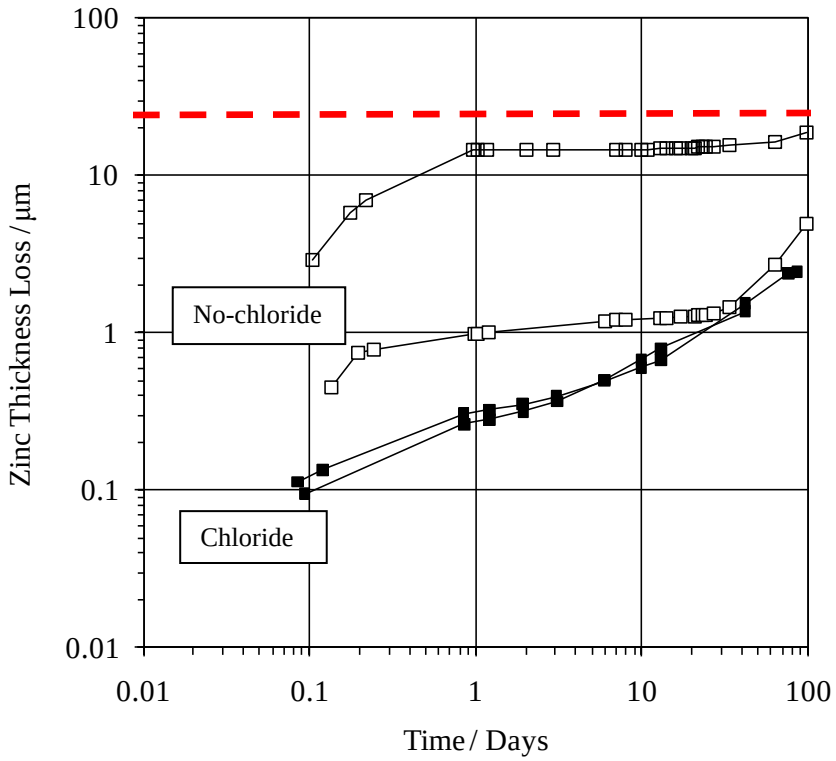

Figure 27: Nominal Zinc Thickness Loss Estimated from EIS Measurements of OCP Duplicate Specimens as a Function of Exposure Time. Dashed line indicates the average thickness of the sprayed zinc layer.

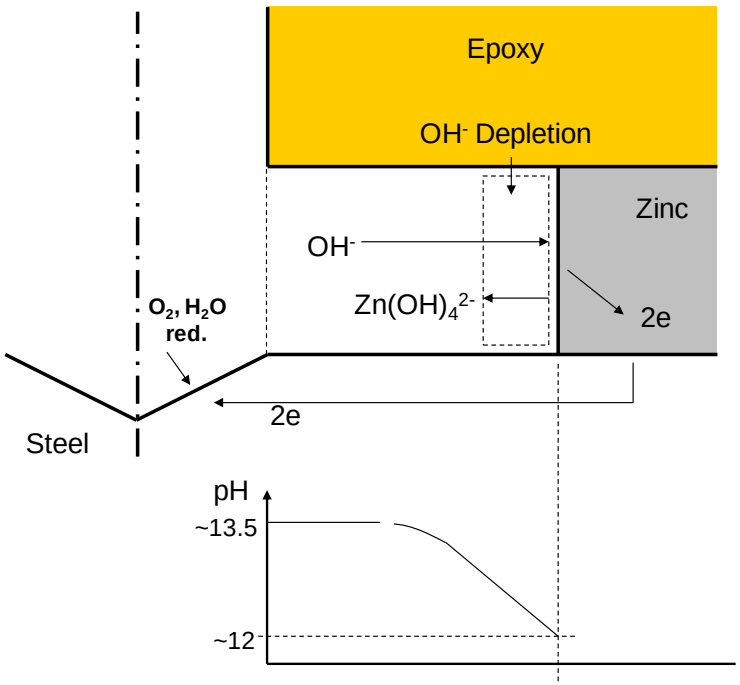

Figure 28: Diagram Showing Possible Passivation Mechanism for Phase 1 DCR (Accardi 2009).

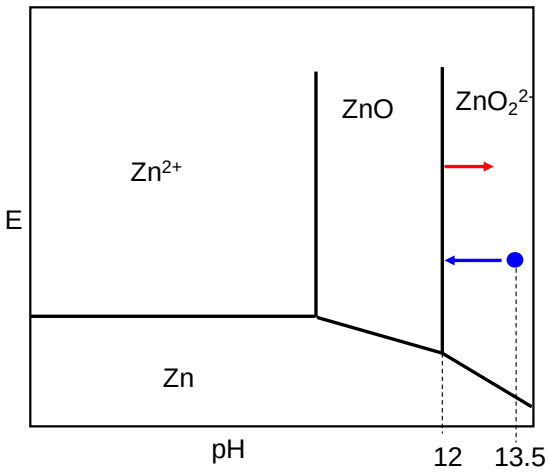

Figure 29: Pourbaix Diagram Showing the Effect of Increased pH and Increased Zincate Ion Concentration (Accardi 2009).

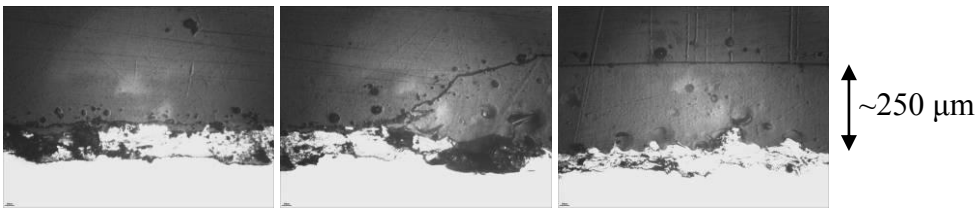

Chloride OCP

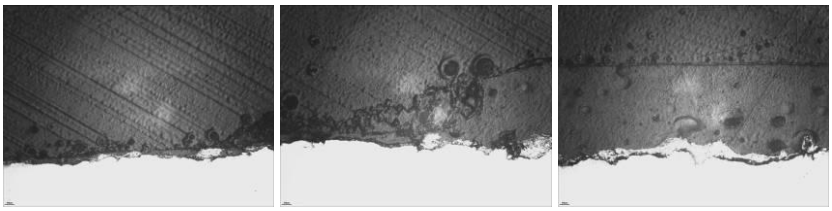

No-chloride OCP

Figure 30: Metallographic Cross-Sections of Chloride (YG6) and No-Chloride OCP (YB14) Specimens after Exposure. The rightmost pictures shows the original ~ 250 µm thick polymer coating (just outside the defect); defect region starts at center picture

Table 5: Summary of Phase 1 and This Investigation Results.

			Phase 1 Investigation		This Investigation
			DCR	ECR	DCR
Chloride Exposure	+100 mV	Current	Initial high anodic current, stabilized to ~0.1 mA (anodic)	~1 mA (anodic)	Initial high anodic current, stabilized to 0.2-0.6 mA (anodic)
		Cumulative Charge	~1000 C	~6000 C	~1000 C
		Average Disbondment Radius	~11mm	~9mm	~10mm
		Average Disbondment Rating	~1	~1	~1
		Average Pull-off Strength	Negligible	Negligible	Negligible
	-500 mV	Current	Initial high anodic current, stabilized to 1-3 uA	~1 mA (anodic)	Initial high anodic current, stabilized to ~0.75 uA (anodic)
		Cumulative Charge	N/A	~1000 C	N/A
		Average Disbondment Radius	~8mm	~7mm	~4mm
		Average Disbondment Rating	~2	~1.5	~1.75
		Average Pull-off Strength	~10 MPa	Negligible	~11 MPa
	-1000 mV	Current	Initial high anodic current, stabilized to 1-3 uA (cathodic)	2-3 uA	Initial high anodic current, stabilized to ~0.5 uA (cathodic)
		Average Disbondment Radius	~7mm	~10mm	~4mm
		Average Disbondment Rating	~2	~1	~1.75
		Average Pull-off Strength	~10 MPa	~13 MPa	~15 MPa
	OCP	Potential	Initial ~-1000 mV, stabilized to ~-400 mV	Initial ~-300 mV, stabilized to ~-600 mV	Initial ~-1400 mV, stabilized to ~-600 mV
		Average Disbondment Radius	~5mm	~5mm	~4.5mm
		Average Disbondment Rating	~2	~2	~2
		Average Pull-off Strength	~15 MPa	~18 MPa	~14 MPa

Table 5: (Continued)

			Phase 1 Investigation		This Investigation
			DCR	ECR	DCR
No-chloride Exposure	+100 mV	Current	Initial high anodic current, stabilized to ~0.2 uA	~0.02 uA	Initial high anodic current, stabilized to ~-0.5 uA
		Cumulative Charge	~1.5 C	~0.15 C	~8 C
		Average Disbondment Radius	~6.5mm	~3.5mm	~6mm
		Average Disbondment Rating	~2	~1.75	~1.6
		Average Pull-off Strength	~15 MPa	~14 MPa	~11 MPa
	-500 mV	Current	Initial high anodic current, stabilized to 1-3 uA	2-3 uA	Initial high anodic current, stabilized to ~0.5 uA
		Average Disbondment Radius	~6.5mm	~2mm	~5mm
		Average Disbondment Rating	~2	~2	~1.75
		Average Pull-off Strength	~10 MPa	~20 MPa	~12 MPa
	-1000 mV	Current	Initial high anodic current, stabilized to 1-3 uA	2-3 uA	Initial high anodic current, stabilized to ~1.5 uA
		Average Disbondment Radius	6mm	~6mm	~4mm
		Average Disbondment Rating	~2	~1.75	~1.75
		Average Pull-off Strength	~10 MPa	~4 MPa	~12 MPa
	OCP	Potential	Initial -1000 mV, stabilizes at ~-400 mV	~-200 to -100 mV	Initial ~-1400 mV, stabilizes at ~-600 mV
		Average Disbondment Radius	~6mm	~3mm	~5mm
		Average Disbondment Rating	~2	~2	~1.75
		Average Pull-off Strength	~14 MPa	~20 MPa	~13MPa

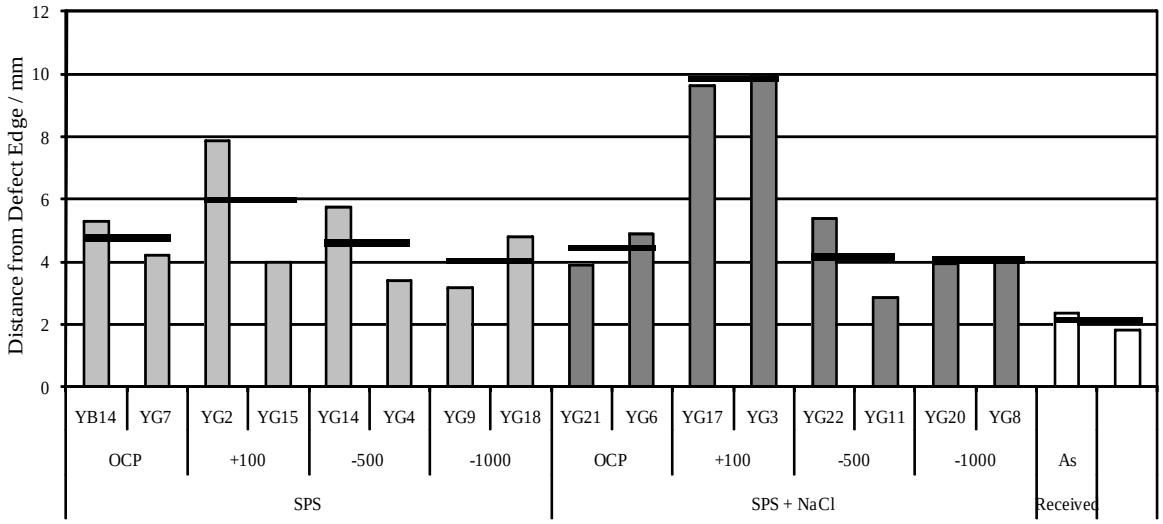

Figure 31: Average Coating Disbondment Radius Results. Average of duplicate specimens shows by the horizontal line.

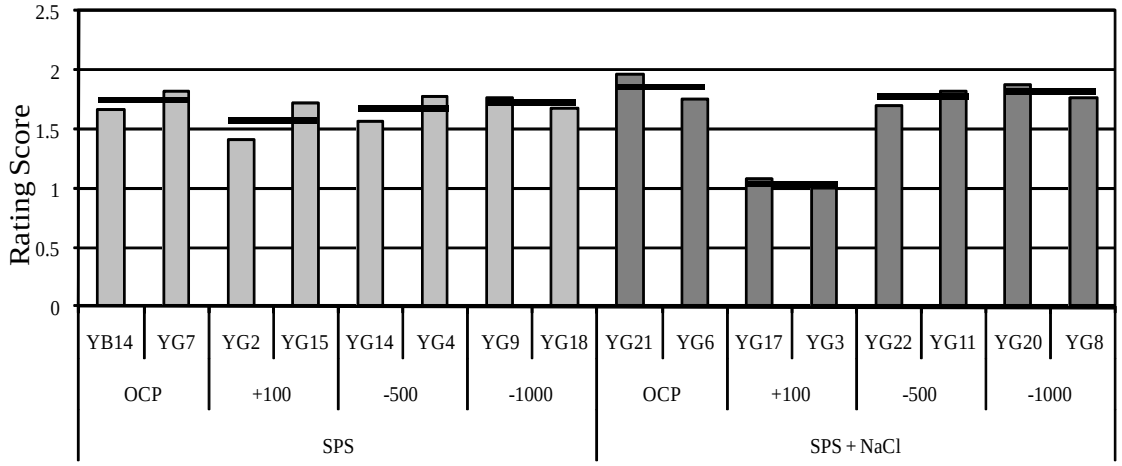

Figure 32: Average Qualitative Adhesion Loss Rating Results. Average of duplicate specimens shows by the horizontal line.

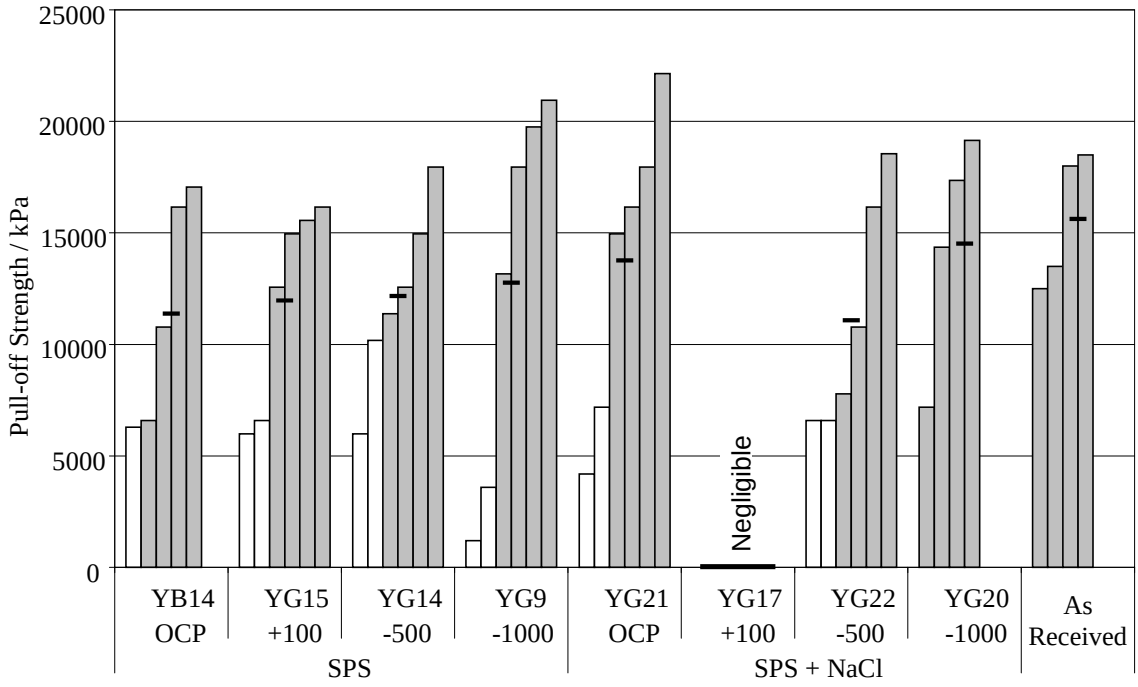

Figure 33: Nominal Coating Pull-off Strength Results. The white bars indicate a failure of the cyanoacrylate bond. Average of duplicate specimens shows by the horizontal line.

Figure 34: Discolored Area Around Defect Observed for the +100 mV Chloride Exposure Specimens. Specimen YG3.

Chapter 5
Conclusions

The following conclusions apply to dual coated reinforcing steel with moderate damage simulated with defects extending through the polymer epoxy coating layer exposing the zinc layer:

DCR with defects penetrating through the polymer layer exposing but not penetrating through the zinc layer ("to-zinc" defects) had extensive corrosion damage when under strong anodic polarization and exposed to chlorides. The extent of corrosion was similar to that seen earlier in DCR with defects penetrating through both the polymer and zinc layers exposing the steel ("to-steel" defects). DCR with both to-zinc and to-steel defects exhibited less corrosion than did ECR under the same conditions. The difference in the extent of corrosion between ECR and DCR may be due to less voluminous corrosion product build up under the coating and, therefore, less surrounding coating disbondment.

The freely corroding (OCP) through-polymer DCR specimens in solutions both with and with no-chlorides experienced initially very active dissolution which ended after ~1 day. The zinc exposed at the coating breaks was not completely consumed even after 100 days and there was no visible corrosion product accumulation.

These observations are consistent with the development of a passive regime with formation of a calcium hydroxyzincate film. The mechanism for passivation seems to be active even without the possible beneficial occluded environment factors that were noted for to-steel defects in the Phase 1 investigation.

The DCR with to-zinc defects had comparable disbondment results for most polarization regimes both with and with no-chlorides. The notable difference was the +100 mV chloride exposure tests which had more extensive disbondment due to active corrosion during the test and the formation of solid corrosion product under the coating. The DCR with to-steel defects and the DCR with to-zinc defects had similar amounts of disbondment for all test conditions.

The present findings are encouraging in demonstrating an ability of the zinc layer to withstand the nominally highly aggressive alkaline test medium used here, even when the layer is freely exposed. These results suggest then that the overall process of zinc wastage in DCR in concrete pore water is not likely to be rapid, which would be beneficial to extending the period in which the barrier and galvanic properties of the zinc are maintained. Evaluation in concrete and sustained field experience is needed to assess overall performance of DCR.

References

Accardi, Adrienne. “Exploring In-Crevice Zinc Passivation with High pH External Environment.” NACE Corrosion 2009 Conference and Expo. Student Poster Session submission. Atlanta, GA.

Andrade, Carmen and Alonso, Cruz. “Chapter 5: Electrochemical Aspects of Galvanized Reinforcement Corrosion.” *Galvanized Steel Reinforcement in Concrete.* Ed. Stephen R. Yeoman. Pgs 111-144. Elsevier. 2004.

ASTM Standard A 1055. “Standard Specification for Zinc and Epoxy Dual Coated Steel Reinforcing Bars.” ASTM International. 2008.

Bentur, A., Diamond, S., and Berke, N.S., *Steel Corrosion in Concrete: Fundamentals and Civil Engineering Practice.* E & FN Spon. New York. 1997.

Broomfield, John P. *Corrosion of Steel in Concrete: Understanding, Investigation, and Repair*. E & FN Spon. New York. 1998.

Castro, P., Sagüés, A.A., Moreno, E.I., and Genesca, J. “Characterization of Activated Titanium Solid Reference Electrodes for Corrosion Testing Of Steel in Concrete.” Corrosion. Vol. 52. No 8. Pages 609-617. NACE International. Houston, TX. August 1996.

Clear, Kenneth C. “Effectiveness of Epoxy Coated Reinforcing Steel.” Final Report. Canadian Strategic Highway Research Program. March 1992.

Clemena, Gerardo G. “Interim Report: Investigation of the Resistance of Several New Metallic Reinforcing Bars to Chloride-Induced Corrosion in Concrete.” Virginia Transportation Research Council. Virginia. December 2003.

Cui, Fushuang, Lawler, John, and Krauss, Paul. “Corrosion Performance of Epoxy-Coated Reinforcing Bars in Marine Environment.” Paper No. 07286. NACE International. Houston, TX. 2007.

Darwin, David, Browning, JoAnn, Locke, Jr., Carl E., and Nguyen, Trung V. “Multiple Corrosion Protection Systems for Reinforced Concrete Bridge Components.” Federal Highway Administration. Interim Report. July 2007.

Derucher, Kenneth N., Ezeldin, A. Samer, and Korfiatis, George P. *Materials for Civil and Highway Engineers, 3rd Edition*. Prentice Hall. New Jersey. 1994.

Fanous, Fouad S. and Wu, Han-Cheng. "Service Life of Iowa Bridge Decks Reinforced with Epoxy-Coated Bars." Mid-continent Transportation Symposium Proceedings. Center for Transportation Research and Education Iowa State University. Pgs 259-262. 2000.

Fontana, Mars G. and Greene, Norbert D. *Corrosion Engineering: Second Edition.* McGraw-Hill Book Company. New York. 1978.

Griffith, Andrew and Laylor, H. Martin. "Epoxy Coated Reinforcement Study." Final Report. Oregon Department of Transportation. June 1999.

Hime, W.G. and Machin, M. "Performance Variances of Galvanized Steel in Mortar and Concrete." Corrosion. Volume 49. No. 10. 1993.

Jones, Denny. "Principles and Prevention of Corrosion: Second Edition." Prentice Hall. New Jersey. 1996.

Koch, Gerdardus H., Brongers, Michael P. H., Thompson, Neil G., Virmani, Y. Paul. And Payer, J. H. "Corrosion Costs and Preventative Stratagies in the United States." Federal Highway Administration. Publication No. FHWA-RD-01-156. Printed in a supplemental to Materials Performance. NACE International. July 2002.

Langill, Thomas J. and Dugan, Barry. "Chapter 4: Zinc Materials for Use in Concrete." *Galvanized Steel Reinforcement in Concrete.* Ed. Stephen R. Yeoman. Pgs 87-109. Elsevier. 2004.

Lau, Kingsley and Sagues, Alberto A. "Corrosion of Epoxy- and Polymer/Zinc- Coated Rebar in Simulated Concrete Pore Solution." Corrosion. Vol. 65 No 10. Page 681. 2009.

Manning, David G. "Corrosion Performance of Epoxy-Coated Reinforcing Steel: North American Experience." Construction and Building Materials. Vol. 10 No. 5 Pgs. 349-365. 1996.

Moreno, Eric I. and Sagues, Alberto A. "Performance of Alternative Material Rebar." Final Report. FDOT. May 1996.

Nguyen, T. and Martin, J.W. "Modes and Mechanisms of Degradation of Epoxy-Coated Reinforcing Steel in Marine Environment." Durability of Building Materials and Components 7. Vol. 1. Pgs 491-507. 1996.

Nguyen, Tinh and Martin, Jonathan W. "Modes and Mechanisms for the Degradation of Fusion-Bonded Epoxy-Coated Steel in a Marine Concrete Environment." JCT Research. Vol. 1 No. 2. Pgs 81-92. April 2004.

Ohta, T. “Corrosion of Reinforcing Steel in Concrete Exposed to Sea Air.” Durability of Concrete. Pg. 459-478. V. M. Malhorta, Ed. Second International Conference. Monteal, CA. 1991.

Orazem, Mark E. and Tribollet, Bernard. *Electrochemical Impedance Spectroscopy.* John Wiley and Sons, Inc. New Jersey. 2008.

Parker, Harry. *Simplified Design of Reinforced Concrete, 3rd Edition*. John Wiley & Sons. New York. 1968.

Pianca, F. and Schell, H. “The Long Term Performance of Three Ontario Bridges Constructed with Galvanized Reinforcement.” Ontario Ministry of Transportation. Ontario, CA. 2005.

Pourbaix, Marcel. “Atlas of Electrochemical Equilibria in Aqueous Solutions.” National Association of Corrosion Engineers. Houston, TX. 1974.

Pyć, Wioleta A., Weyers, Richard E., Weyers, Ryan M., Mokarem, David W., and Zemajtis, Jerzy. “Filed Performance of Epoxy-Coated Reinforcing Steel in Virginia Bridge Decks.” Final Report #00-R16. VTRC. February 2000.

Sagüés, Alberto A. “Corrosion of Epoxy-Coated Reinforcing Steel (Phase 1)” Final Report. FL/DOT/SMO/89-419. Florida Department of Transportation. December 1989.

Sagüés, Alberto A. and Powers, Rodney G. “Coating Disbondment in Epoxy-Coated Reinforcing Steel in Concrete – Field Observations.” NACE Corrosion Conference. Paper #325. 1996.

Sagüés, Alberto A., et al. “Corrosion of Epoxy Coated Rebar in Florida Bridges.” Final Report. WPI no. 0510603, Florida Department of Transportation. May 1994.

Sagüés, Alberto A., Powers, Rodney G. and Kessler, Richard J. “Corrosion of Epoxy-Coated Rebar in Marine Bridges – A 30 Year Perspective.” Paper No. 4039, Proceedings of the 17th International Corrosion Congress ,“Corrosion Control in the Service of Society”, October 6-10, 2008, Las Vegas, Nevada, Published by NACE International, Houston, 2009.

Smith, Jeffrey L., and Virmani, Yash Paul. “Performance of Epoxy-Coated Rebars in Bridge Decks.” US Department of Transportation and the Federal Highway Administration. Public Roads Online. Vol. 60 No. 2. Fall 1996.

Videm, Ketil. “Behavior of Zinc in Synthetic Concrete Pore Water and in Cement Mortar.” The European Federation of Corrosion. EUROCORR. Rive, Italy. 2001.

Yeomans, S.R. “Performance of Black, Galvanized, and Epoxy-Coated Reinforcing Steels in Chloride-Contaminated Concrete.” NACE International. Corrosion. Vol. 50 No. 1. Pgs 72-81. Houston, TX. January 1994.

Appendices

Appendix 1: Impedance Diagrams

Tables 6 and 7 include the EIS fit parameters obtained for each of the four OCP specimens evaluated (designated by identifiers per Table 3). The blue highlighted entries are for a fit using the circuit in Figure 11. Entries not highlighted resulted from a fit to the circuit in Figure 8 with the modification indicated in Chapter 4. Yellow highlighted entries denote the few instances in which no adequate fit could be obtained by either approach. Fitting procedures involved working assumptions. Refer to Chapter 4 for limitations on the significance of the values obtained by these procedures.

Bode and Nyquist EIS representations of the EIS results for each sample tested and for the indicated exposure time are shown in Figures 35 to 114.

Appendix 1: (Continued)

Table 6: Impedance Fit Data for Chloride Specimens

YG6	Chloride					CPEm			CPEc	
Date	Time (Days)	Test ID	Eoc (mV)	Rp	Rs	YoM	nM	Rb	YoC	nC
2/17/09 15:18	0.06	a	-1398	2.69E+03	1.11E+01	2.13E-03	8.93E-01	3.13E+03	2.51E-04	3.37E-01
2/17/09 16:09	0.09	b	-1364	3.34E+04	2.14E+01	4.47E-05	7.58E-01	5.35E+02	9.16E-05	0.479
2/17/09 16:58	0.13	c	-1169							
2/18/09 10:17	0.85	d	-754	2.84E+05	0	6.44E-05	5.53E-01			
2/18/09 19:06	1.22	e	-702	2.56E+05	0	5.71E-05	5.95E-01			
2/19/09 12:15	1.93	f	-659	3.04E+05	0	5.28E-05	6.27E-01			
2/20/09 15:33	3.07	g	-659	2.86E+05	0	5.52E-05	6.57E-01			
2/23/09 13:15	5.97	h	-649	2.78E+05	727.5	6.19E-05	6.94E-01			
2/27/09 12:18	9.93	i	-680	3.32E+05	111.8	7.01E-05	6.65E-01			
3/2/09 14:00	13.00	j	-671	3.59E+05	711.6	7.64E-05	6.66E-01			
3/31/09 13:51	42.00	k	-606	5.23E+06	2.97E+03	1.23E-04	5.93E-01			
5/5/09 9:51	76.83	l	-558							
5/14/09 12:05	85.92	m								
YG21	Chloride					CPEm			CPEc	
Date	Time (Days)	Test ID	Eoc (mV)	Rp	Rs	YoM	nM	Rb	YoC	nC
2/17/09 15:06	0.05	a	-1383	2.37E+03	2.42E+01	1.65E-03	0.791	2.97E+03	1.14E-04	0.443
2/17/09 15:57	0.08	b	-1358	1.68E+04	26.31	1.61E-05	0.897	922.3	1.23E-04	0.448
2/17/09 16:48	0.12	c	-1305	3.08E+04	28.53	4.40E-05	7.51E-01	557.6	8.21E-05	0.496
2/18/09 10:08	0.84	d	-773	2.93E+05	0	8.34E-05	5.62E-01			
2/18/09 18:55	1.21	e	-701	3.16E+05	0	6.88E-05	5.64E-01			
2/19/09 12:06	1.92	f	-741	3.47E+05	0	8.22E-05	5.90E-01			
2/20/09 15:24	3.06	g	-742	3.41E+05	0	8.80E-05	6.04E-01			
2/23/09 12:36	5.95	h	-681	4.55E+05	0	8.17E-05	6.16E-01			
2/27/09 12:02	9.92	i	-634	5.43E+05	0	8.05E-05	6.19E-01			
3/2/09 13:42	12.99	j	-635	6.63E+05	0	8.59E-05	6.21E-01			
3/31/09 13:34	41.99	k	-551	3.35E+05	2.93E+03	1.39E-04	6.74E-01			
5/5/09 9:43	76.83	l	-542	1.39E+06	3.37E+03	1.50E-04	6.43E-01			
5/14/09 11:55	85.92	m		2.20E+06	2.41E+03	1.81E-04	6.37E-01			

Appendix 1: (Continued)

Table 7: Impedance Fit Data for No-chloride Specimen

YB14	No Chloride					CPEm			CPEc	
Date	Time (Days)	Test ID	Eoc (mV)	Rp	Rs	YoM	nM	Rb	YoC	nC
1/27/09 12:13	0.04	a	-1398	374.9	16.45	4.78E-03	0.6861	804.5	3.32E-05	0.6697
1/27/09 13:50	0.10	b	-1389	260.4	17.07	1.32E-02	1.002	826.4	8.52E-05	0.6002
1/27/09 15:30	0.17	c	-1375	430.8	16.25	1.23E-02	0.8349	828.4	1.82E-04	0.5281
1/27/09 16:34	0.22	d	-1362	655	16.41	9.23E-03	0.7362	977	3.13E-04	0.4905
1/28/09 10:20	0.96	e	-711	1.35E+05	1.70E+03	3.80E-04	7.20E-01			
1/28/09 12:00	1.03	f	-694	2.20E+05	1.28E+03	3.22E-04	6.76E-01			
1/28/09 15:41	1.18	g	-685	2.67E+05	1.32E+03	2.97E-04	6.93E-01			
1/29/09 11:24	2.00	h	-713	4.79E+05	1.29E+03	2.80E-04	6.80E-01			
1/30/09 10:06	2.95	i	-679	3.61E+05	1.30E+03	2.57E-04	6.88E-01			
2/2/09 9:49	5.94	j	-753							
2/3/09 11:15	7.00	k	-718	2.18E+06	914.9	2.72E-04	0.6725			
2/4/09 10:10	7.95	l	-704	1.35E+06	952.8	2.55E-04	0.677			
2/6/09 9:45	9.93	m	-602	4.63E+05	1.18E+03	2.10E-04	6.84E-01			
2/7/09 9:43	10.93	n	-600	5.20E+05	1.19E+03	2.05E-04	6.93E-01			
2/9/09 10:00	12.94	o	-566	4.36E+05	1.23E+03	1.92E-04	7.00E-01			
2/10/09 11:35	14.01	p	-548	3.78E+05	1.23E+03	1.87E-04	7.04E-01			
2/12/09 11:07	15.99	q	-540	3.20E+05	1.18E+03	1.82E-04	7.09E-01			
2/13/09 10:12	16.95	r	-539	4.01E+05	908.4	1.72E-04	6.94E-01			
2/16/09 10:00	19.94	s	-539	2.79E+05	1.14E+03	1.76E-04	7.22E-01			
2/17/09 11:40	21.01	t	-530	3.23E+05	1.14E+03	1.74E-04	7.19E-01			
2/18/09 9:51	21.94	u	-543	3.31E+05	1.18E+03	1.72E-04	7.21E-01			
2/19/09 13:05	23.07	v	-526	3.19E+05	1.14E+03	1.74E-04	7.21E-01			
2/20/09 15:09	24.16	w	-543	3.37E+05	1.07E+03	1.72E-04	7.19E-01			
2/23/09 12:07	27.03	x	-532	4.03E+05	1.06E+03	1.65E-04	7.17E-01			
3/2/09 11:51	34.02	y	-529	4.78E+05	8.98E+02	1.57E-04	7.17E-01			
3/31/09 13:10	63.08	z	-495	3.08E+05	6.22E+02	1.59E-04	7.50E-01			
5/5/09 9:17	97.91	aa	-498	1.74E+05	8.85E+02	1.97E-04	8.23E-01			
YG7	No Chloride					CPEm			CPEc	
Date	Time (Days)	Test ID	Eoc (mV)	Rp	Rs	YoM	nM	Rb	YoC	nC
1/27/09 12:39	0.05	a	-1427	6.53E+03	2.11E+01	1.30E-03	3.75E+01	6.00E+02	5.24E-05	5.83E-01
1/27/09 14:34	0.13	b	-1412							
1/27/09 16:01	0.20	c	-1304	1.92E+04	42.24	1.81E-04	0.704	2.17E+02	8.92E-05	4.96E-01
1/27/09 17:07	0.24	d	-1077	2.89E+04	5.91E+01	1.95E-04	0.703	1.82E+02	8.06E-05	0.557
1/28/09 11:00	0.99	e	-872	5.46E+05	1.74E+03	1.62E-04	5.48E-01			
1/28/09 12:00	1.03	f	-859	2.69E+05	0	1.34E-04	5.07E-01			
1/28/09 15:59	1.19	g	-846	3.44E+05	0	1.36E-04	4.98E-01			
1/29/09 11:36	2.01	h	-790							
1/30/09 10:15	2.95	i	-798							
2/2/09 10:00	5.94	j	-780	3.39E+05	134.1	1.32E-04	5.31E-01			
2/3/09 11:28	7.01	k	-762	2.08E+06	920.9	2.71E-04	6.73E-01			
2/4/09 10:18	7.96	l	-755	1.51E+06	0	1.12E-04	4.87E-01			
2/6/09 9:53	9.94	m	-743							
2/7/09 9:51	10.94	n	-736							
2/9/09 10:07	12.95	o	-735	3.08E+06	1.00E+03	1.13E-04	5.15E-01			
2/10/09 12:45	14.06	p	-730	2.97E+06	1.17E+03	1.12E-04	5.19E-01			
2/12/09 11:15	16.00	q	-728							
2/13/09 10:20	16.96	r	-730	2.09E+06	1.61E+03	1.20E-04	5.31E-01			
2/16/09 10:10	19.95	s	-729							
2/17/09 11:49	21.02	t	-722	4.41E+07	0	1.05E-04	5.01E-01			
2/18/09 9:59	21.94	u	-722	1.51E+06	0	1.04E-04	5.08E-01			
2/19/09 13:35	23.09	v	-722	4.81E+06	0	1.06E-04	5.04E-01			
2/20/09 15:16	24.16	w	-721	1.89E+06	0	1.05E-04	5.11E-01			
2/23/09 12:18	27.04	x	-722	1.41E+06	0	1.05E-04	5.14E-01			
3/2/09 12:00	34.03	y	-724	4.87E+05	0	1.08E-04	5.42E-01			
3/31/09 13:22	63.08	z	-747	2.26E+05	0	1.67E-04	6.06E-01			
5/5/09 9:34	97.93	aa	-769	1.85E+05	0	2.90E-04	6.59E-01			

Appendix 1: (Continued)

YG6 (Chloride) Impedance Diagrams

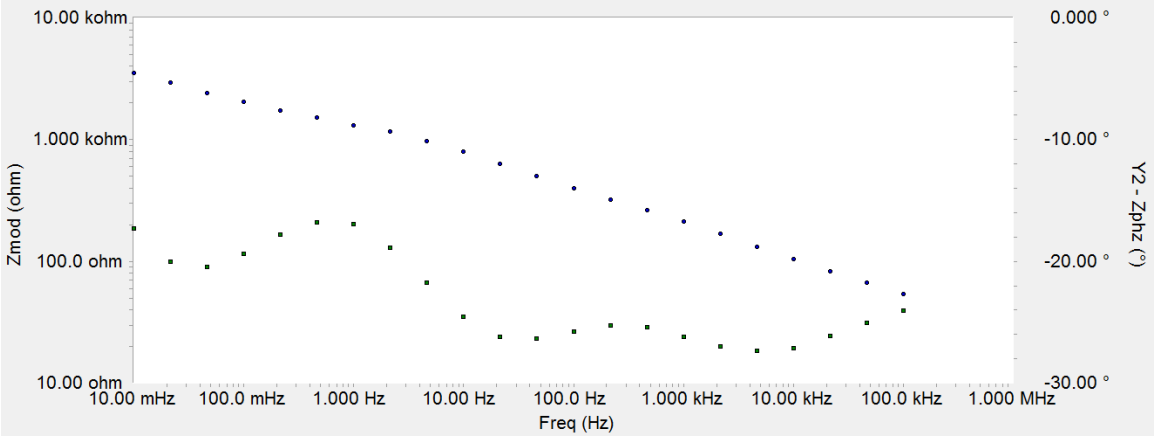

Test a (0.06 days)

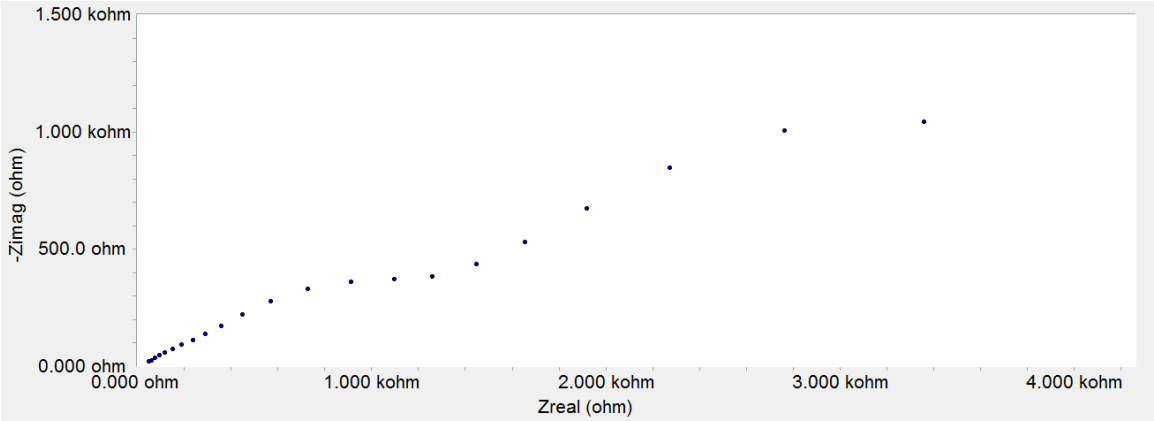

Test a (0.06 days)

Figure 35: Bode and Nyquist Diagrams for YG6 at 0.06 Days of Exposure.

Appendix 1: (Continued)

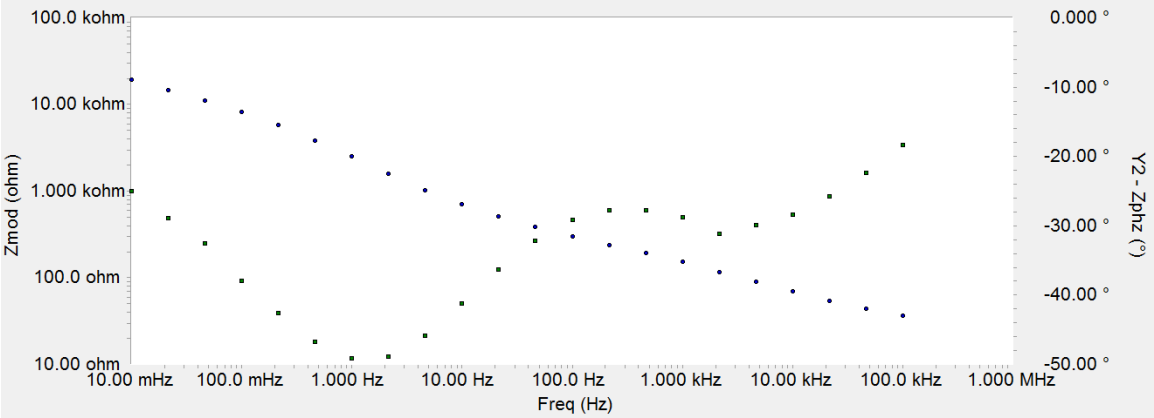

Test b (0.09 days)

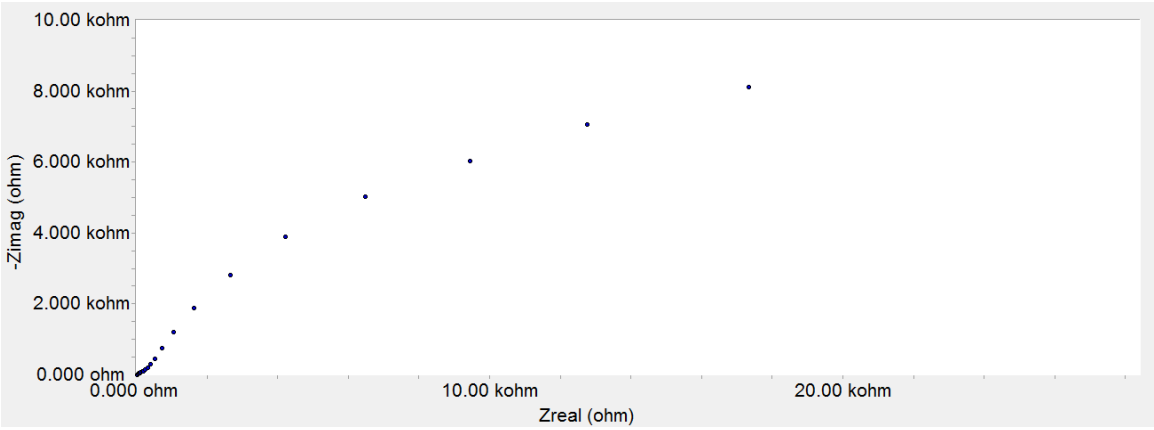

Test b (0.09 days)

Figure 36: Bode and Nyquist Diagrams for YG6 at 0.09 Days of Exposure.

Appendix 1: (Continued)

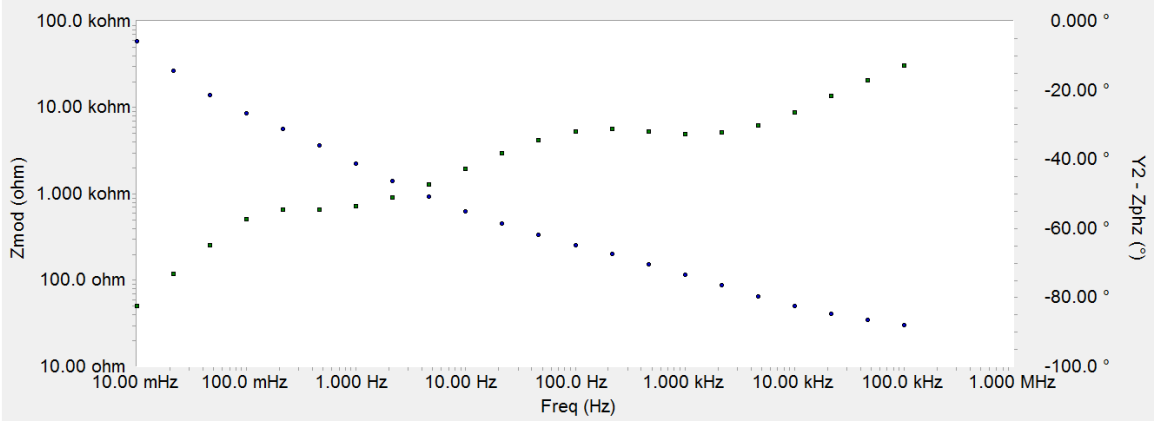

Test c (0.13 days)

Test c (0.13 days)

Figure 37: Bode and Nyquist Diagrams for YG6 at 0.13 Days of Exposure.

Appendix 1: (Continued)

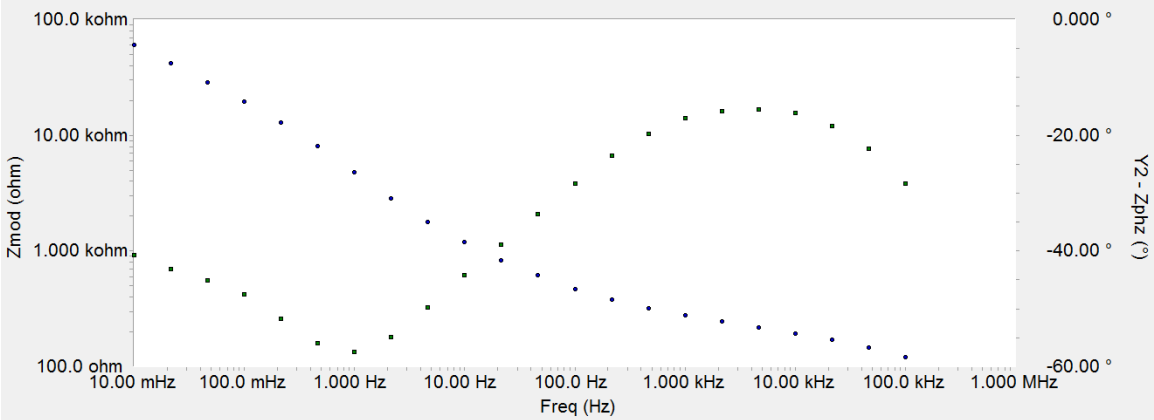

Test d (0.85 days)

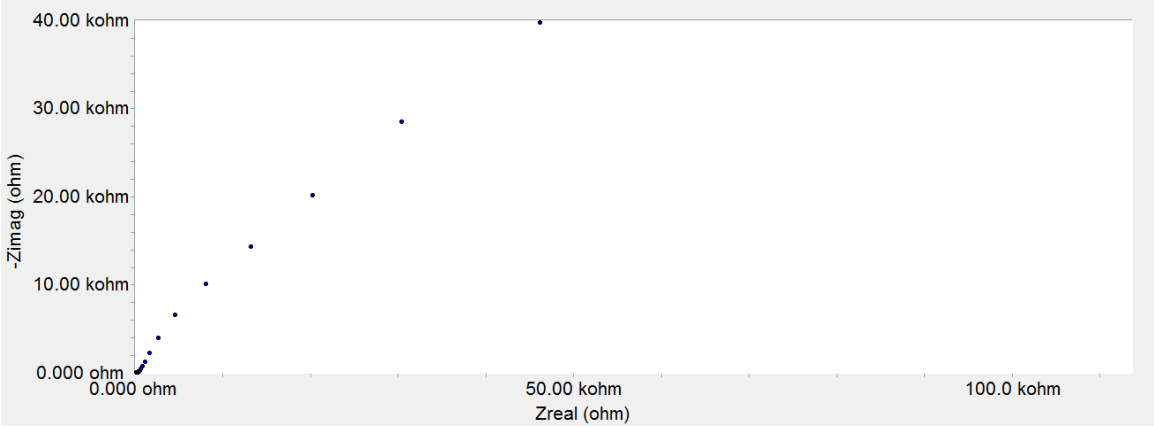

Test d (0.85 days)

Figure 38: Bode and Nyquist Diagrams for YG6 at 0.85 Days of Exposure.

Appendix 1: (Continued)

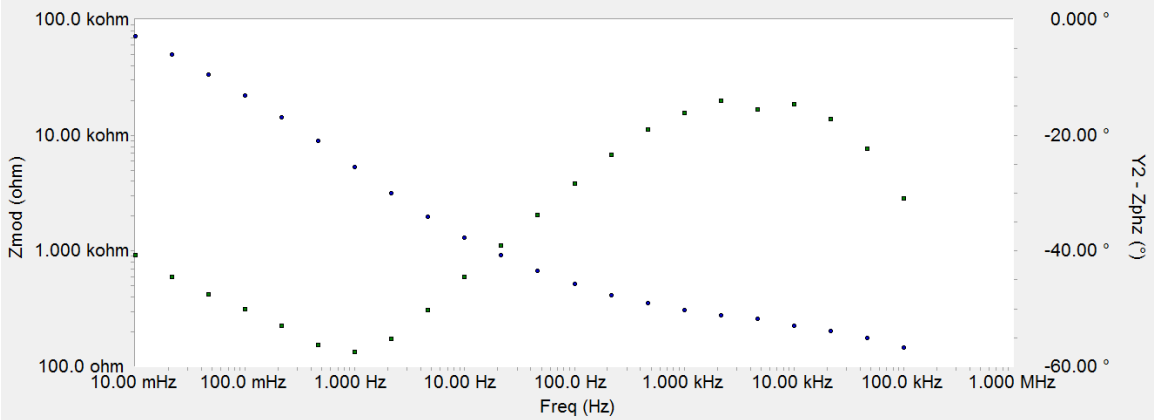

Test e (1.22 days)

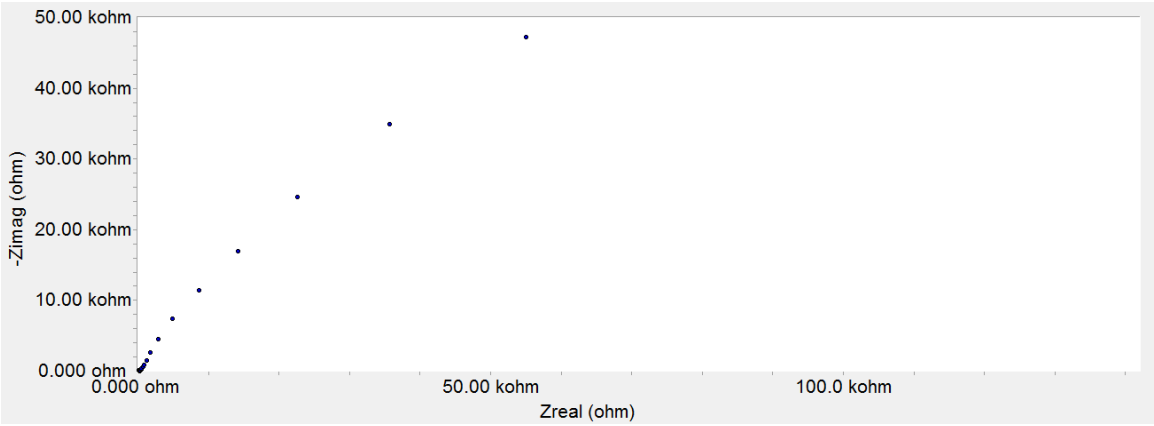

Test e (1.22 days)

Figure 39: Bode and Nyquist Diagrams for YG6 at 1.22 Days of Exposure.

Appendix 1: (Continued)

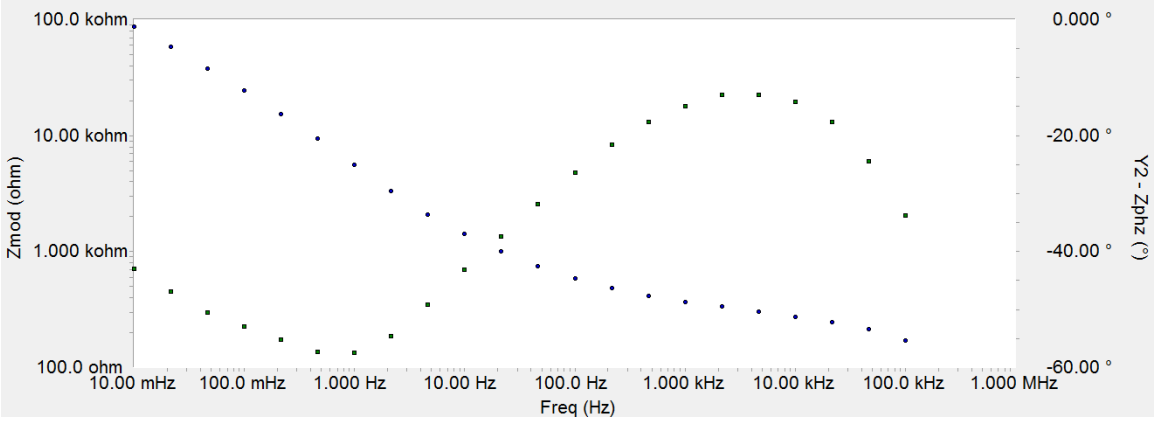

Test f (1.93 days)

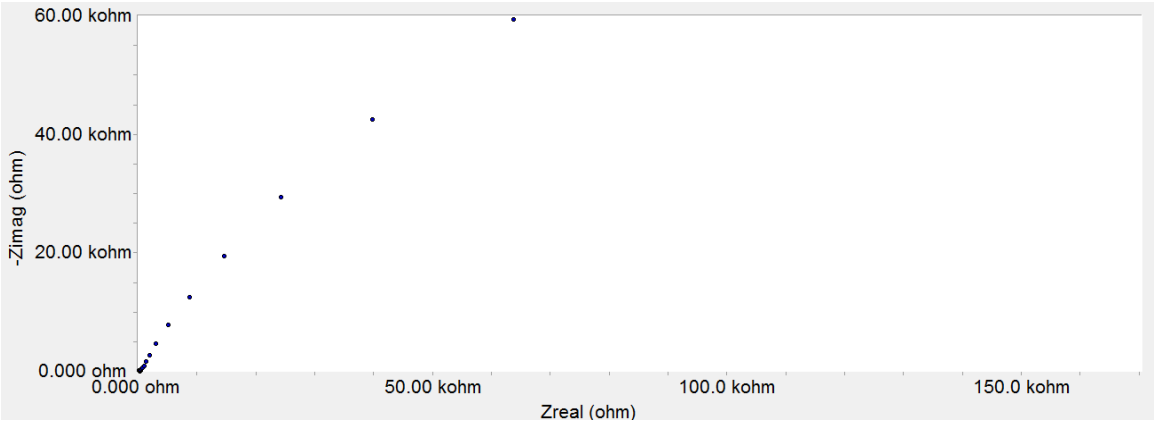

Test f (1.93 days)

Figure 40: Bode and Nyquist Diagrams for YG6 at 1.93 Days of Exposure.

Appendix 1: (Continued)

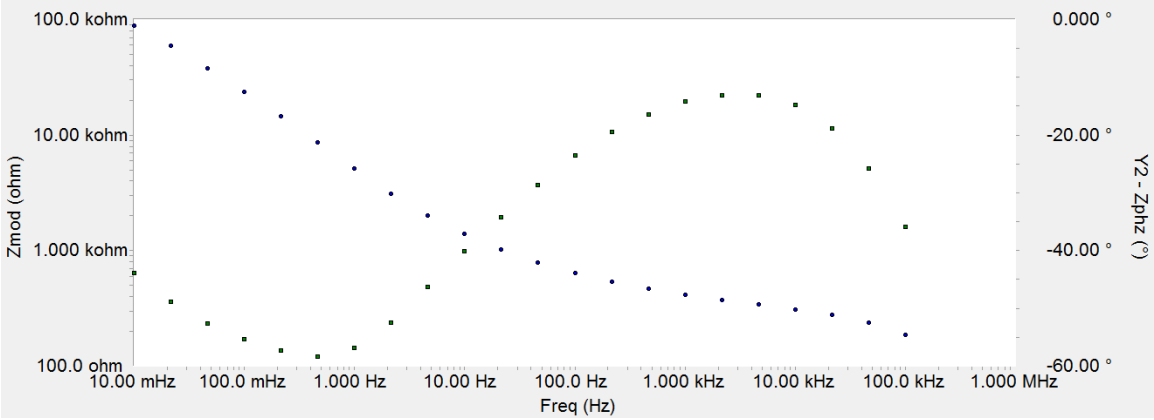

Test g (3.07 days)

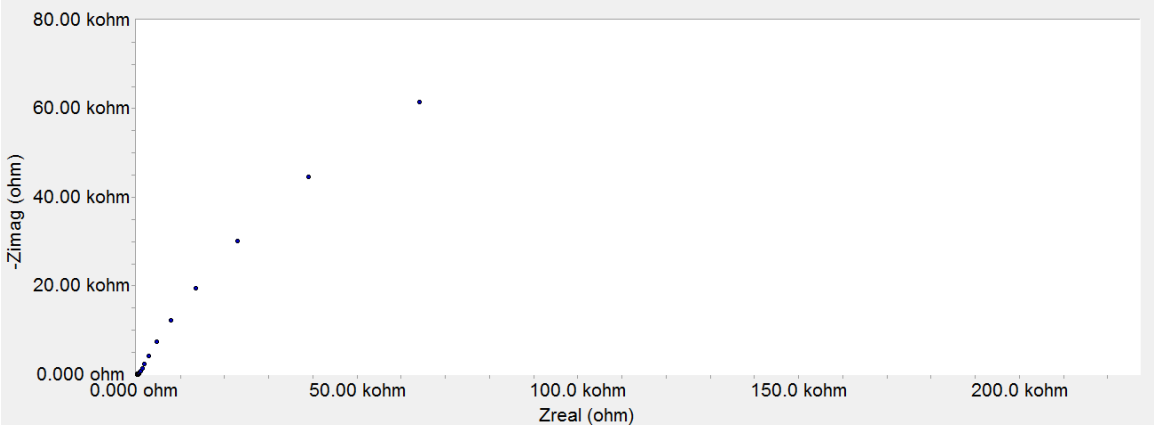

Test g (3.07 days)

Figure 41: Bode and Nyquist Diagrams for YG6 at 3.07 Days of Exposure.

Appendix 1: (Continued)

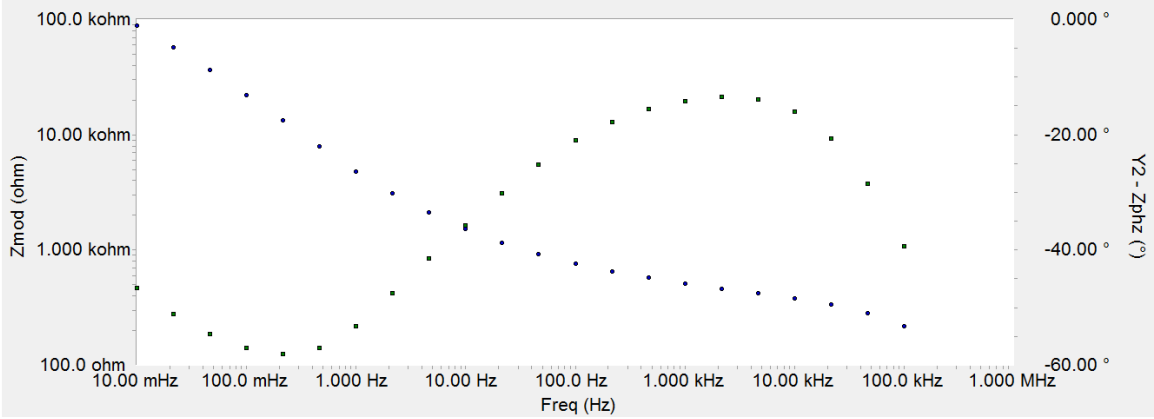

Test h (5.97 days)

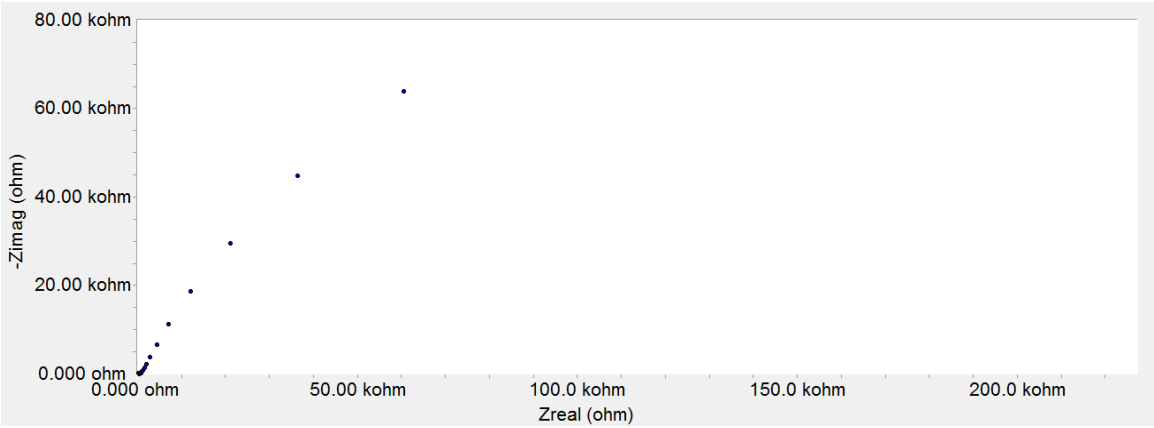

Test h (5.97 days)

Figure 42: Bode and Nyquist Diagrams for YG6 at 5.97 Days of Exposure.

Appendix 1: (Continued)

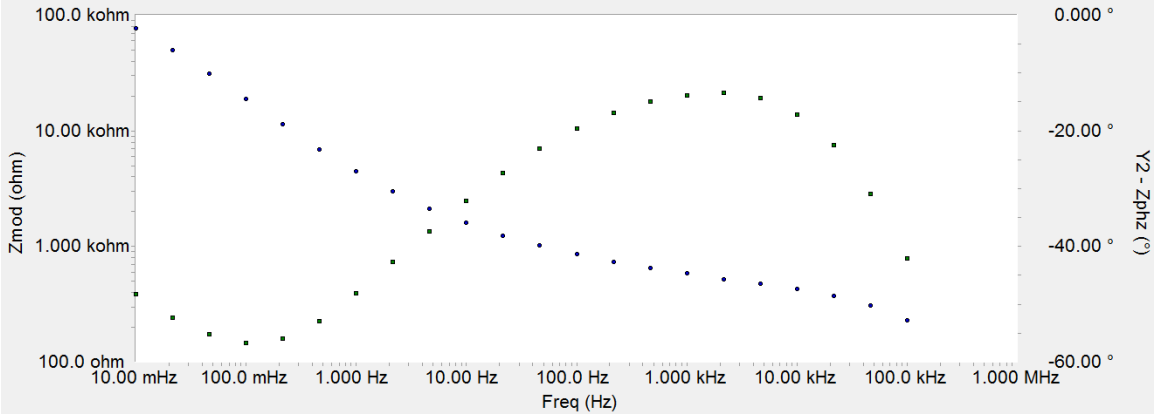

Test i (9.93 days)

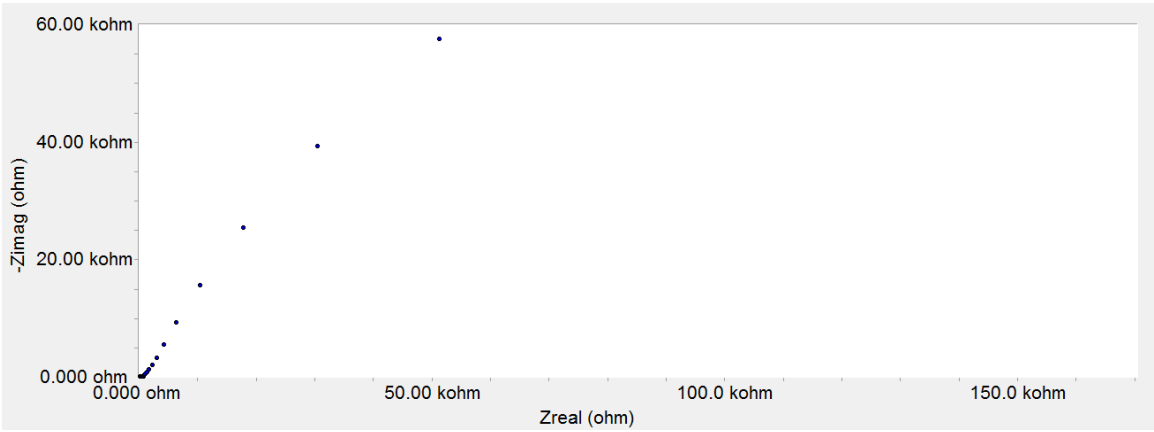

Test i (9.93 days)

Figure 43: Bode and Nyquist Diagrams for YG6 at 9.93 Days of Exposure.

Appendix 1: (Continued)

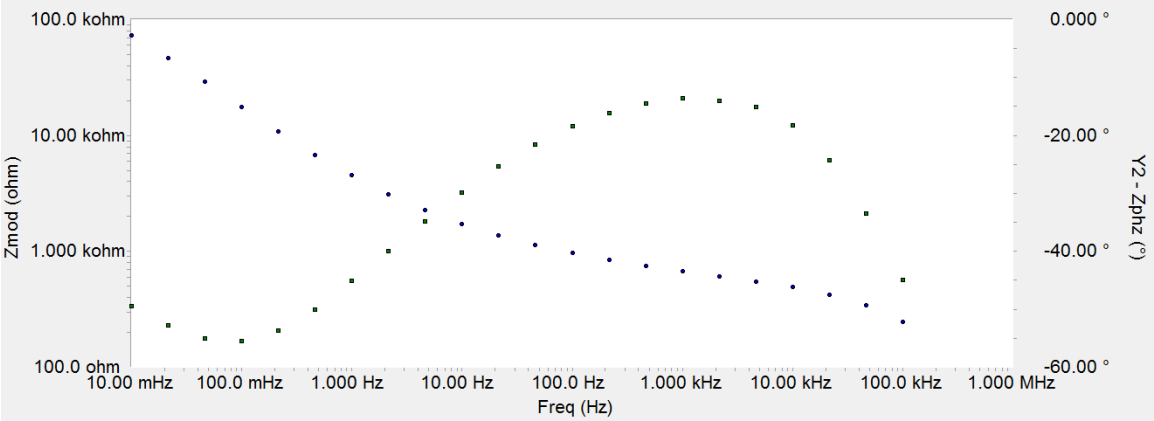

Test j (13 days)

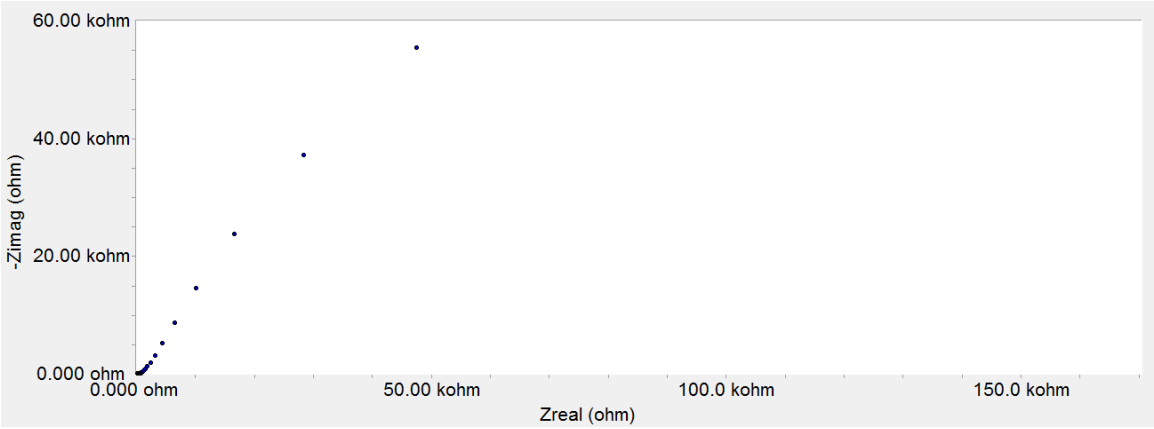

Test j (13 days)

Figure 44: Bode and Nyquist Diagrams for YG6 at 13 Days of Exposure.

Appendix 1: (Continued)

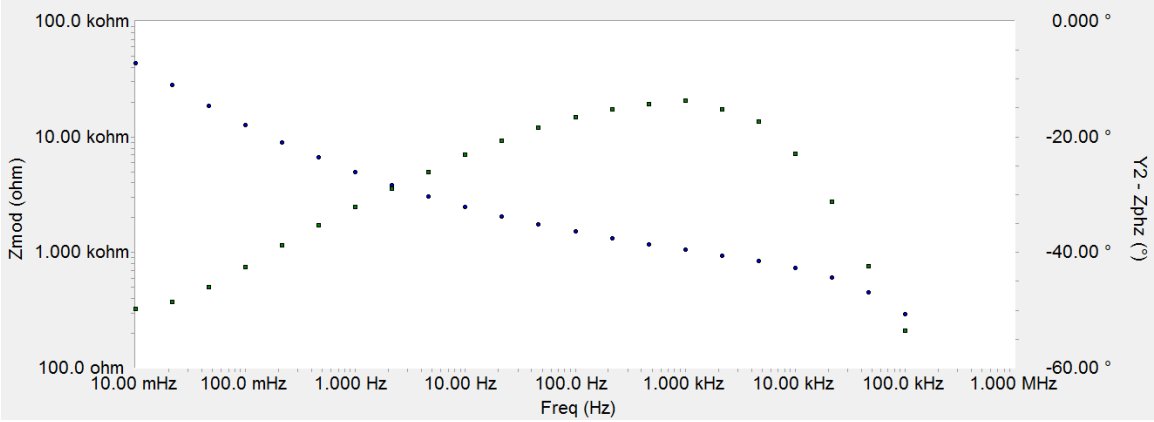

Test k (42 days)

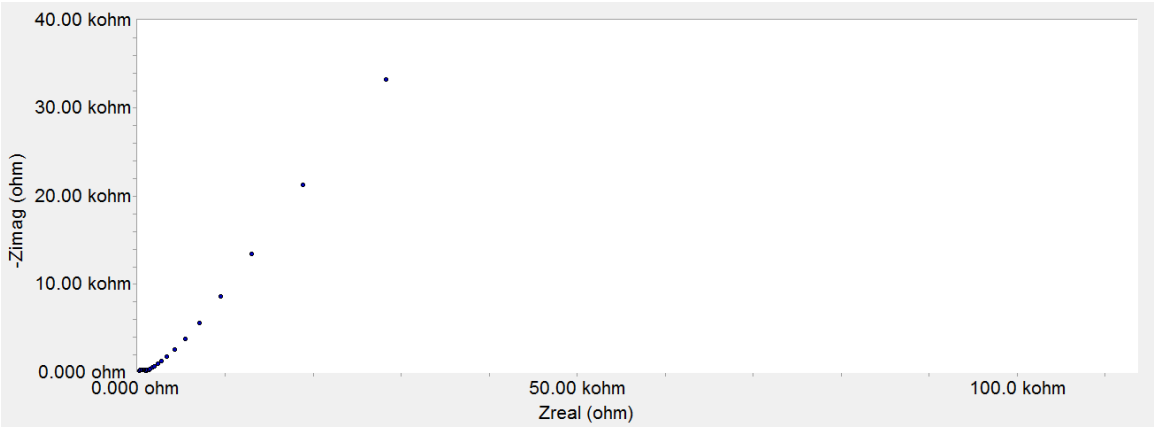

Test k (42 days)

Figure 45: Bode and Nyquist Diagrams for YG6 at 42 Days of Exposure.

Appendix 1: (Continued)

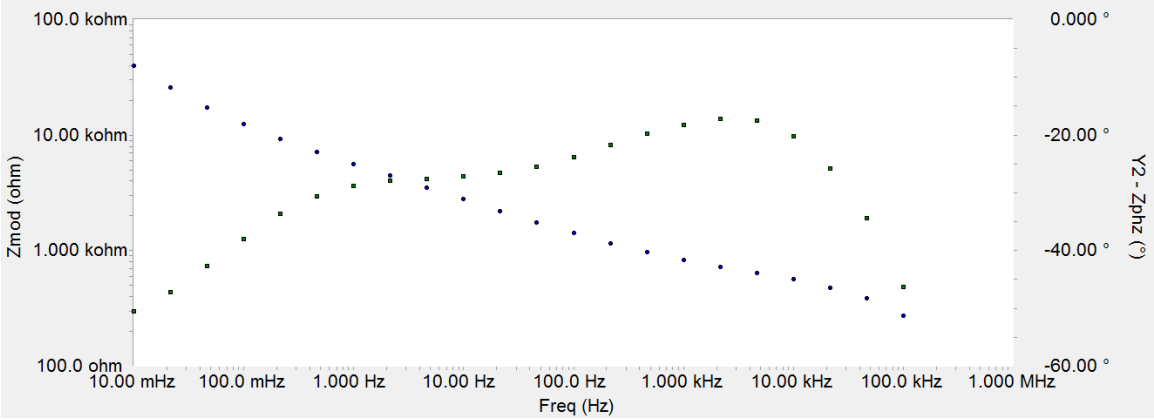

Test l (76.83 days)

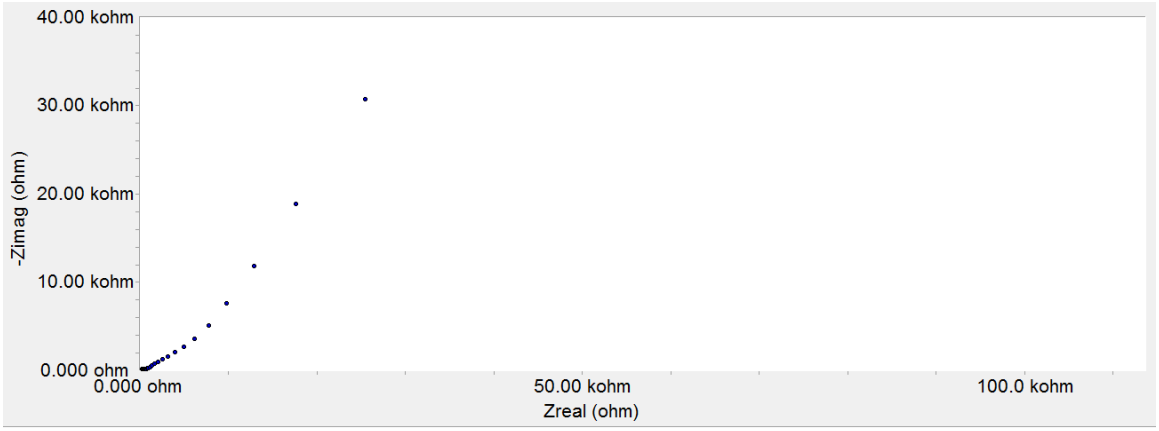

Test l (76.83 days)

Figure 46: Bode and Nyquist Diagrams for YG6 at 76.83 Days of Exposure.

Appendix 1: (Continued)

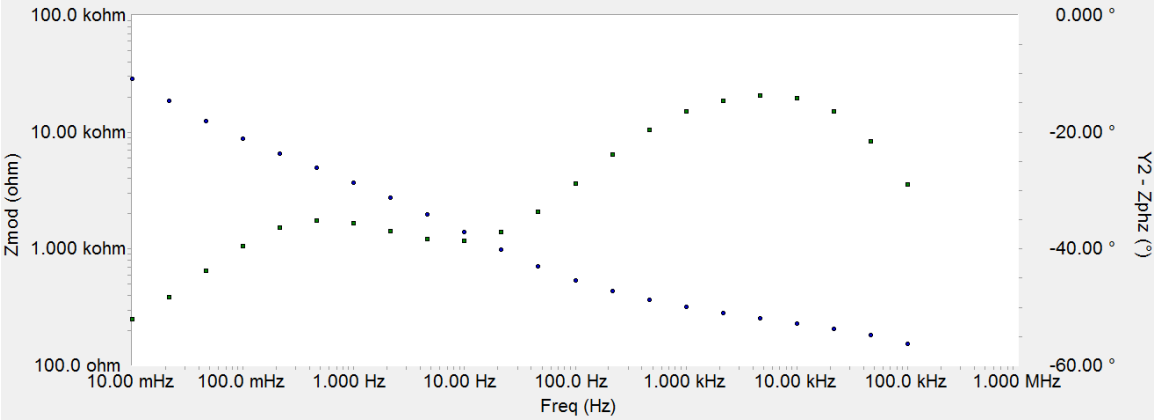

Test m (85.92 days)

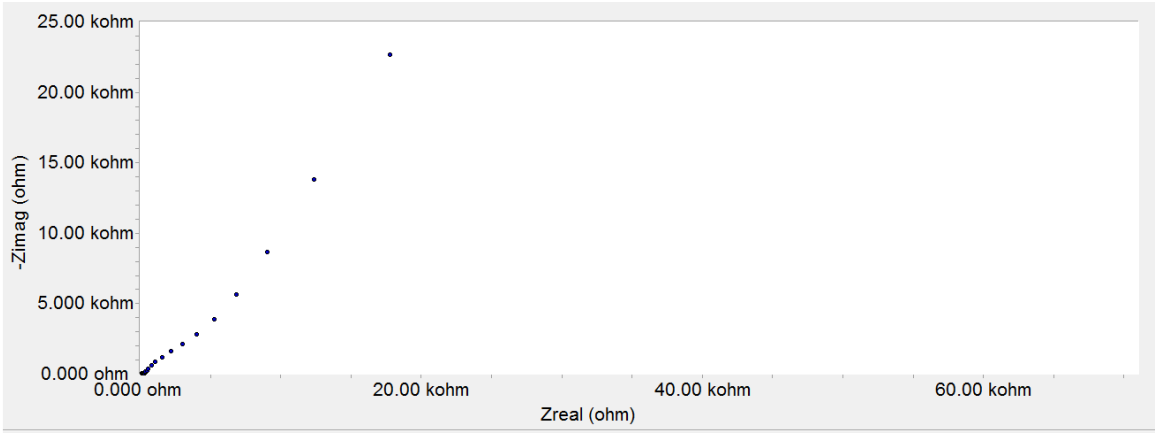

Test m (85.92 days)

Figure 47: Bode and Nyquist Diagrams for YG6 at 85.92 Days of Exposure.

Appendix 1: (Continued)

Impedance Diagrams YG21 (Chloride)

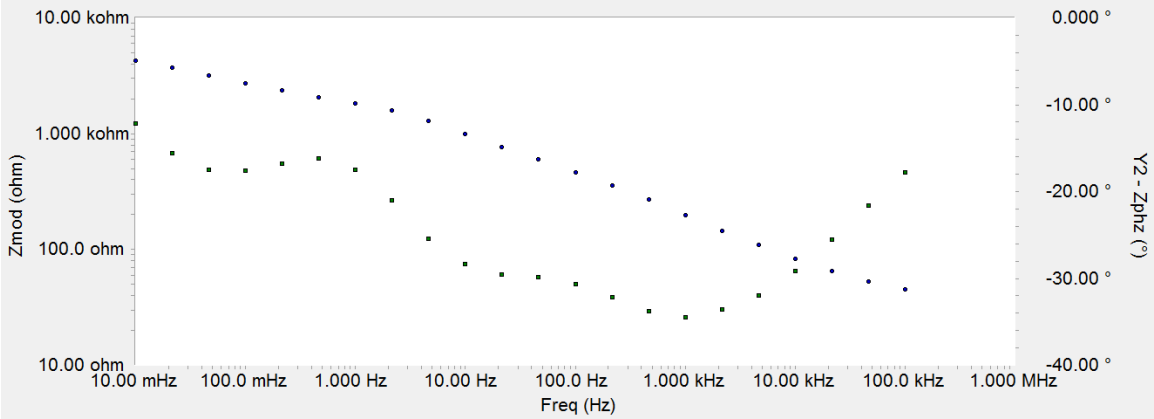

Test a (0.05 days)

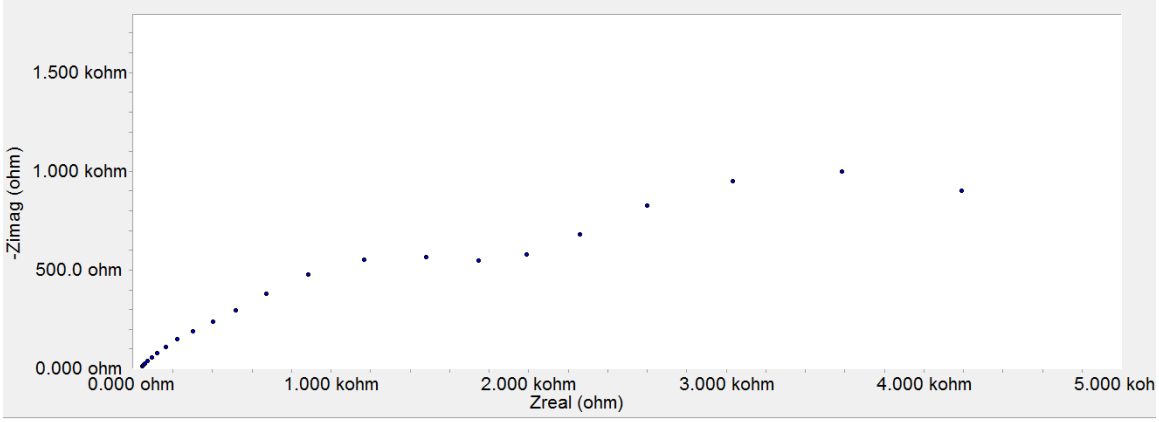

Test a (0.05 days)

Figure 48: Bode and Nyquist Diagrams for YG21 at 0.05 Days of Exposure.

Appendix 1: (Continued)

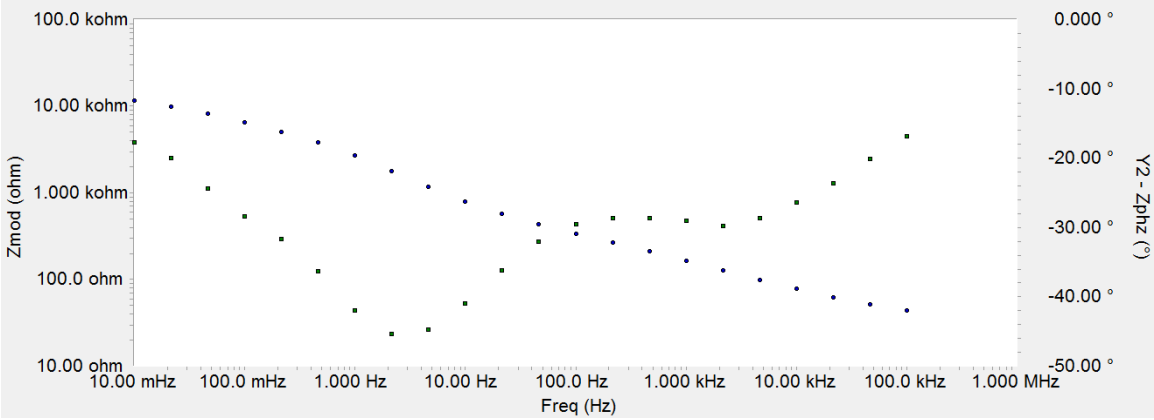

Test b (0.08 days)

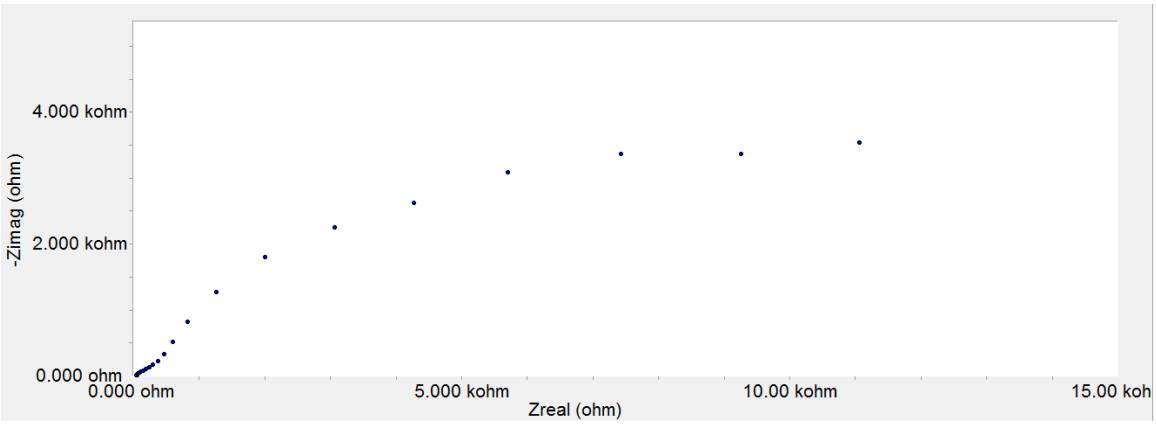

Test b (0.08 days)

Figure 49: Bode and Nyquist Diagrams for YG21 at 0.08 Days of Exposure.

Appendix 1: (Continued)

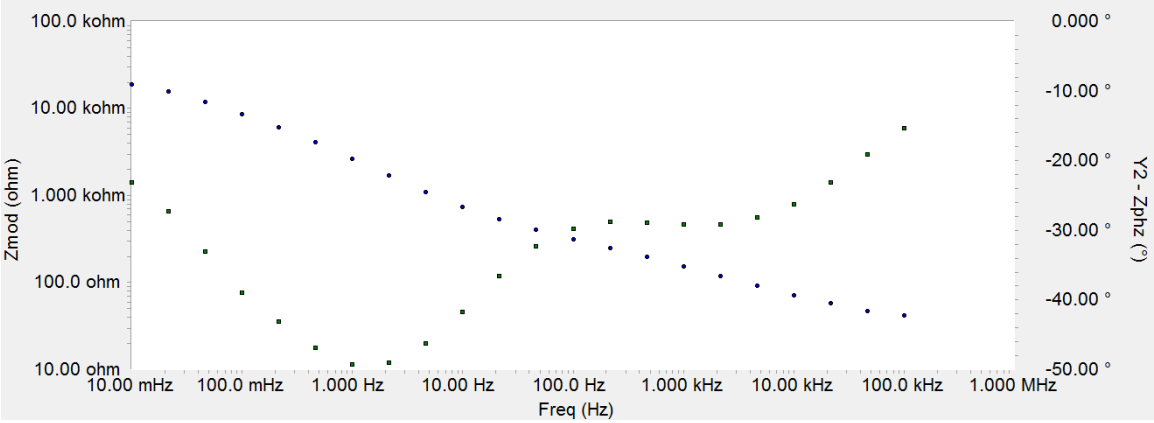

Test c (0.12 days)

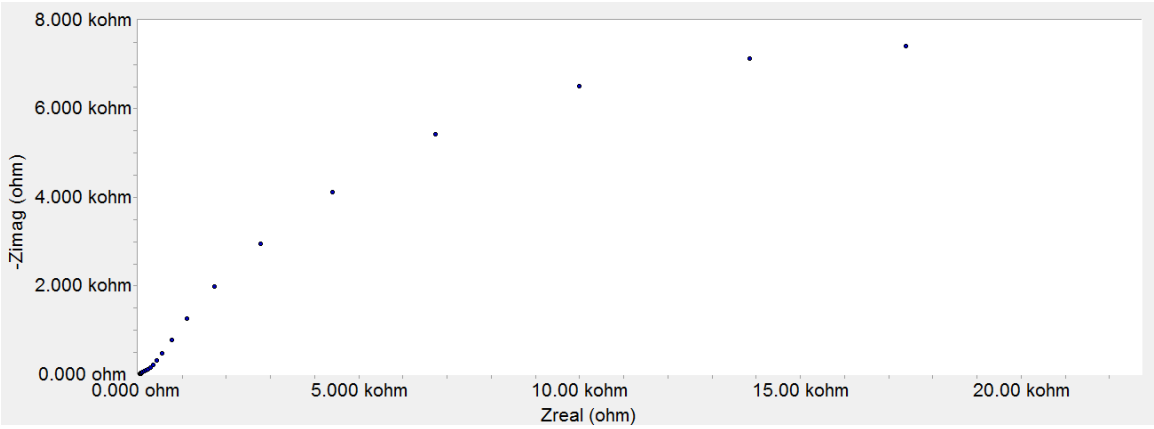

Test c (0.12 days)

Figure 50: Bode and Nyquist Diagrams for YG21 at 0.12 Days of Exposure.

Appendix 1: (Continued)

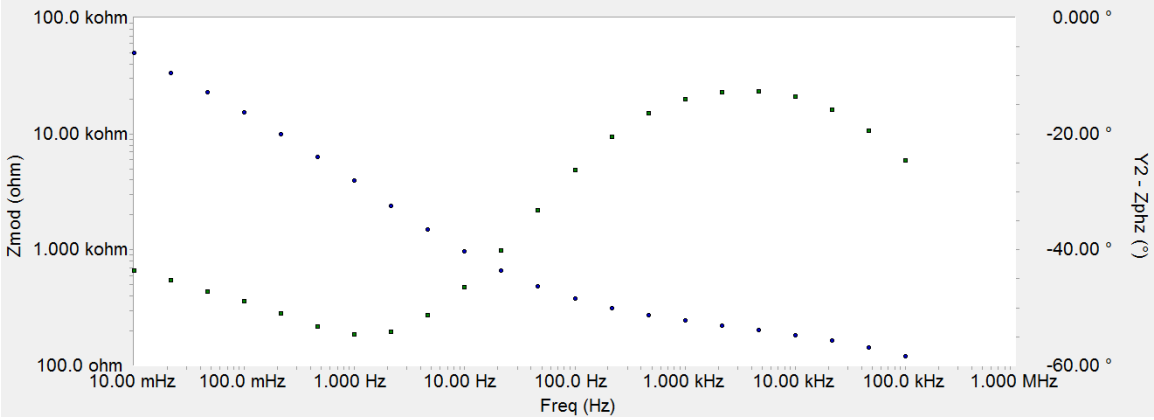

Test d (0.84 days)

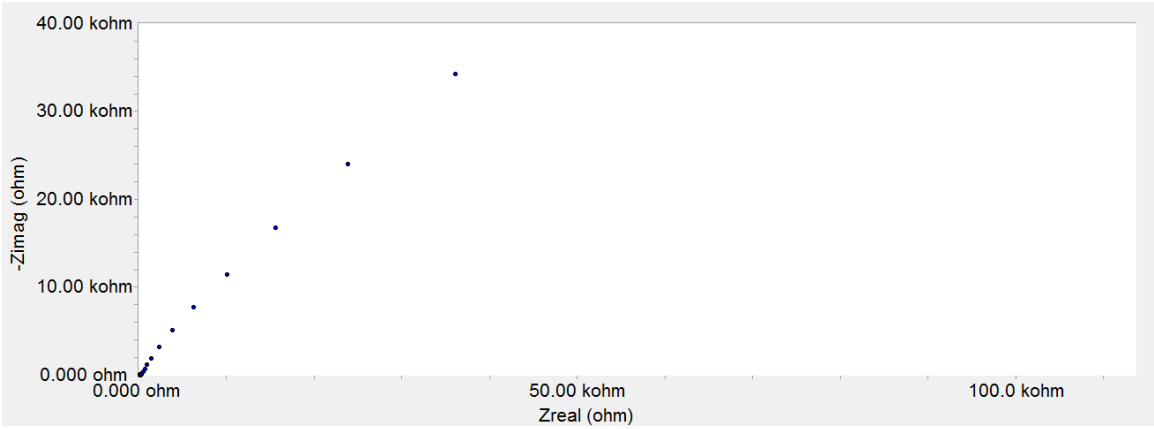

Test d (0.84 days)

Figure 51: Bode and Nyquist Diagrams for YG21 at 0.84 Days of Exposure.

Appendix 1: (Continued)

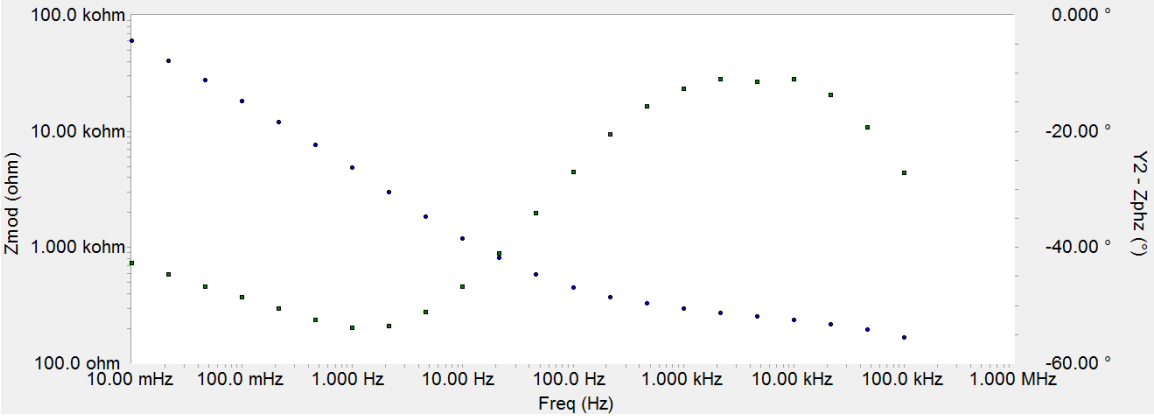

Test e (1.21 days)

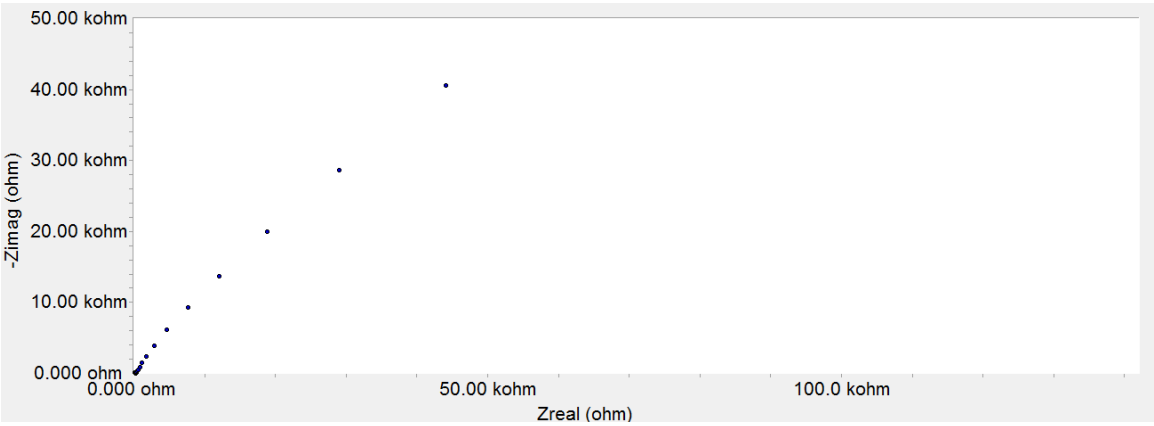

Test e (1.21 days)

Figure 52: Bode and Nyquist Diagrams for YG21 at 1.21 Days of Exposure.

Appendix 1: (Continued)

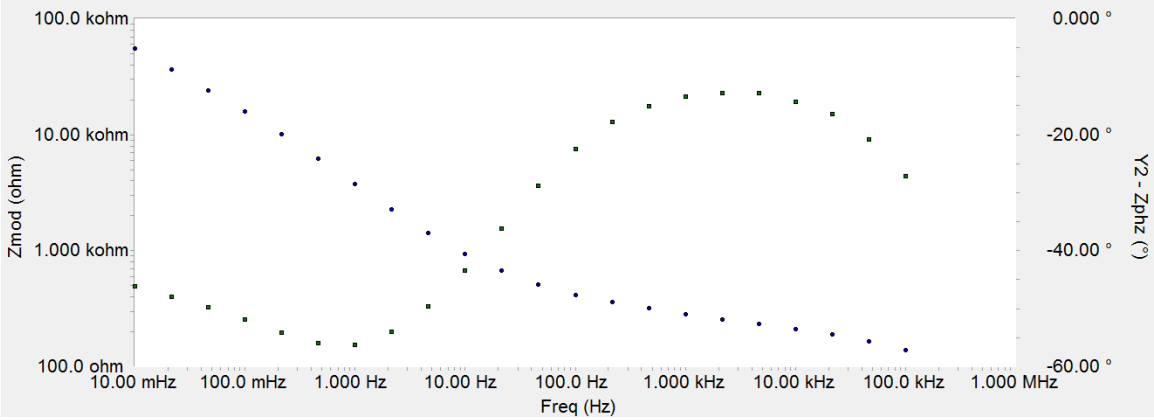

Test f (1.92 days)

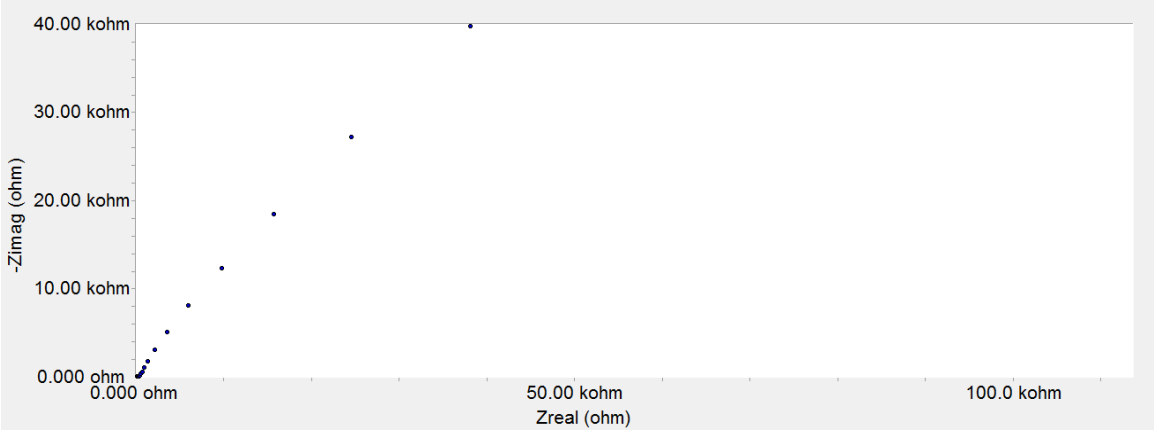

Test f (1.92 days)

Figure 53: Bode and Nyquist Diagrams for YG21 at 1.92 Days of Exposure.

Appendix 1: (Continued)

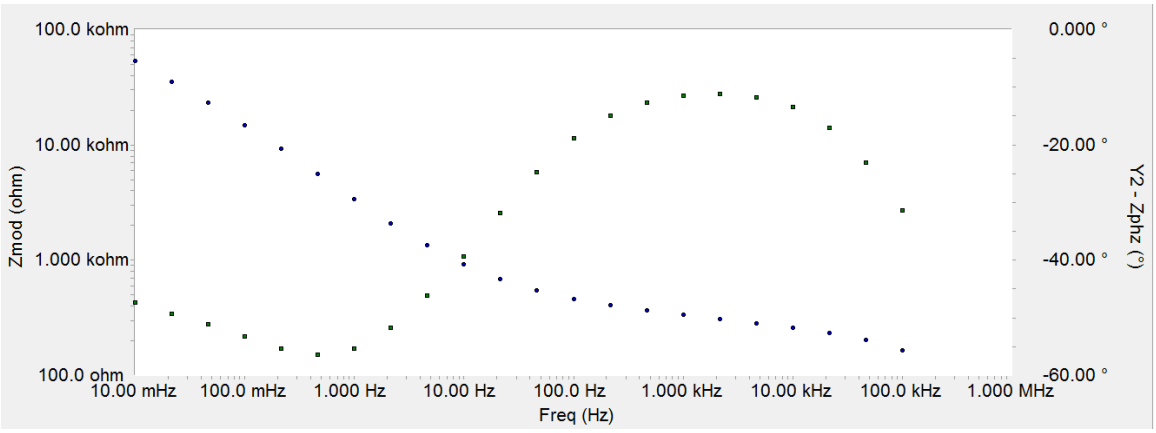

Test g (3.06 days)

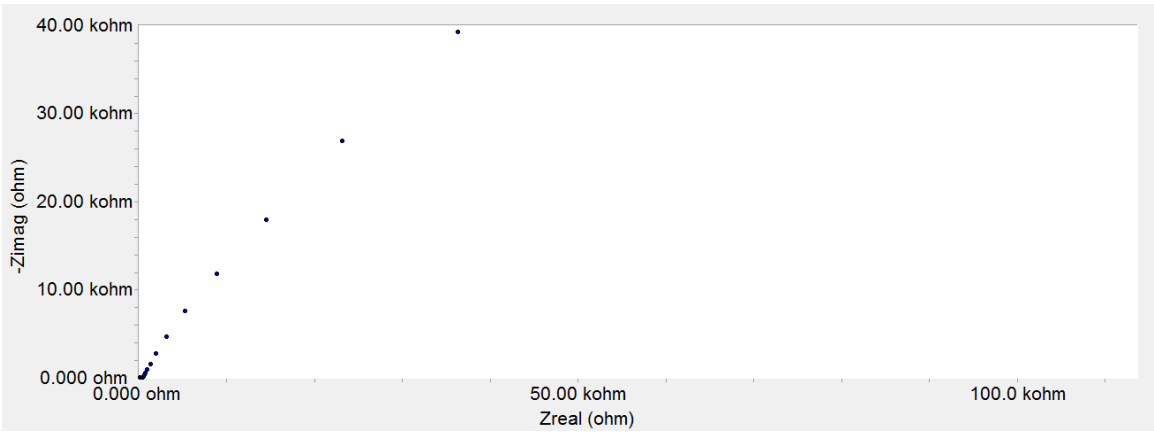

Test g (3.06 days)

Figure 54: Bode and Nyquist Diagrams for YG21 at 3.06 Days of Exposure.

Appendix 1: (Continued)

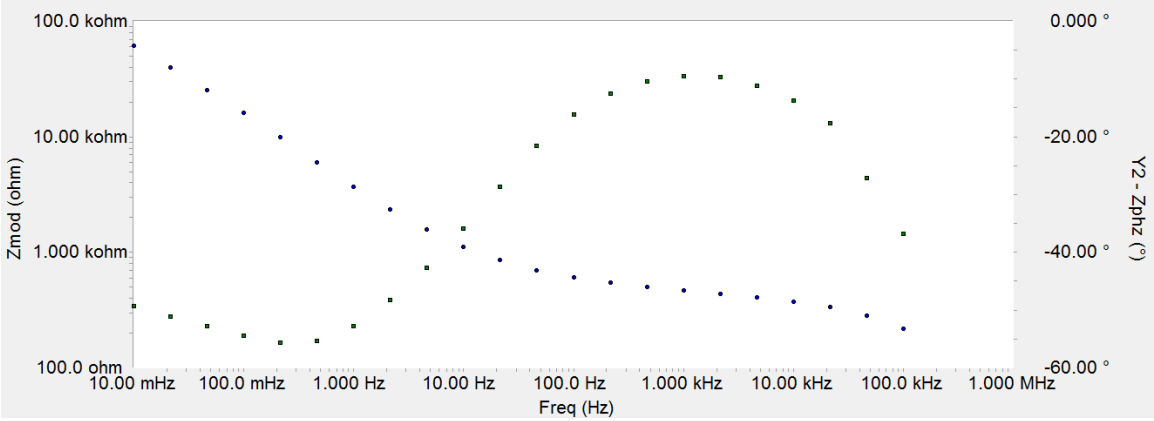

Test h (5.95 days)

Test h (5.95 days)

Figure 55: Bode and Nyquist Diagrams for YG21 at 5.95 Days of Exposure.

Appendix 1: (Continued)

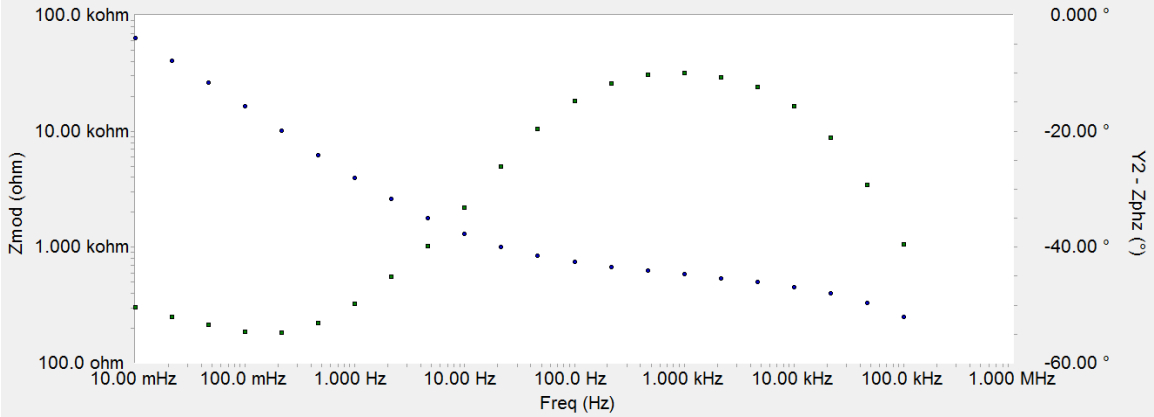

Test i (9.92 days)

Test i (9.92 days)

Figure 56: Bode and Nyquist Diagrams for YG21 at 9.92 Days of Exposure.

Appendix 1: (Continued)

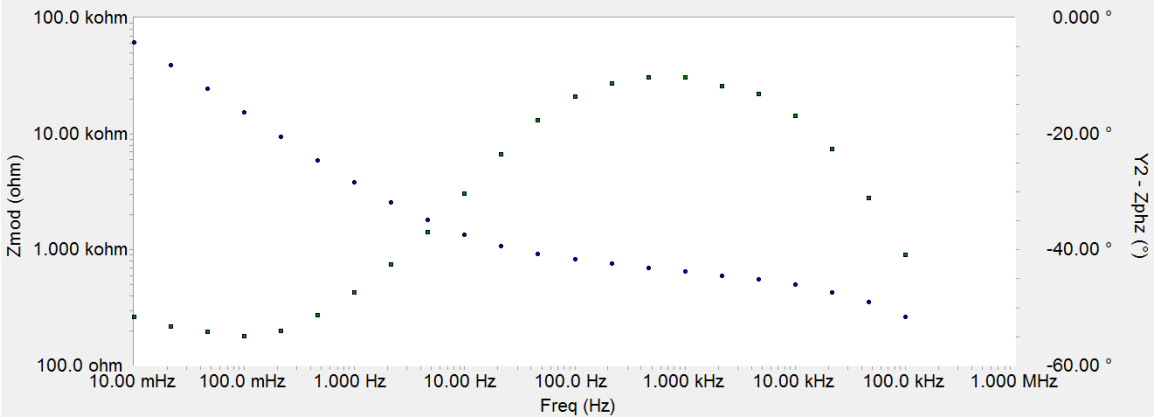

Test j (12.99 days)

Test j (12.99 days)

Figure 57: Bode and Nyquist Diagrams for YG21 at 12.99 Days of Exposure.

Appendix 1: (Continued)

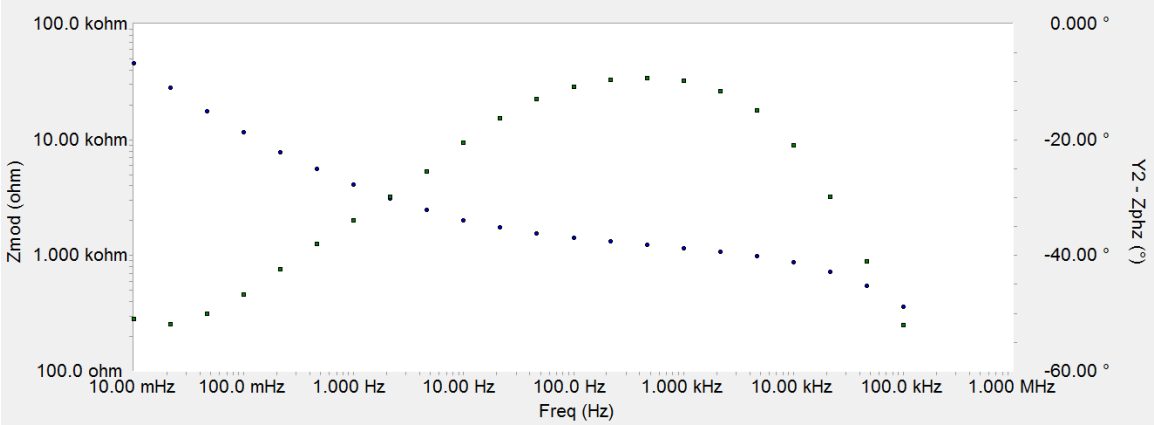

Test k (41.99 days)

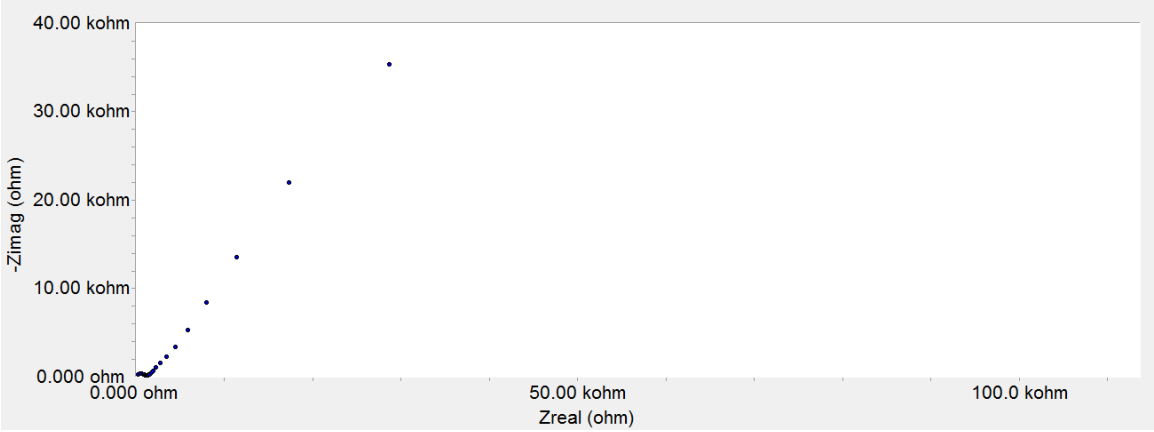

Test k (41.99 days)

Figure 58: Bode and Nyquist Diagrams for YG21 at 41.99 Days of Exposure.

Appendix 1: (Continued)

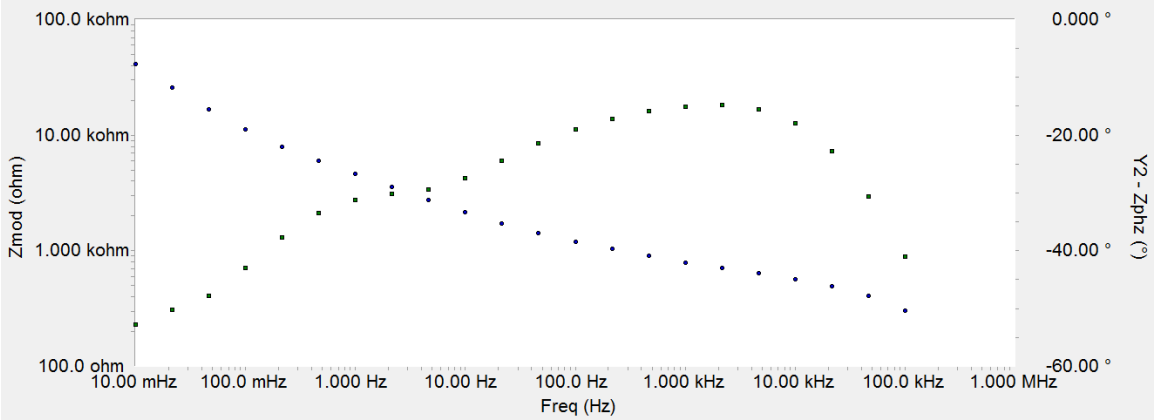

Test l (76.83 days)

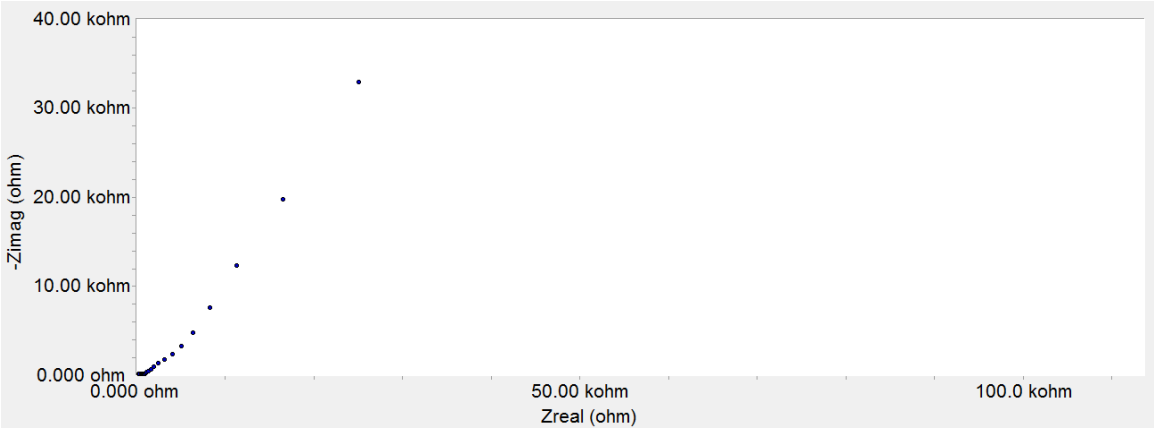

Test l (76.83 days)

Figure 59: Bode and Nyquist Diagrams for YG21 at 76.83 Days of Exposure.

Appendix 1: (Continued)

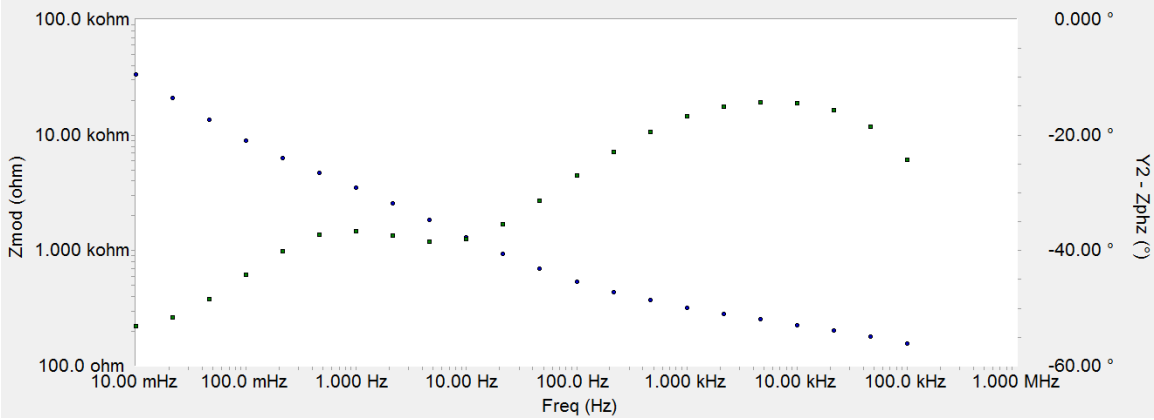

Test m (85.92 days)

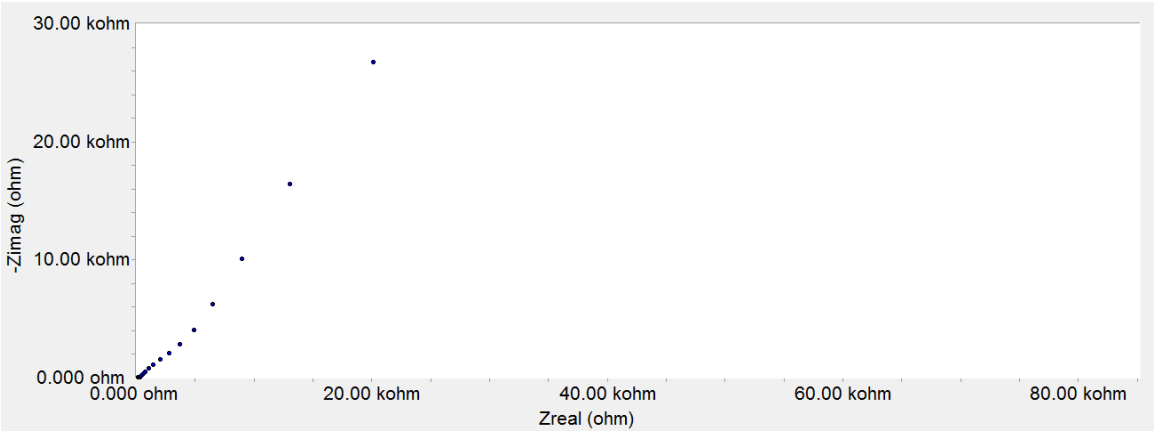

Test m (85.92 days)

Figure 60: Bode and Nyquist Diagrams for YG21 at 85.92 Days of Exposure.

Appendix 1: (Continued)

YB14 (No-chloride) Impedance Diagrams

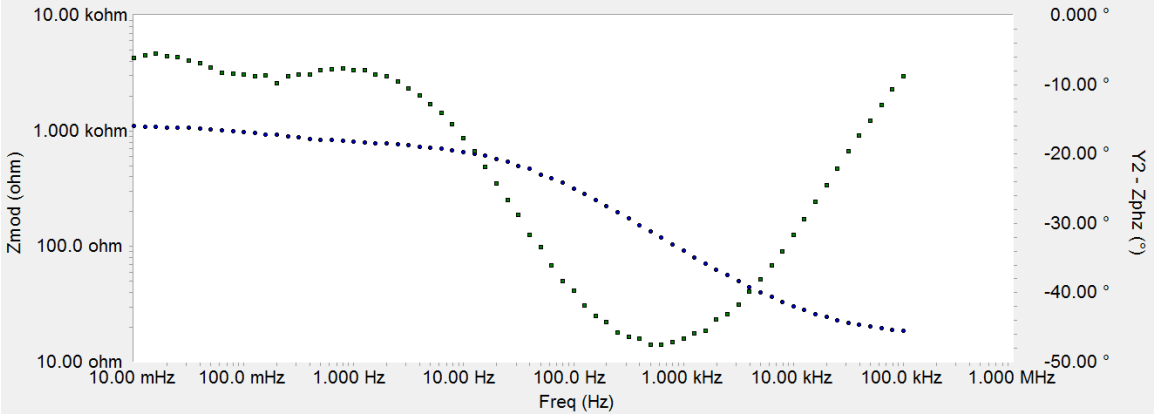

Test a (0.04 days)

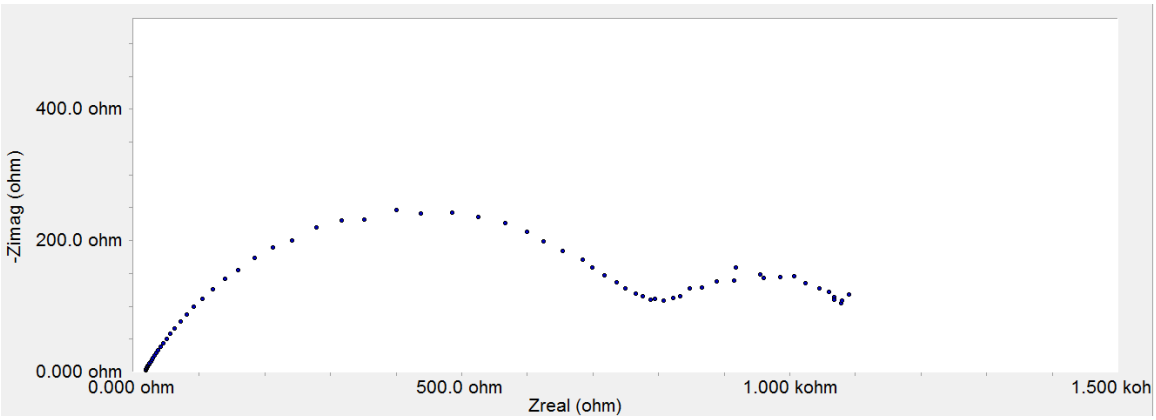

Test a (0.04 days)

Figure 61: Bode and Nyquist Diagrams for YB14 at 0.04 Days of Exposure.

Appendix 1: (Continued)

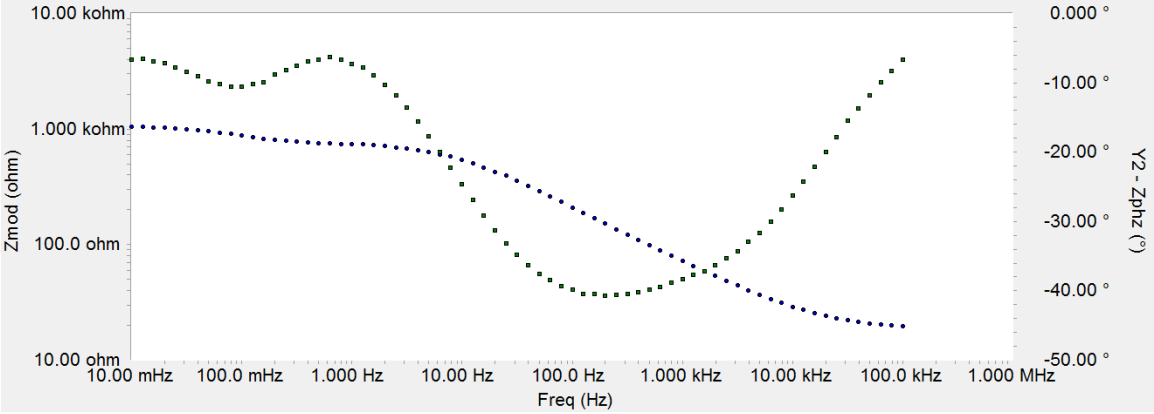

Test b (0.1 days)

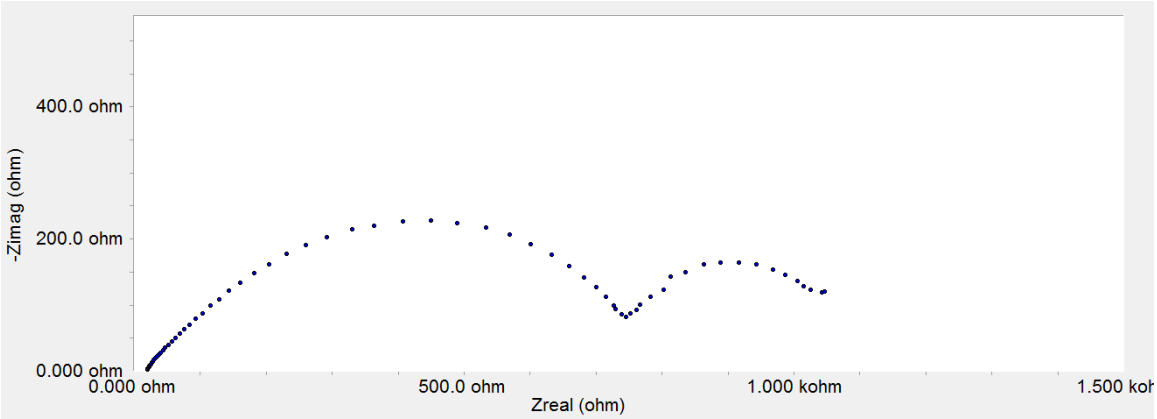

Test b (0.1 days)

Figure 62: Bode and Nyquist Diagrams for YB14 at 0.1 Days of Exposure.

Appendix 1: (Continued)

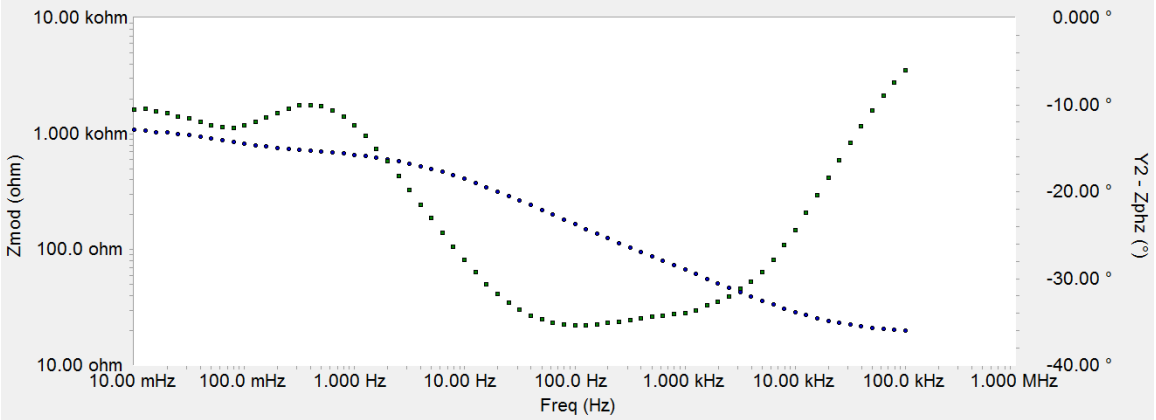

Test c (0.17 days)

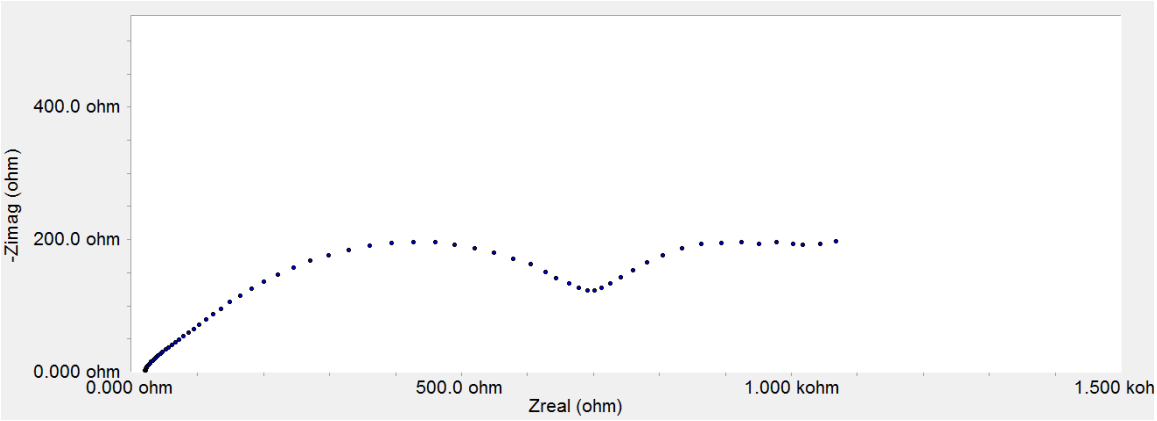

Test c (0.17 days)

Figure 63: Bode and Nyquist Diagrams for YB14 at 0.17 Days of Exposure.

Appendix 1: (Continued)

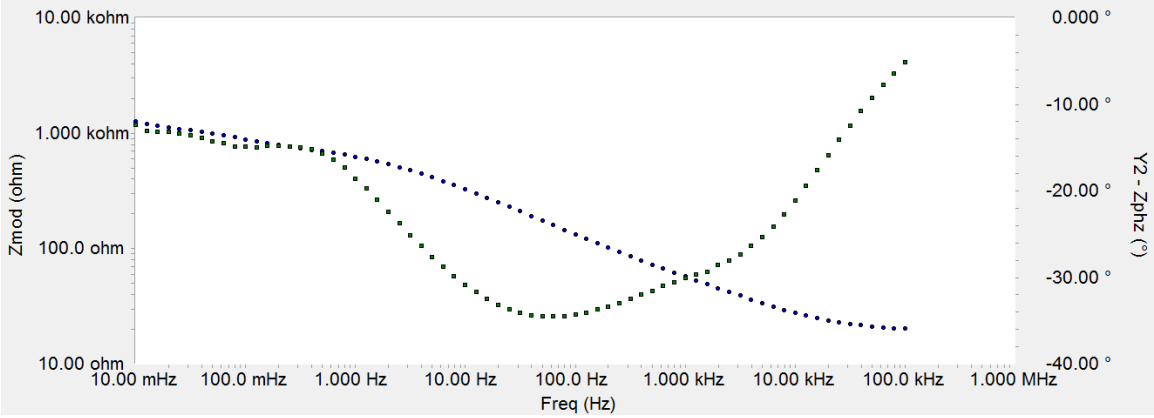

Test d (0.22 days)

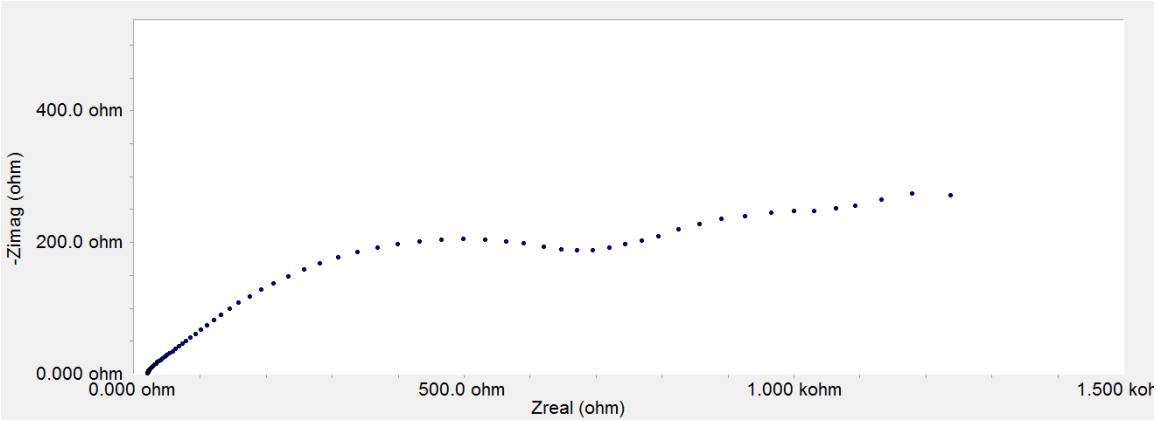

Test d (0.22 days)

Figure 64: Bode and Nyquist Diagrams for YB14 at 0.22 Days of Exposure.

Appendix 1: (Continued)

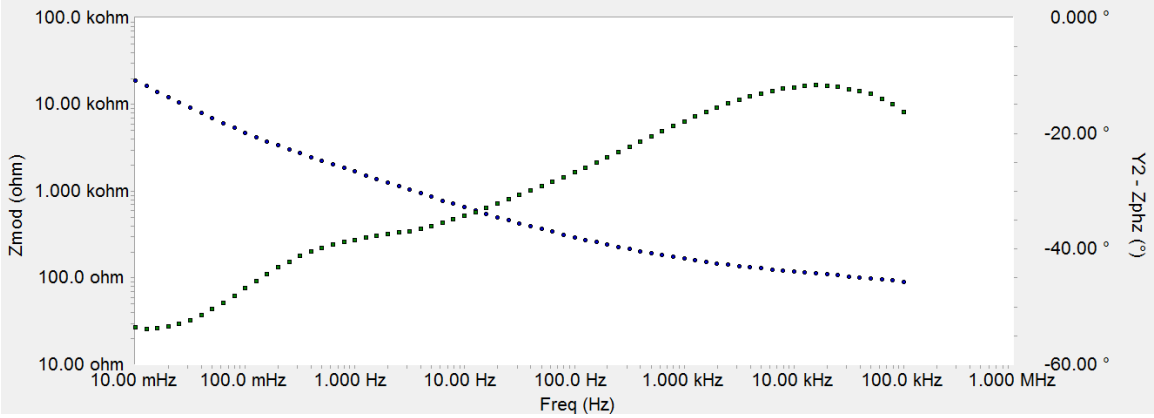

Test e (0.96 days)

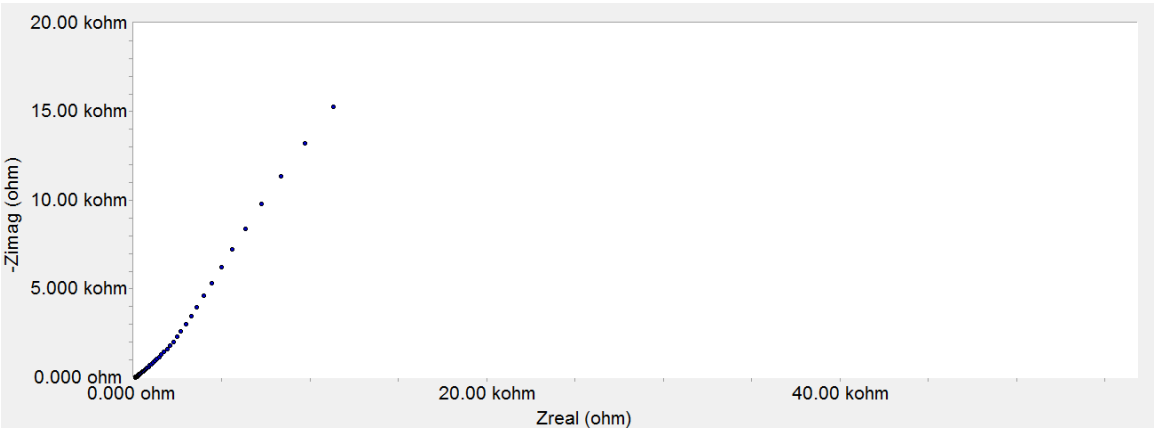

Test e (0.96 days)

Figure 65: Bode and Nyquist Diagrams for YB14 at 0.96 Days of Exposure.

Appendix 1: (Continued)

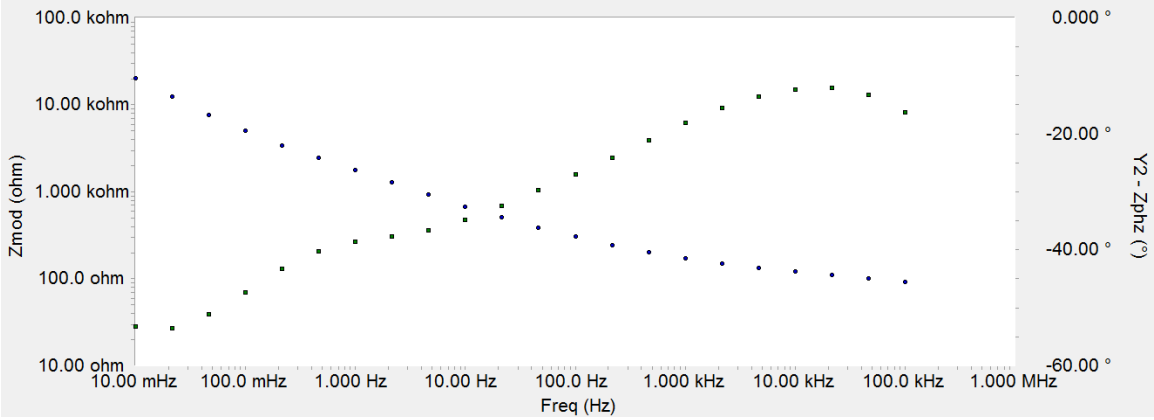

Test f (1.03 days)

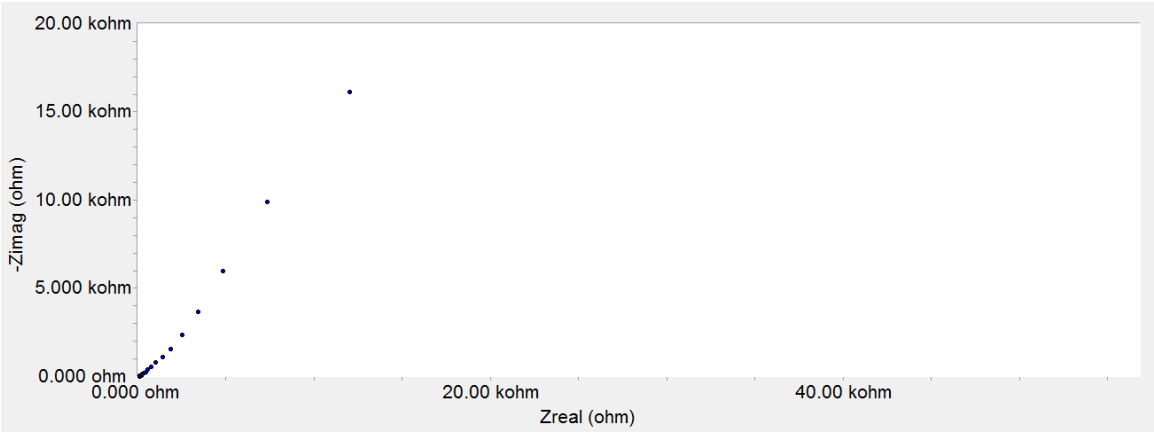

Test f (1.03 days)

Figure 66: Bode and Nyquist Diagrams for YB14 at 1.03 Days of Exposure.

Appendix 1: (Continued)

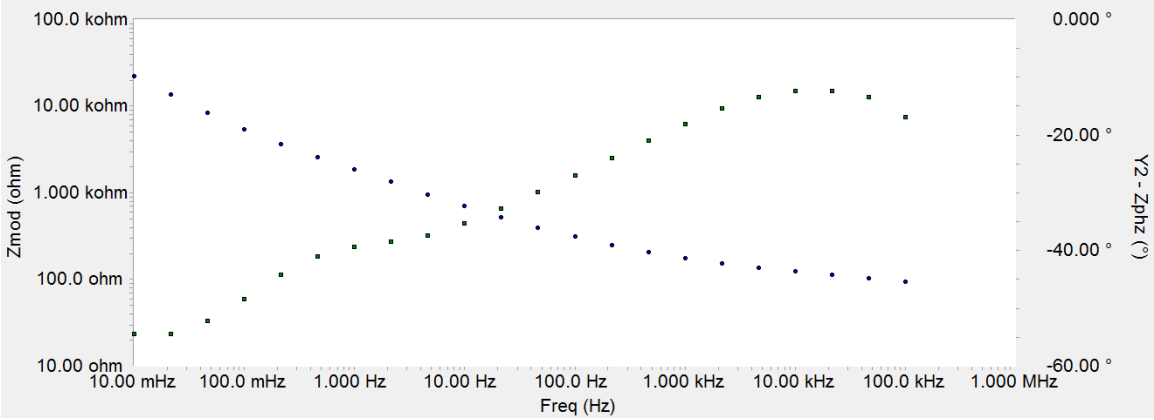

Test g (1.18 days)

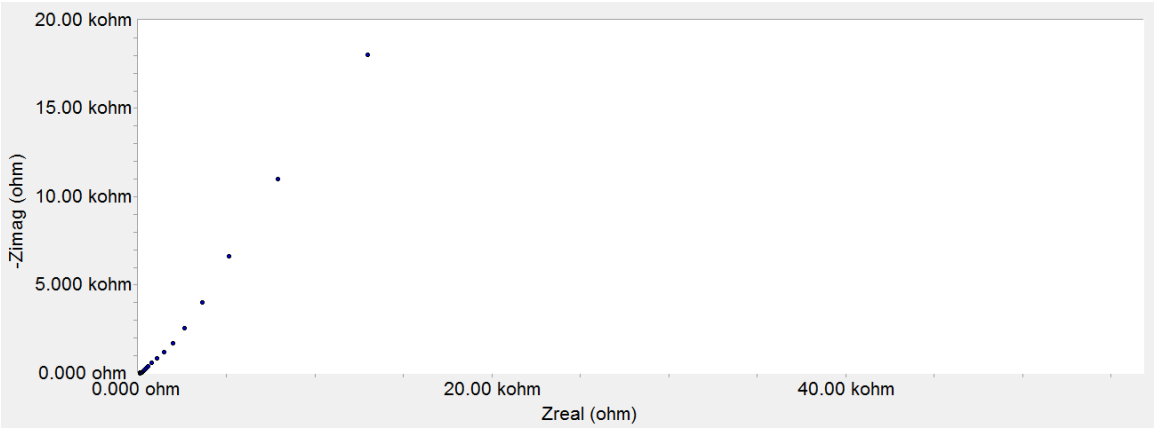

Test g (1.18 days)

Figure 67: Bode and Nyquist Diagrams for YB14 at 1.18 Days of Exposure.

Appendix 1: (Continued)

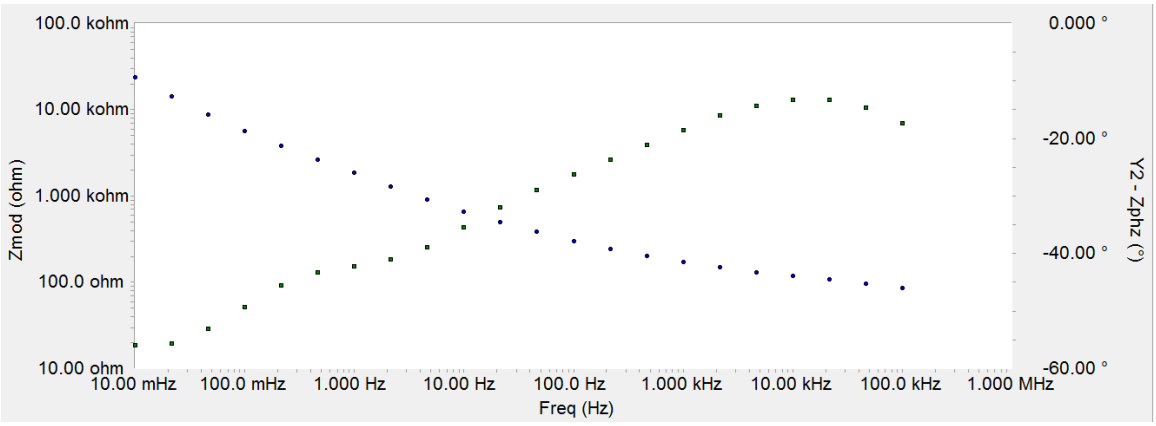

Test h (2 days)

Test h (2 days)

Figure 68: Bode and Nyquist Diagrams for YB14 at 2 Days of Exposure.

Appendix 1: (Continued)

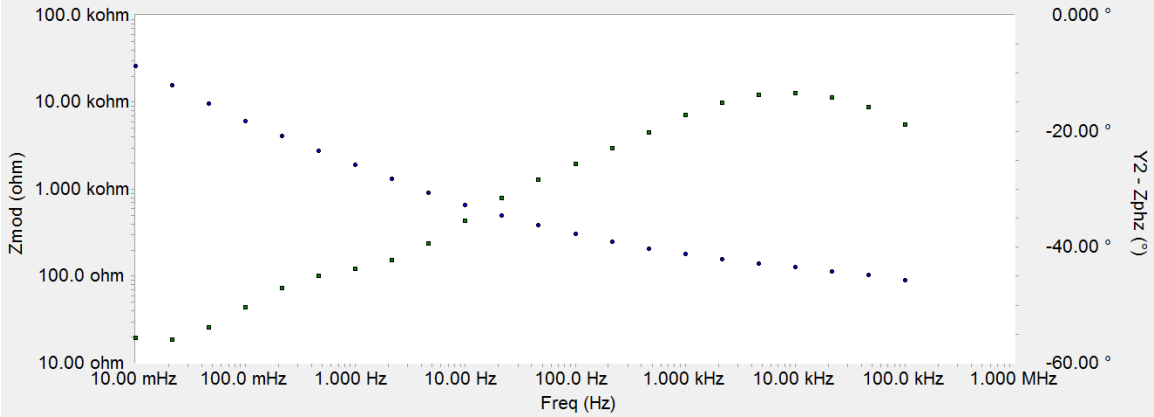

Test i (2.95 days)

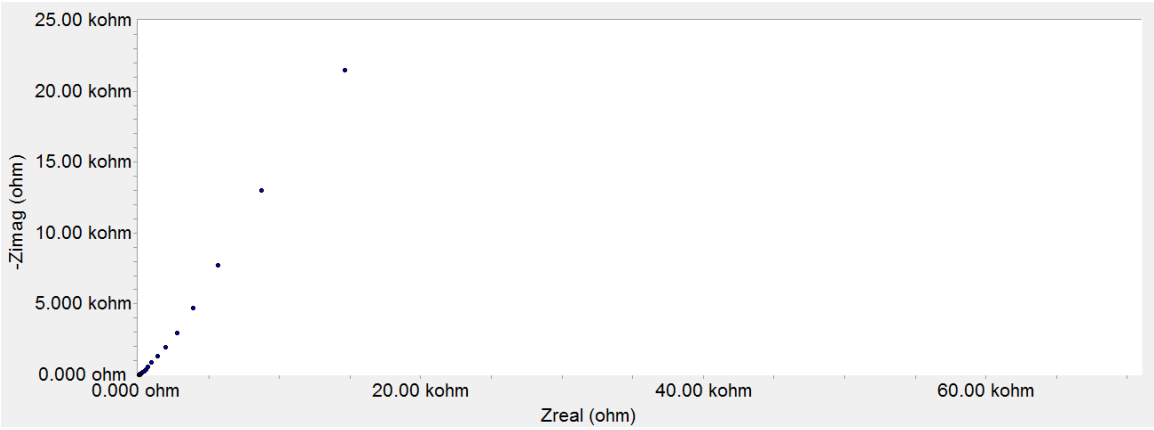

Test i (2.95 days)

Figure 69: Bode and Nyquist Diagrams for YB14 at 2.95 Days of Exposure.

Appendix 1: (Continued)

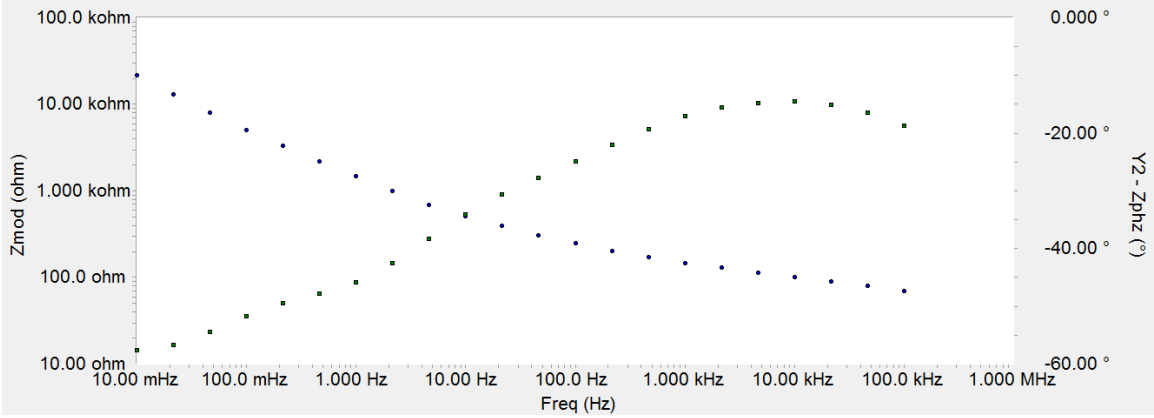

Test j (5.94 days)

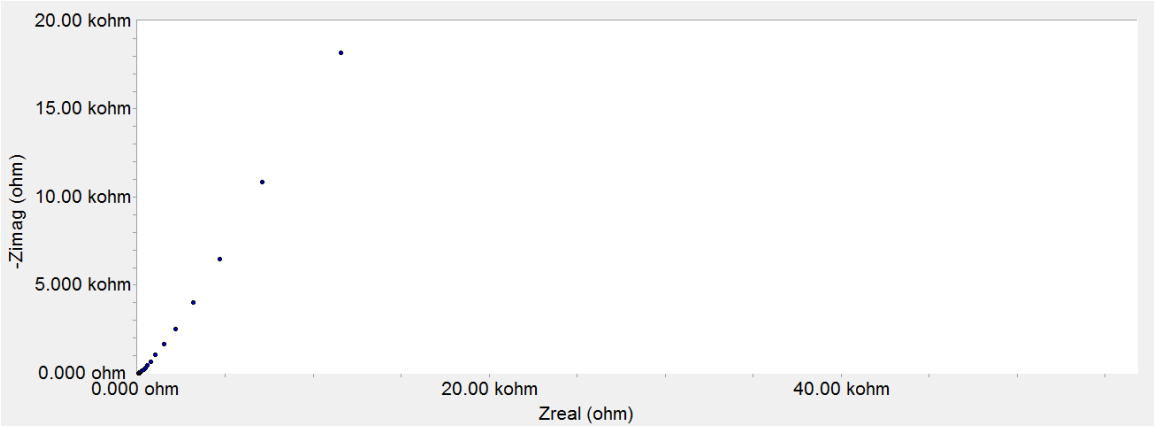

Test j (5.94 days)

Figure 70: Bode and Nyquist Diagrams for YB14 at 5.94 Days of Exposure.

Appendix 1: (Continued)

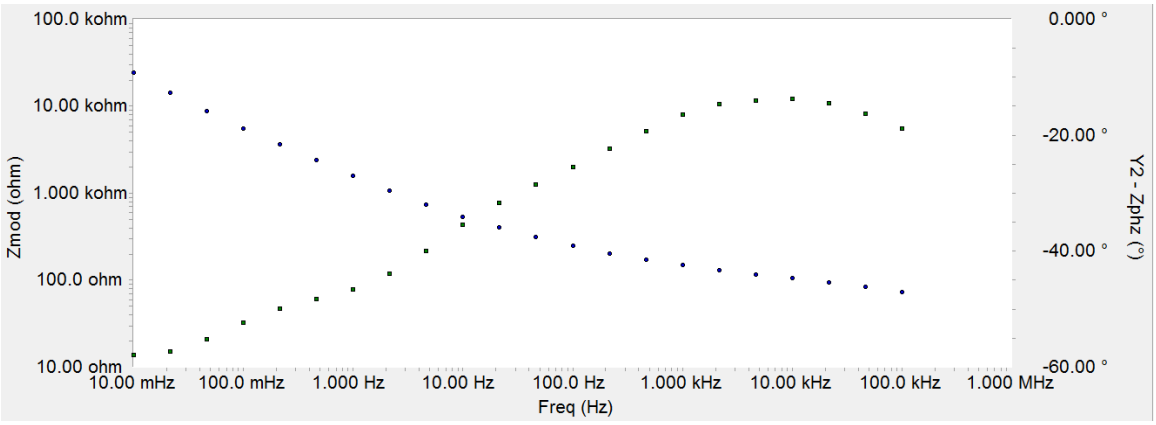

Test k (7 days)

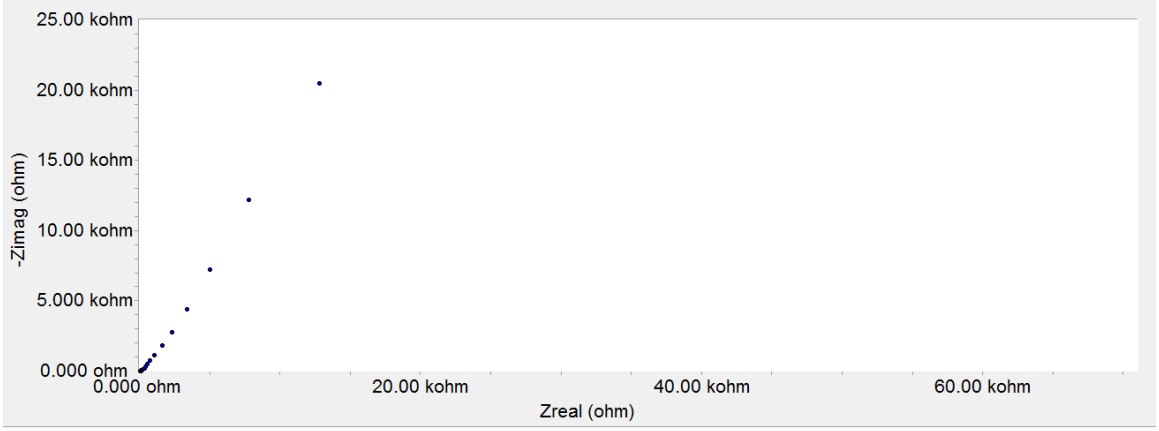

Test k (7 days)

Figure 71: Bode and Nyquist Diagrams for YB14 at 7 Days of Exposure.

Appendix 1: (Continued)

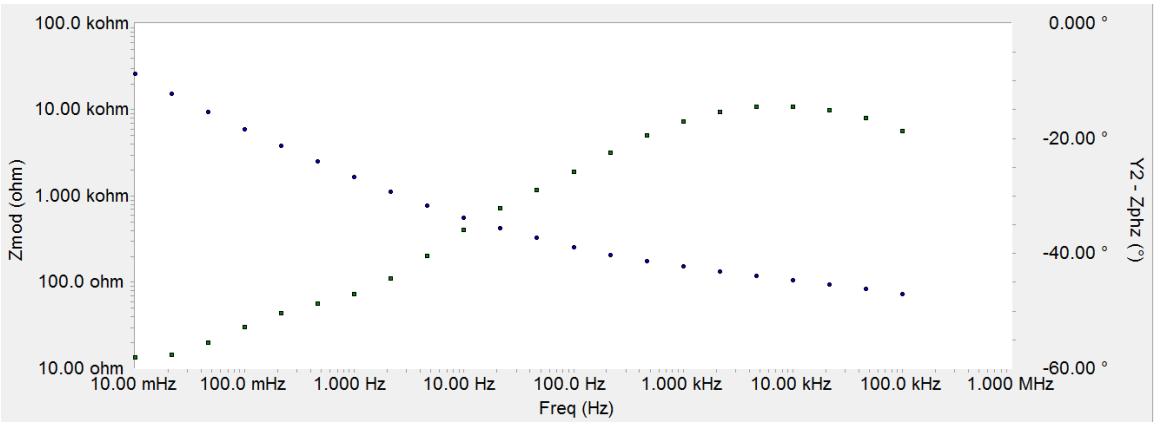

Test l (7.95 days)

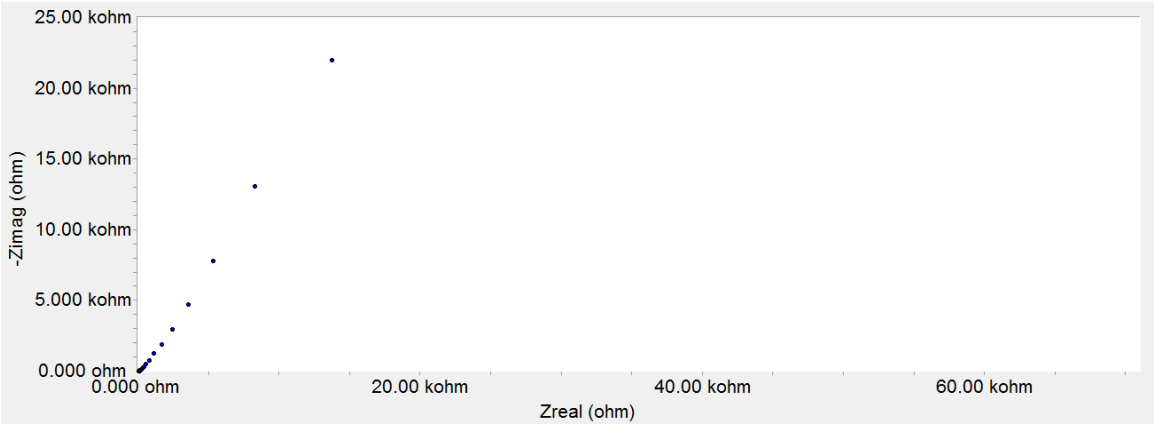

Test l (7.95 days)

Figure 72: Bode and Nyquist Diagrams for YB14 at 7.95 Days of Exposure.

Appendix 1: (Continued)

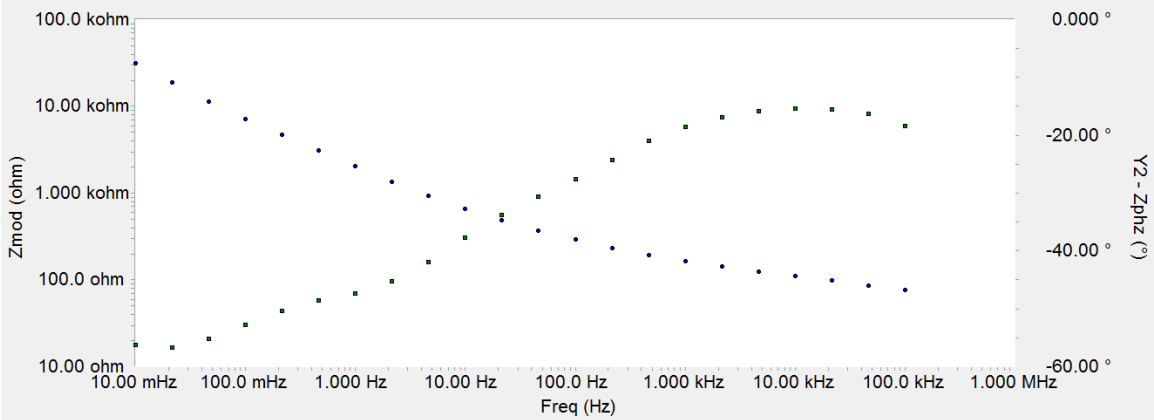

Test m (9.93 days)

Test m (9.93 days)

Figure 73: Bode and Nyquist Diagrams for YB14 at 9.93 Days of Exposure.

Appendix 1: (Continued)

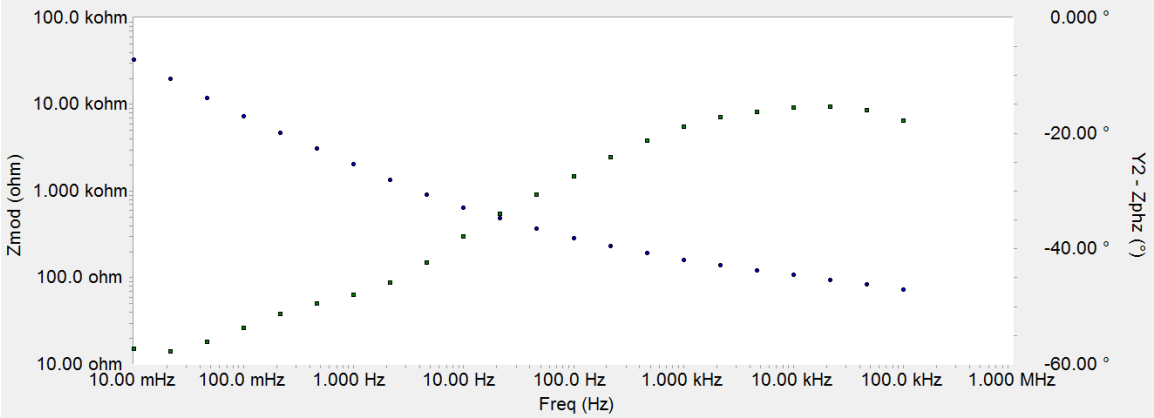

Test n (10.93 days)

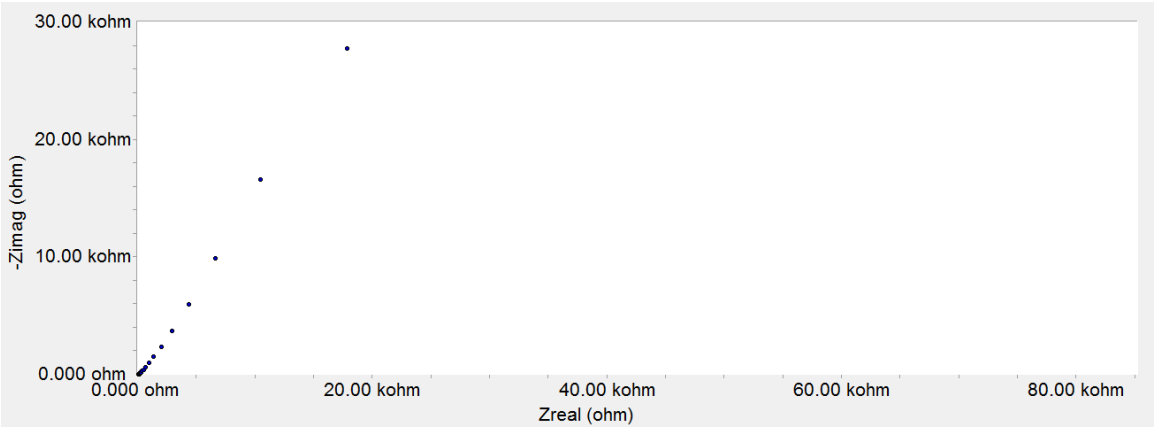

Test n (10.93 days)

Figure 74: Bode and Nyquist Diagrams for YB14 at 10.93 Days of Exposure.

Appendix 1: (Continued)

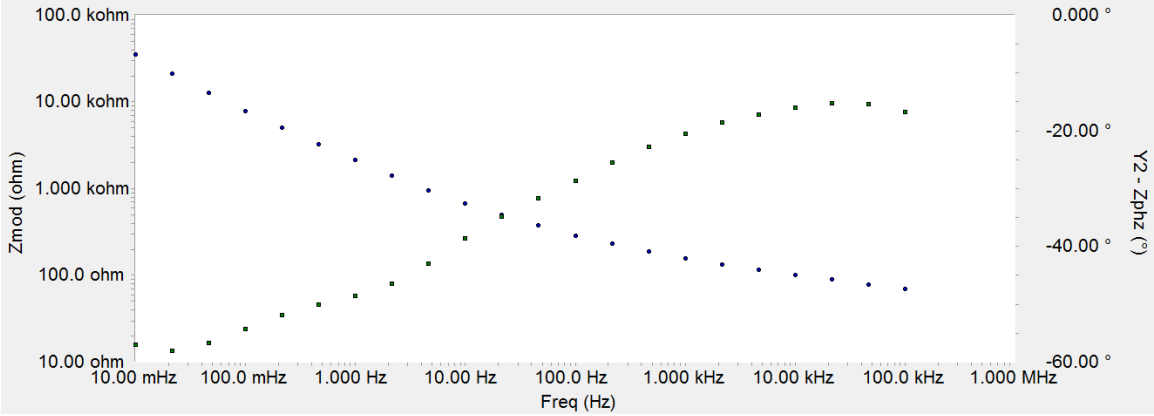

Test o (12.94 days)

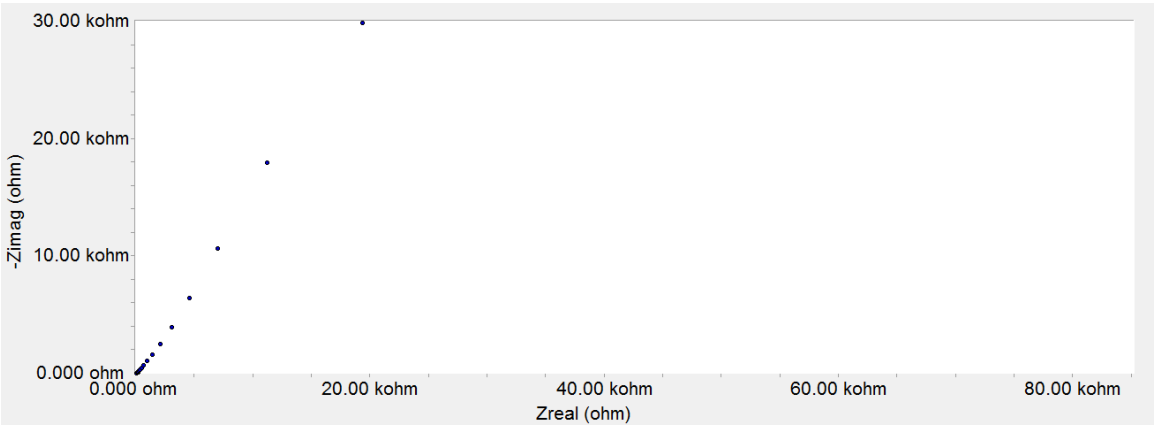

Test o (12.94 days)

Figure 75: Bode and Nyquist Diagrams for YB14 at 12.94 Days of Exposure.

Appendix 1: (Continued)

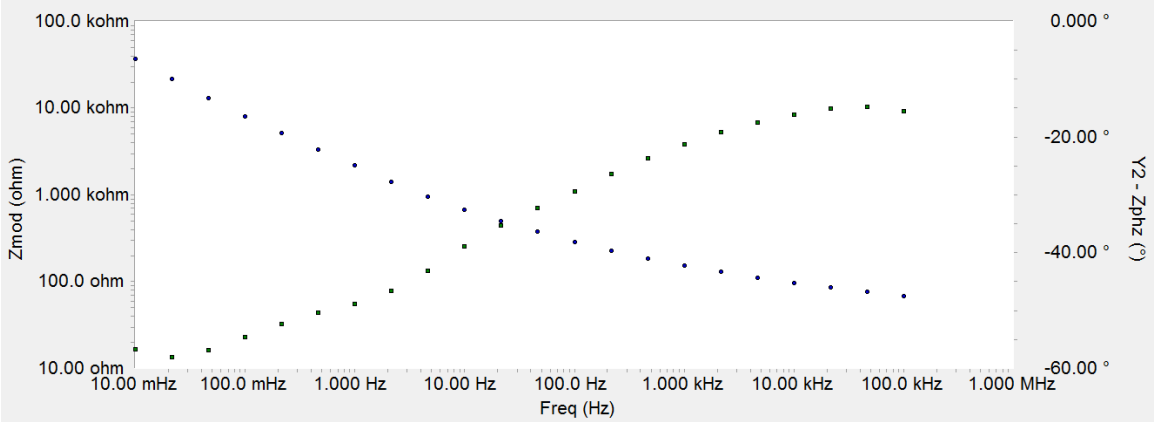

Test p (14.01 days)

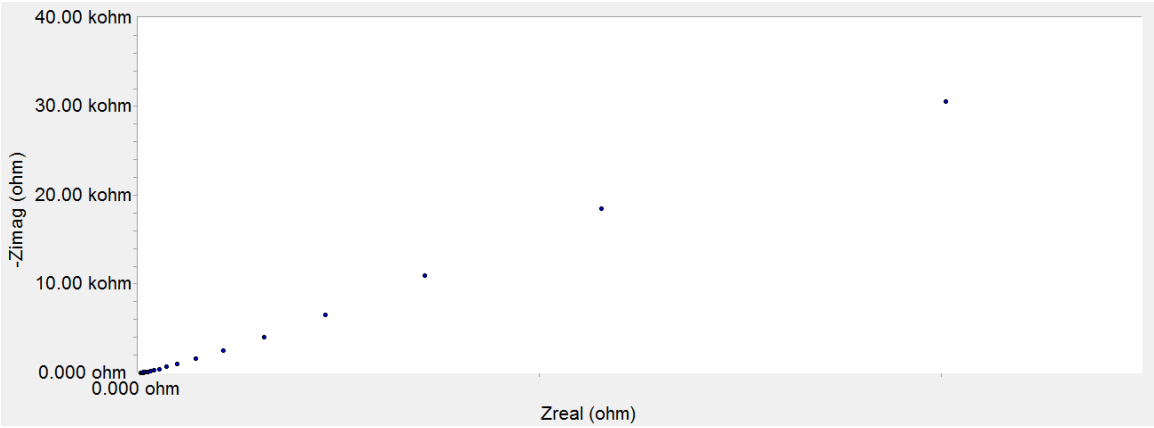

Test p (14.01 days)

Figure 76: Bode and Nyquist Diagrams for YB14 at 14.01 Days of Exposure.

Appendix 1: (Continued)

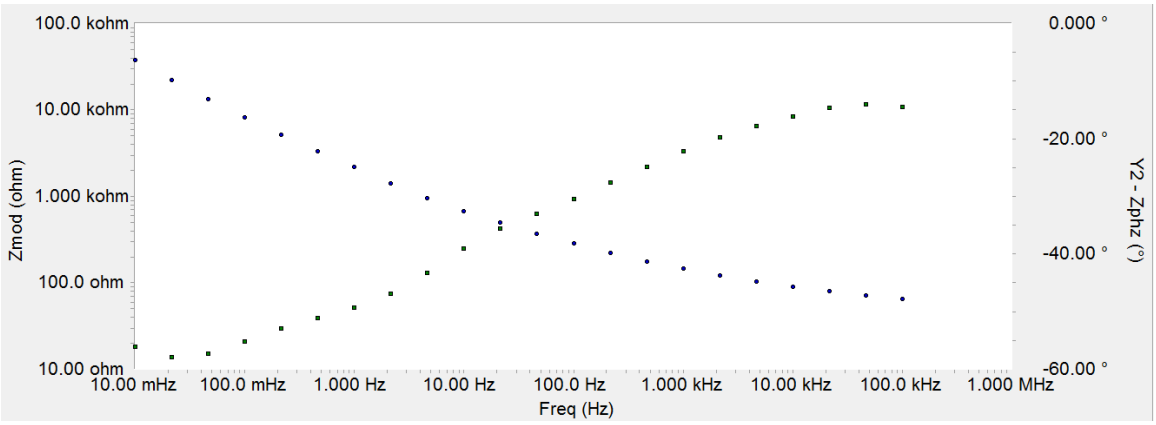

Test q (15.99 days)

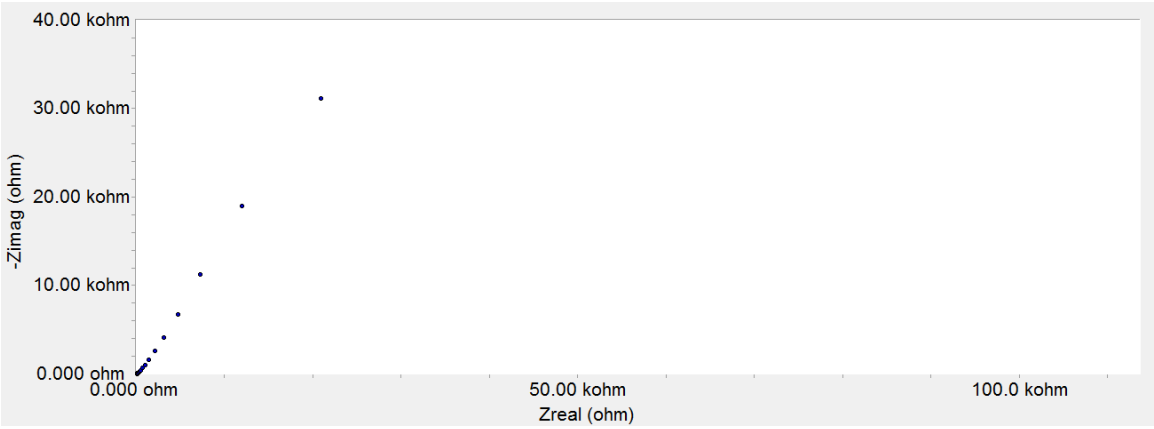

Test q (15.99 days)

Figure 77: Bode and Nyquist Diagrams for YB14 at 15.99 Days of Exposure.

Appendix 1: (Continued)

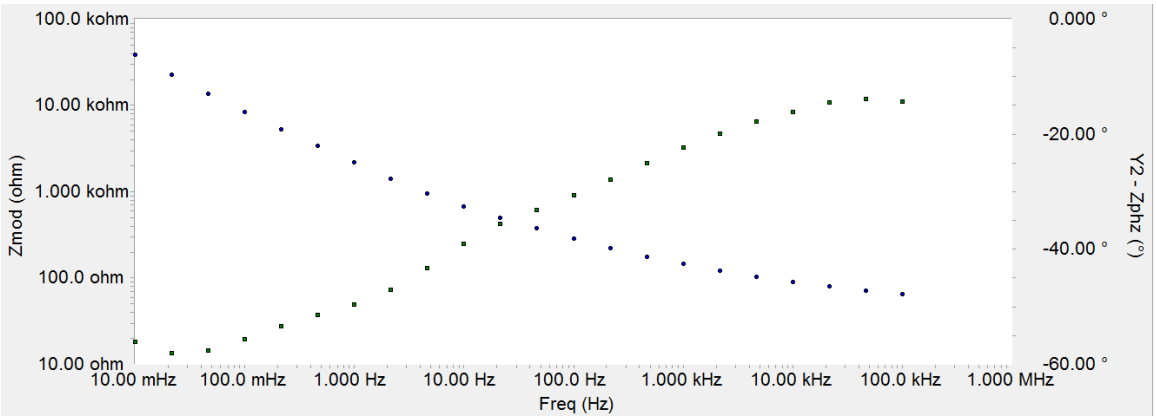

Test r (16.95 days)

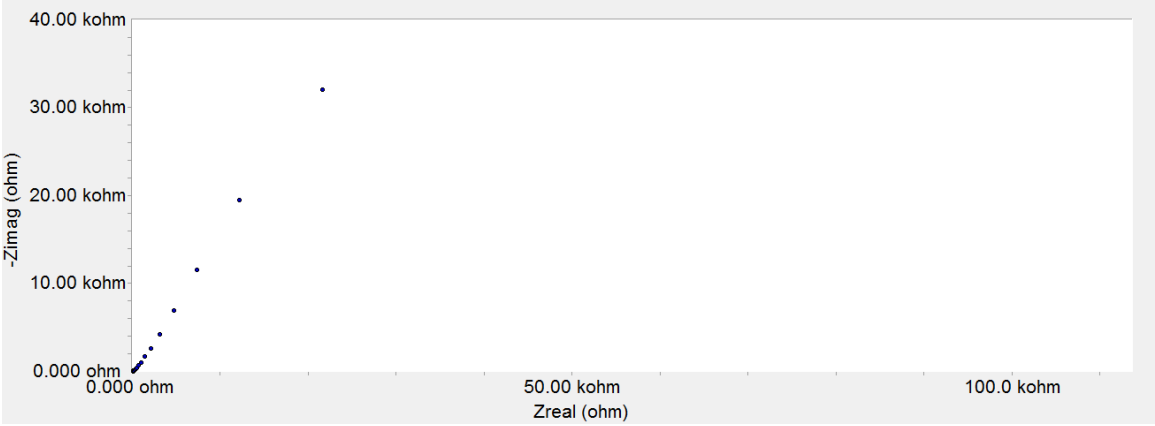

Test r (16.95 days)

Figure 78: Bode and Nyquist Diagrams for YB14 at 16.95 Days of Exposure.

Appendix 1: (Continued)

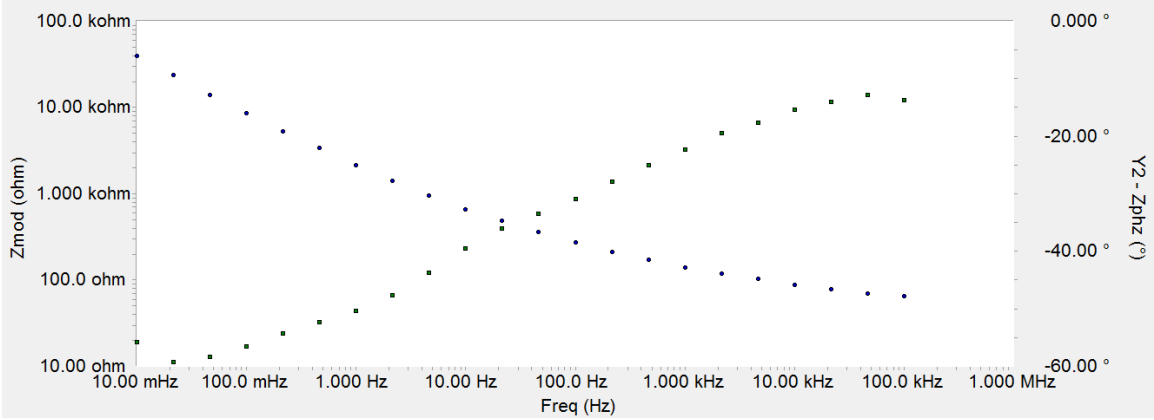

Test s (19.94 days)

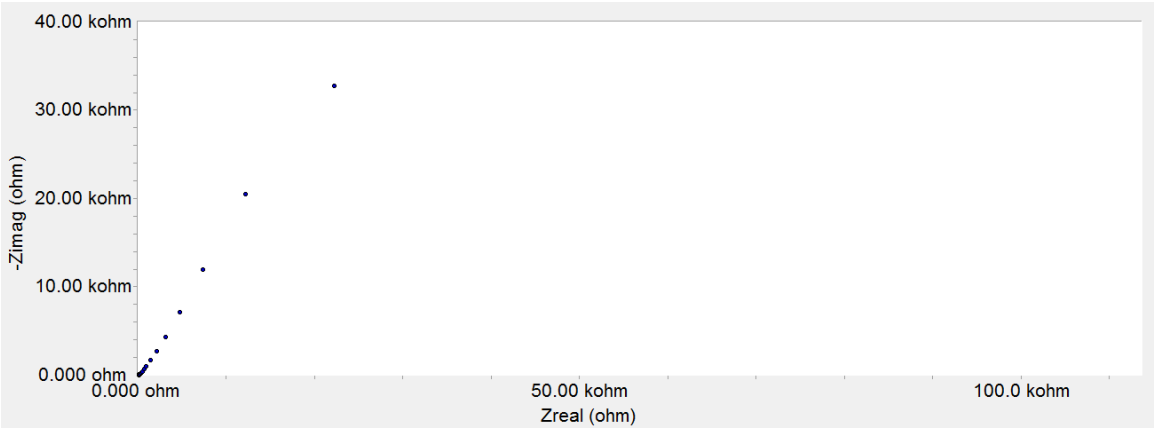

Test s (19.94 days)

Figure 79: Bode and Nyquist Diagrams for YB14 at 19.94 Days of Exposure.

Appendix 1: (Continued)

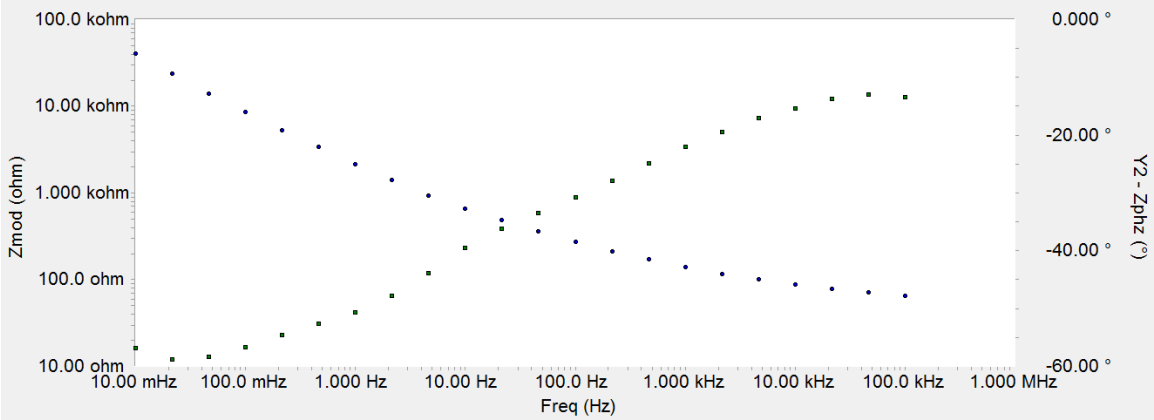

Test t (21.01 days)

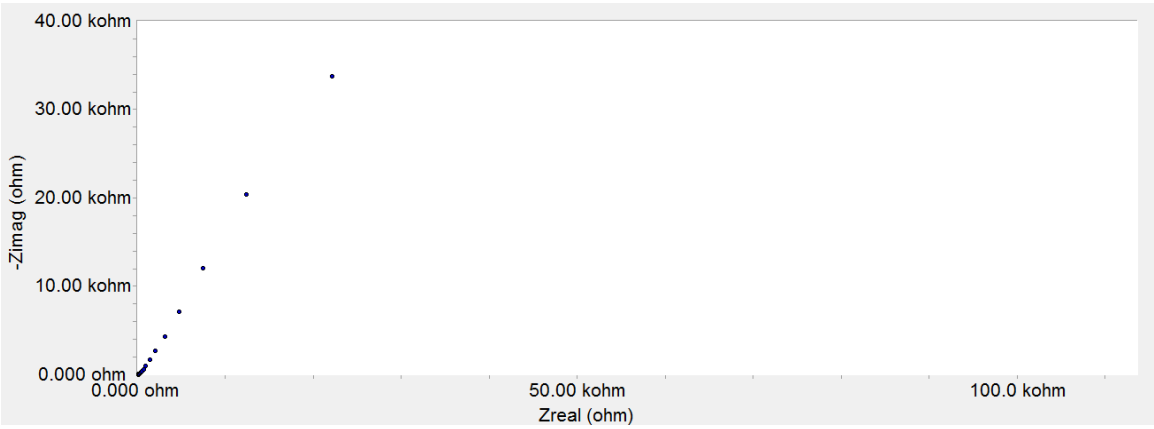

Test t (21.01 days)

Figure 80: Bode and Nyquist Diagrams for YB14 at 21.01 Days of Exposure.

Appendix 1: (Continued)

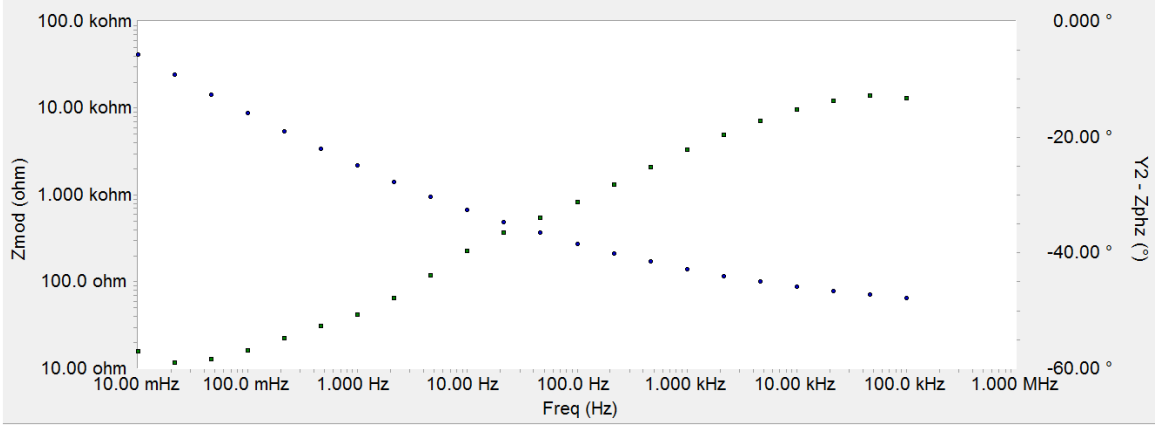

Test u (21.94 days)

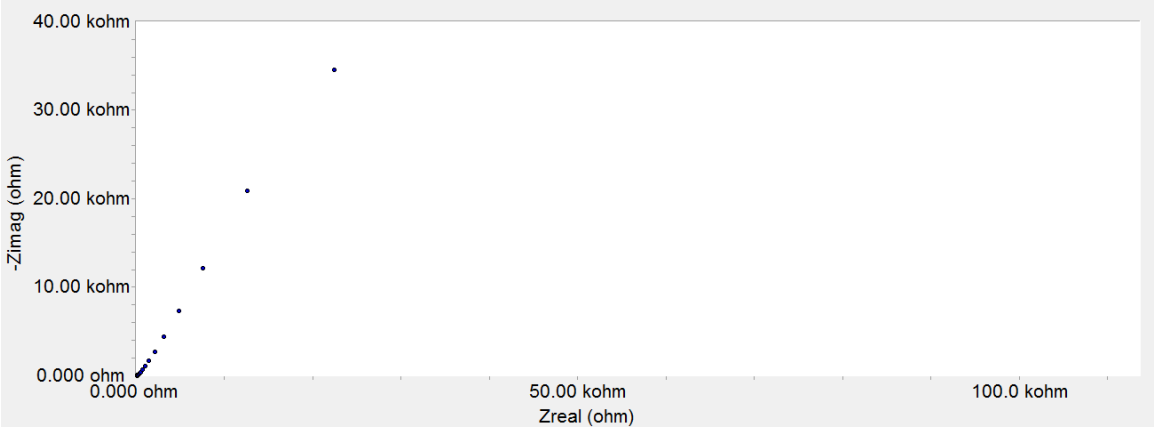

Test u (21.94 days)

Figure 81: Bode and Nyquist Diagrams for YB14 at 21.94 Days of Exposure.

Appendix 1: (Continued)

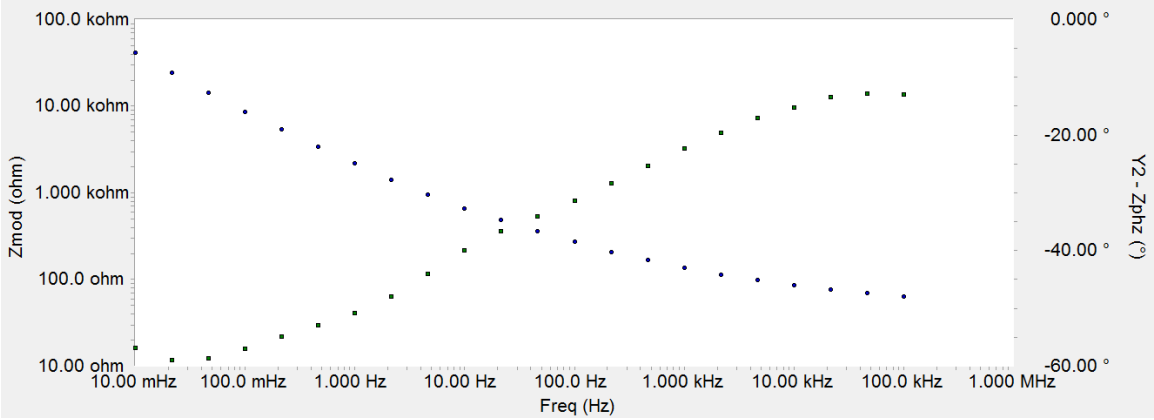

Test v (23.07 days)

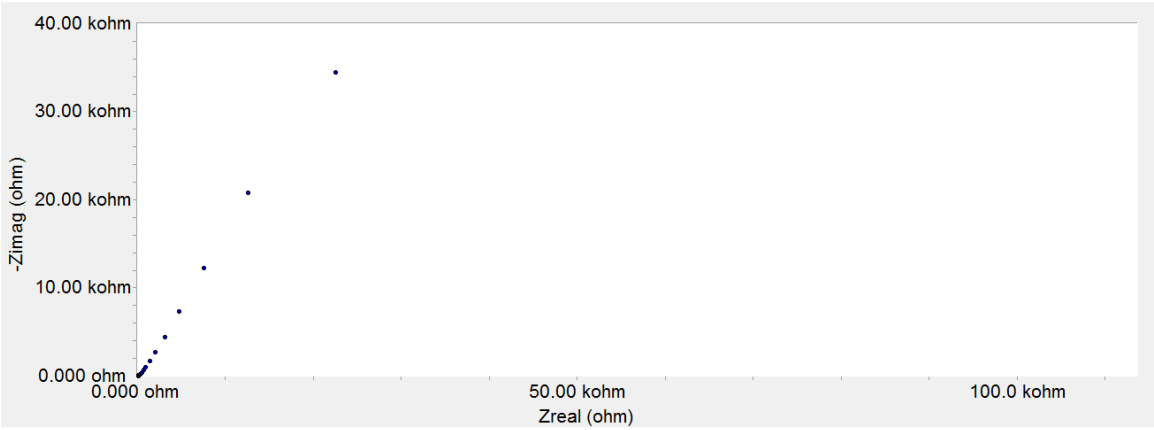

Test v (23.07 days)

Figure 82: Bode and Nyquist Diagrams for YB14 at 23.07 Days of Exposure.

Appendix 1: (Continued)

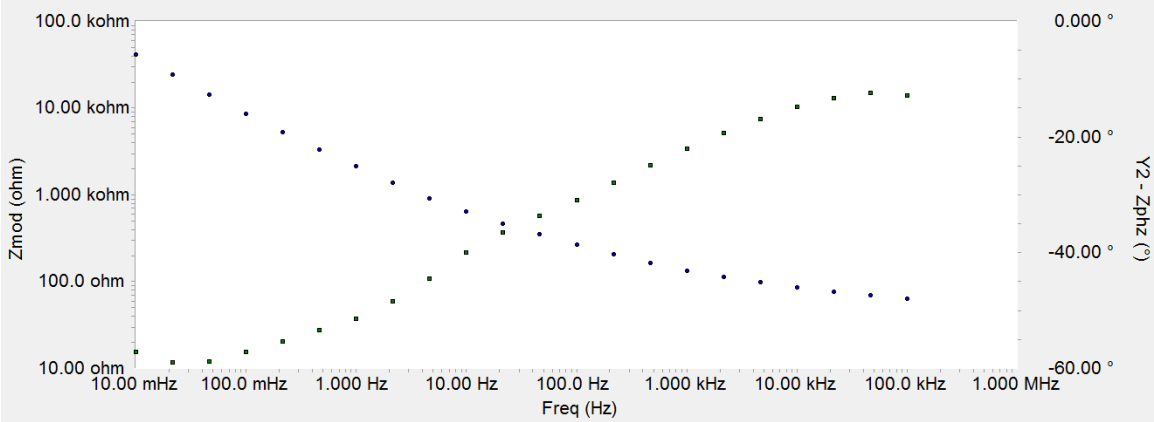

Test w (24.16 days)

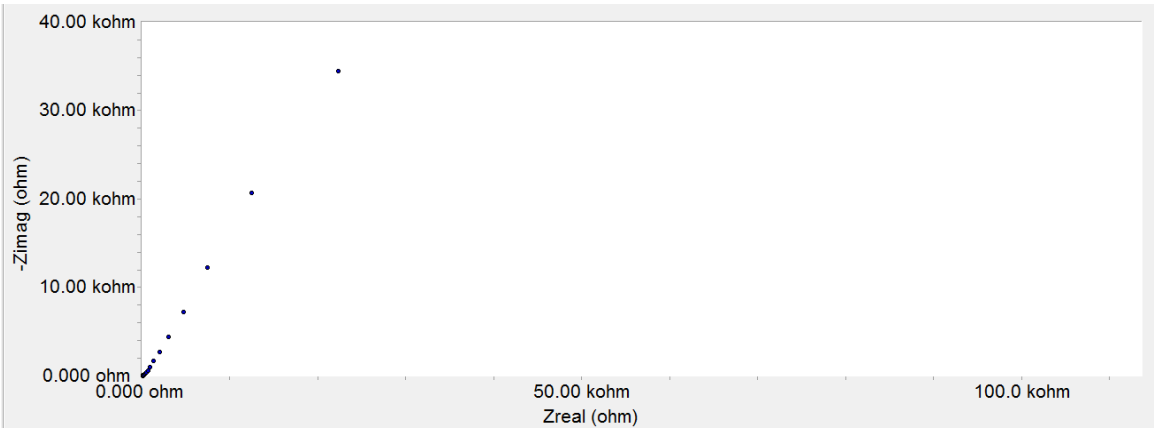

Test w (24.16 days)

Figure 83: Bode and Nyquist Diagrams for YB14 at 24.16 Days of Exposure.

Appendix 1: (Continued)

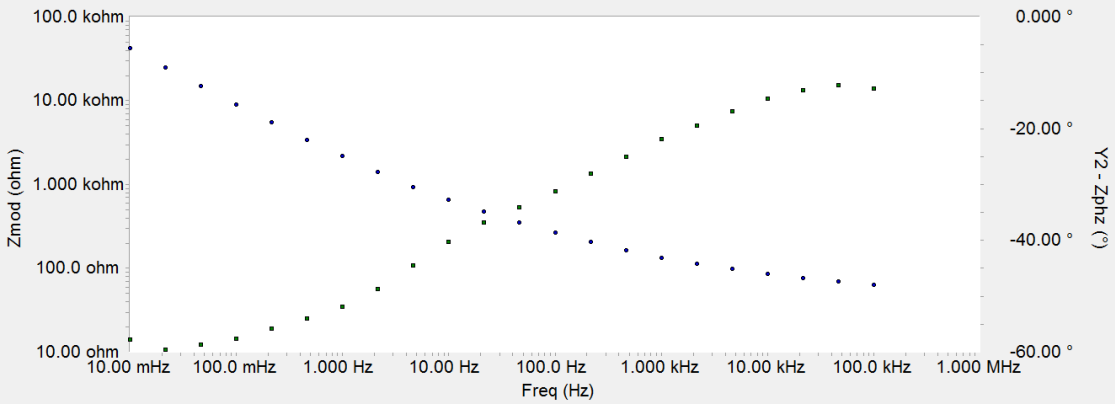

Test x (27.03 days)

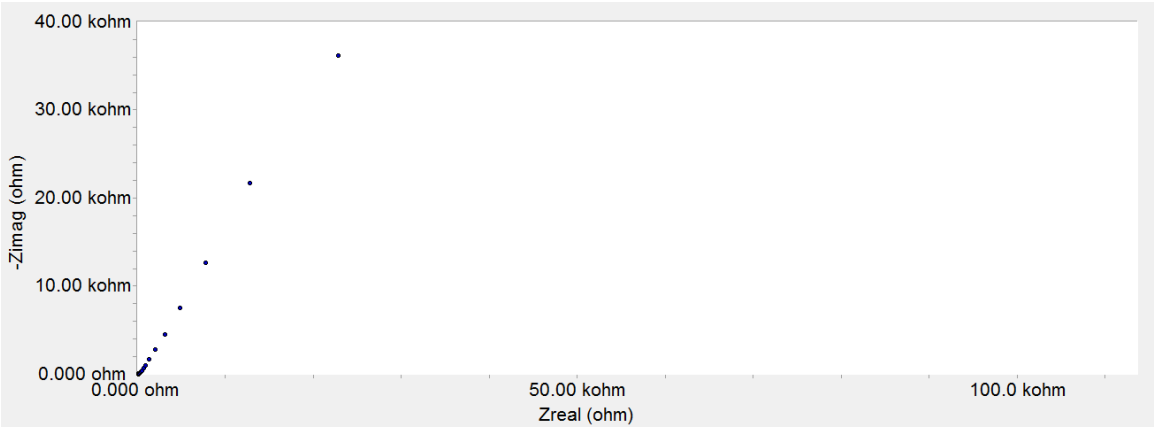

Test x (27.03 days)

Figure 84: Bode and Nyquist Diagrams for YB14 at 27.03 Days of Exposure.

Appendix 1: (Continued)

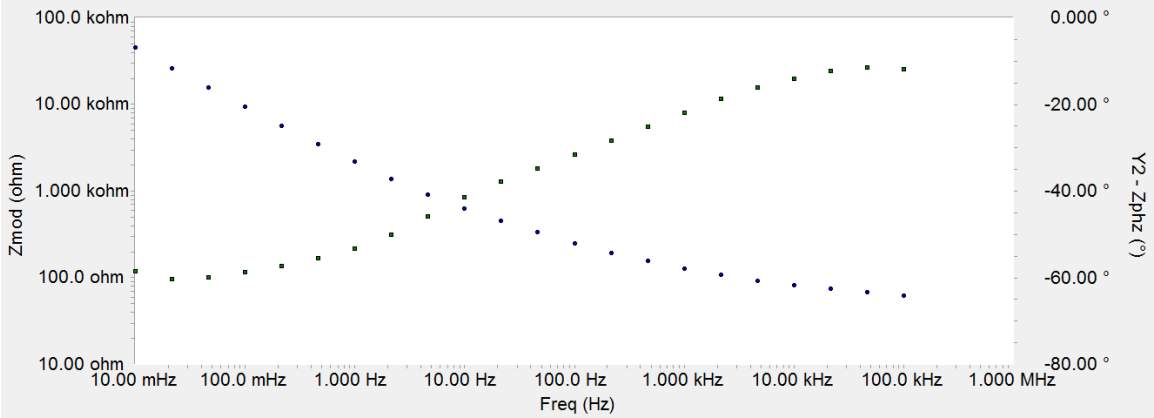

Test y (34.02 days)

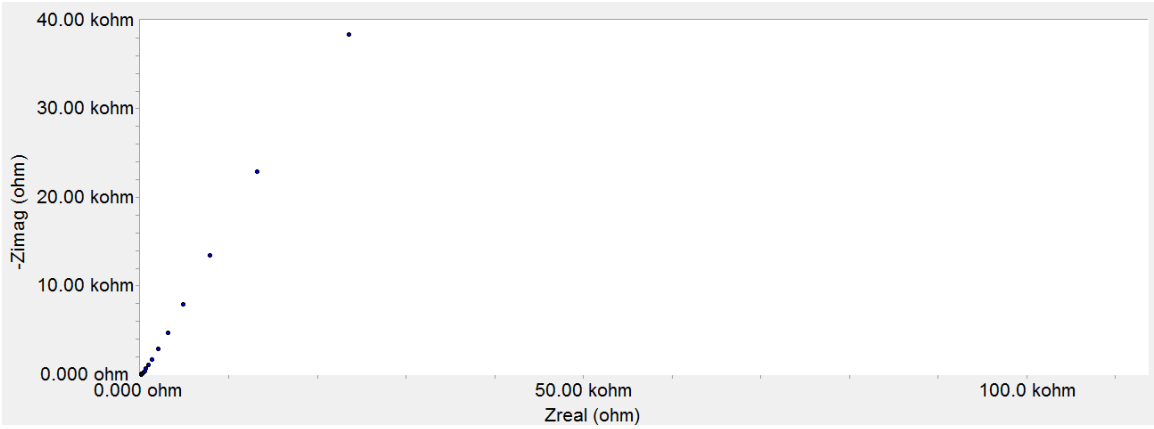

Test y (34.02 days)

Figure 85: Bode and Nyquist Diagrams for YB14 at 34.02 Days of Exposure.

Appendix 1: (Continued)

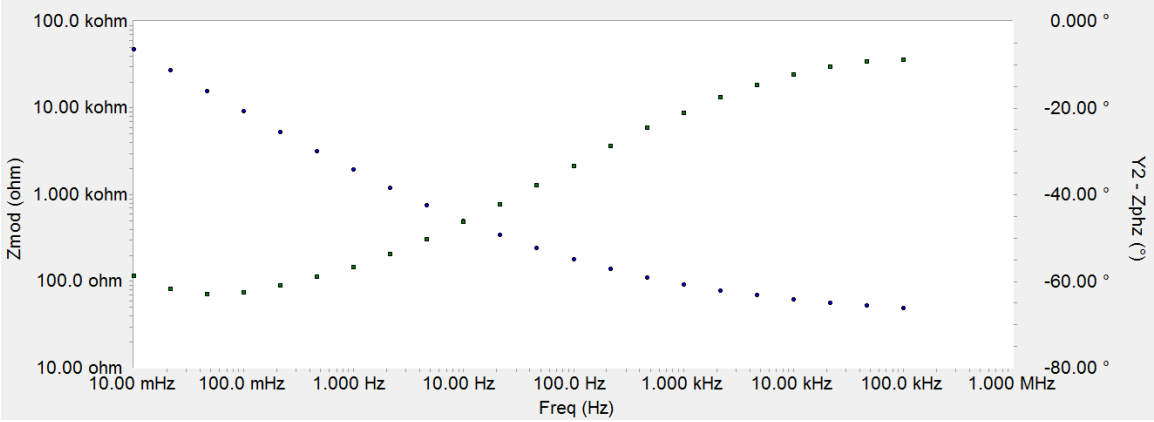

Test z (63.08 days)

Test z (63.08 days)

Figure 86: Bode and Nyquist Diagrams for YB14 at 63.08 Days of Exposure.

Appendix 1: (Continued)

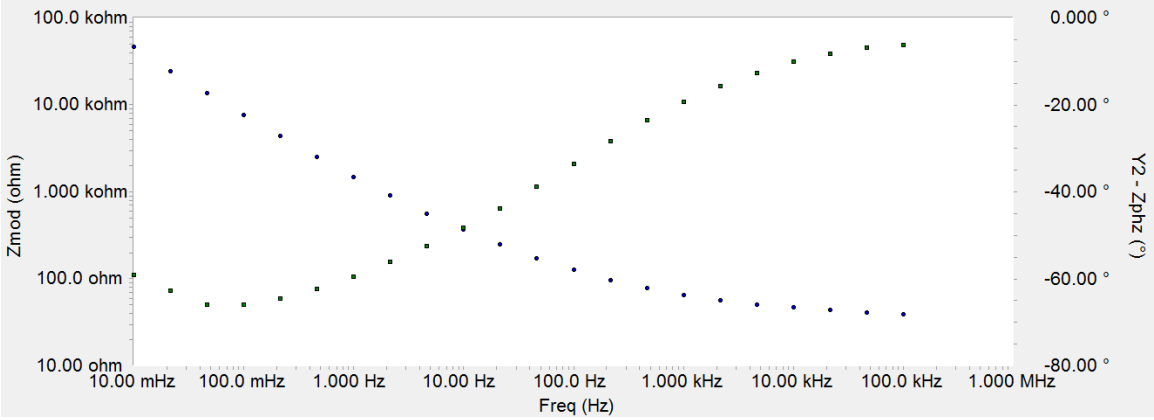

Test aa (97.91 days)

Test aa (97.91 days)

Figure 87: Bode and Nyquist Diagrams for YB14 at 97.91 Days of Exposure.

Appendix 1: (Continued)

YG7 (No-chloride) Impedance Diagrams

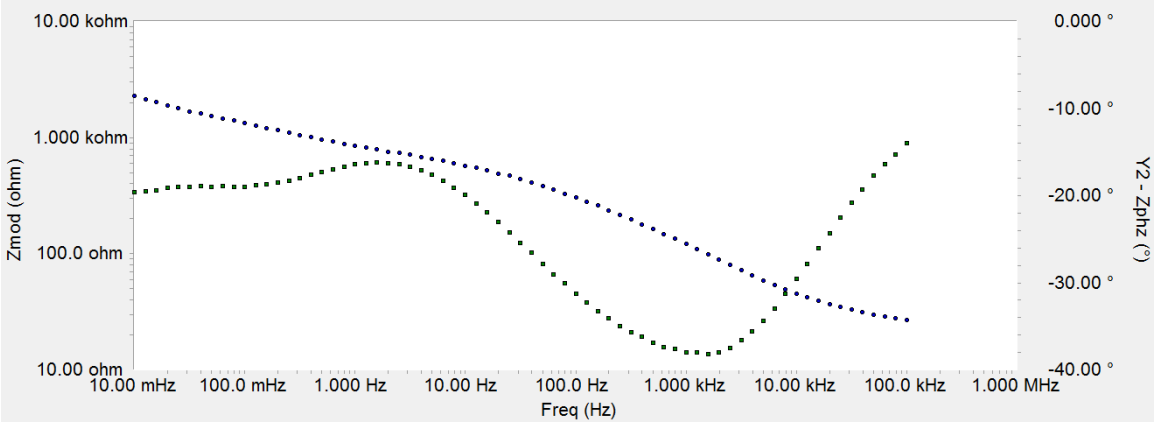

Test a (0.05 days)

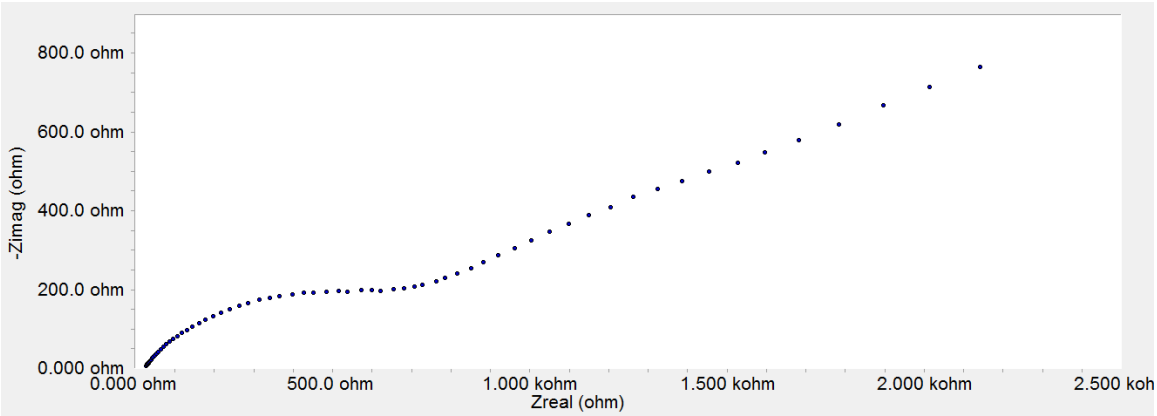

Test a (0.05 days)

Figure 88: Bode and Nyquist Diagrams for YG7 at 0.05 Days of Exposure.

Appendix 1: (Continued)

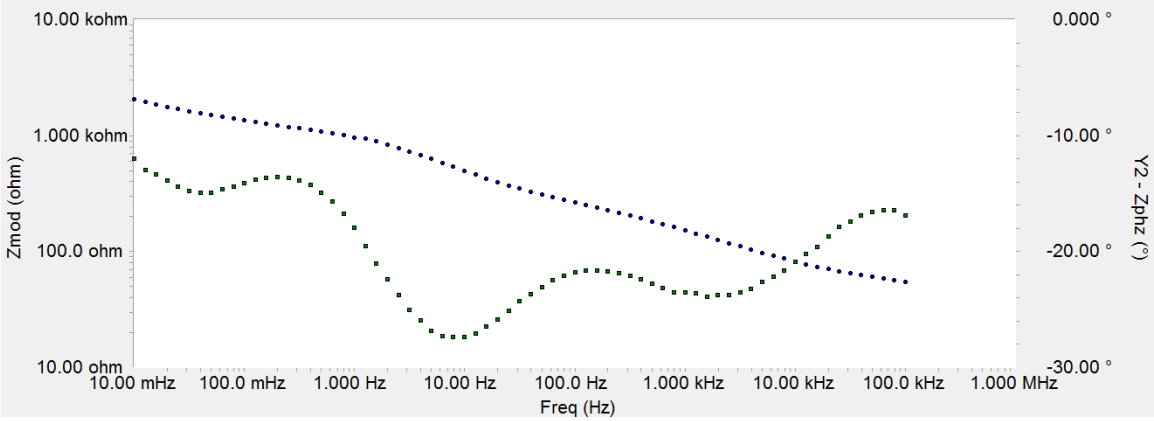

Test b (0.13 days)

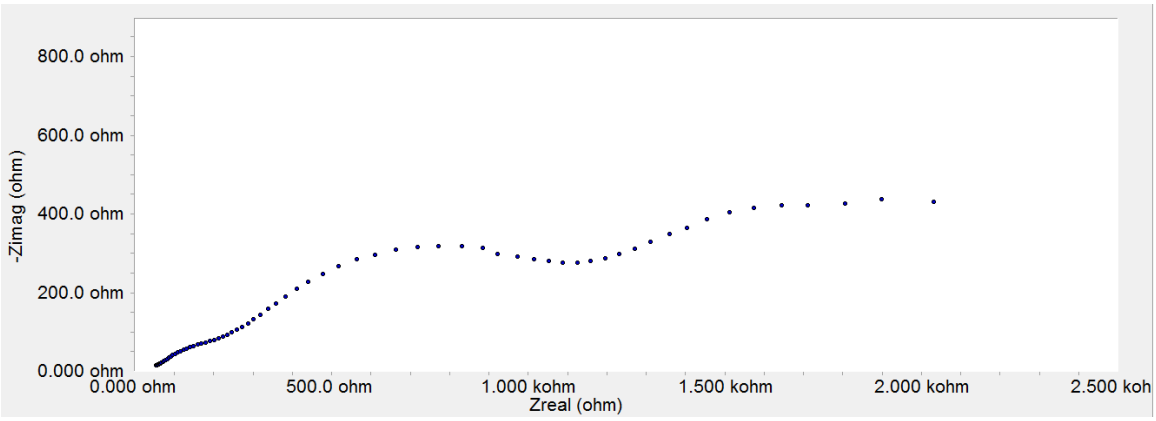

Test b (0.13 days)

Figure 89: Bode and Nyquist Diagrams for YG7 at 0.13 Days of Exposure.

Appendix 1: (Continued)

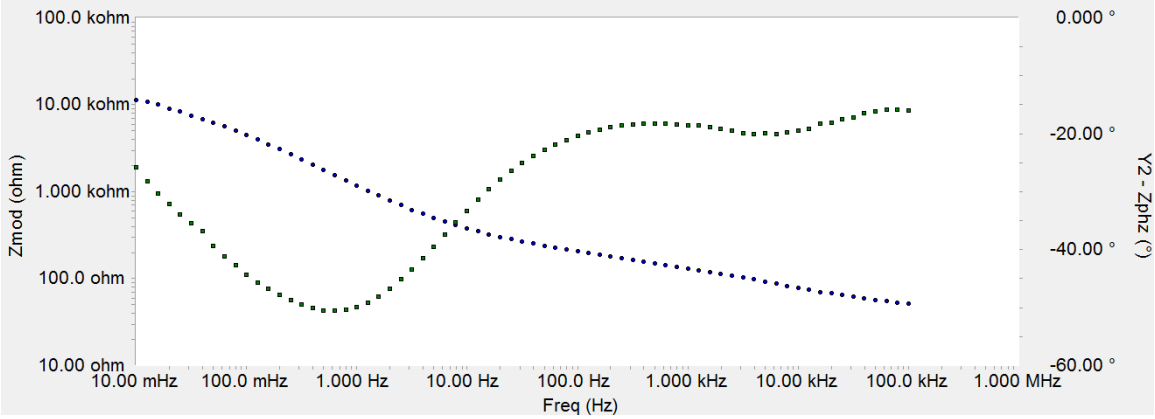

Test c (0.20 days)

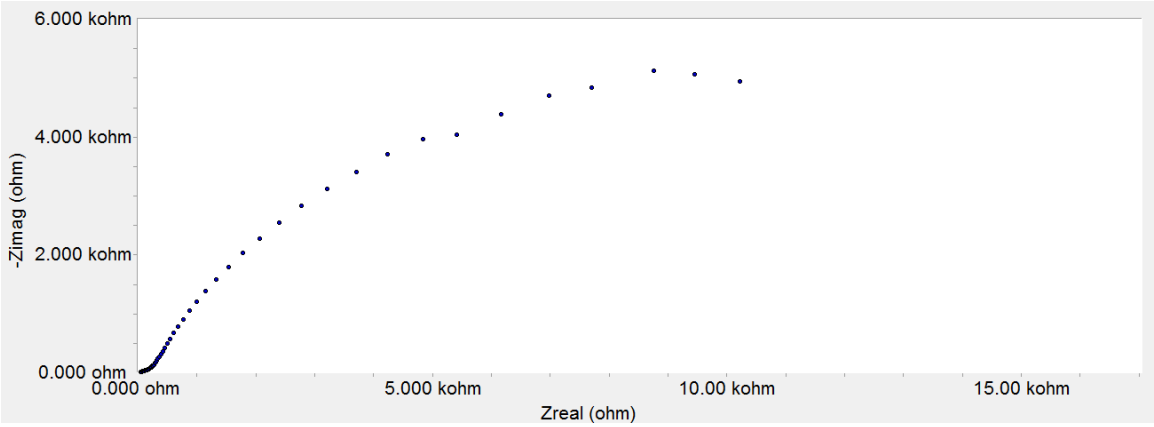

Test c (0.20 days)

Figure 90: Bode and Nyquist Diagrams for YG7 at 0.20 Days of Exposure.

Appendix 1: (Continued)

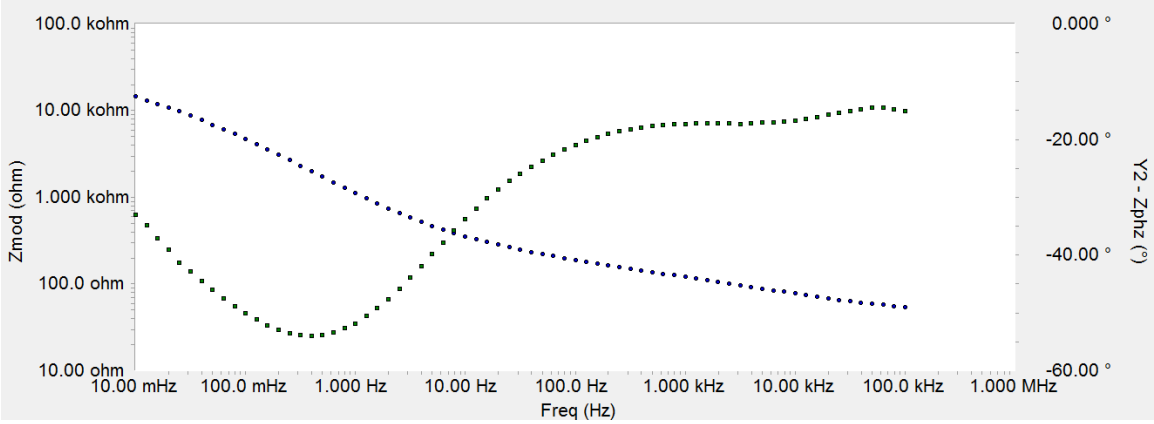

Test d (0.24 days)

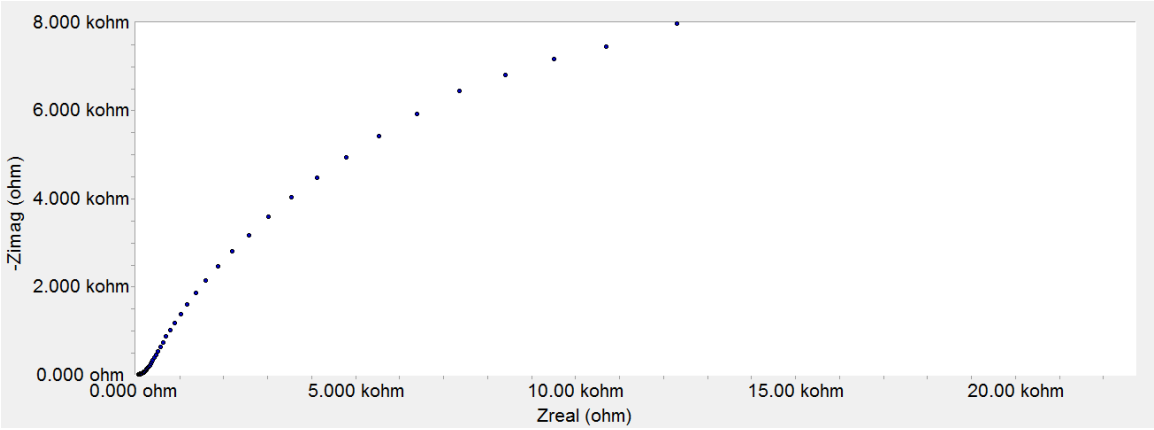

Test d (0.24 days)

Figure 91: Bode and Nyquist Diagrams for YG7 at 0.24 Days of Exposure.

Appendix 1: (Continued)

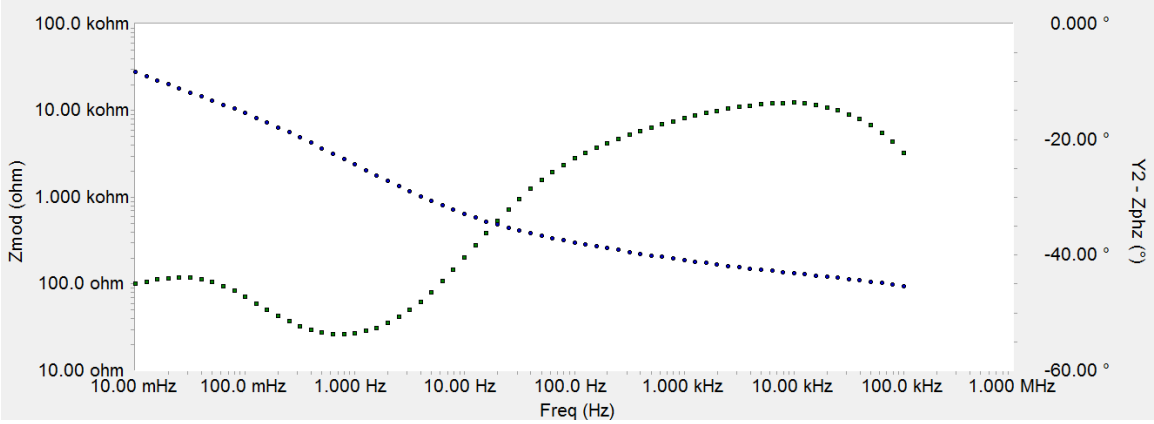

Test e (0.99 days)

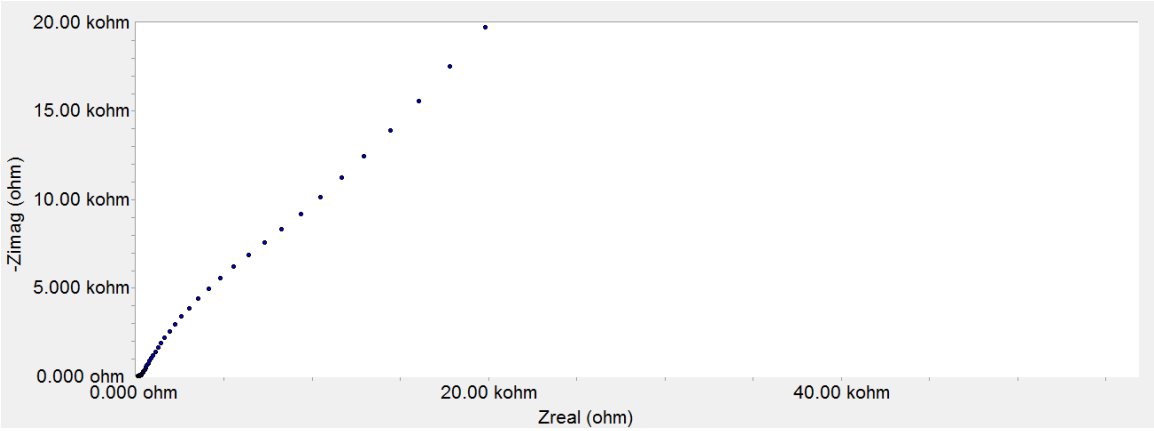

Test e (0.99 days)

Figure 92: Bode and Nyquist Diagrams for YG7 at 0.99 Days of Exposure.

Appendix 1: (Continued)

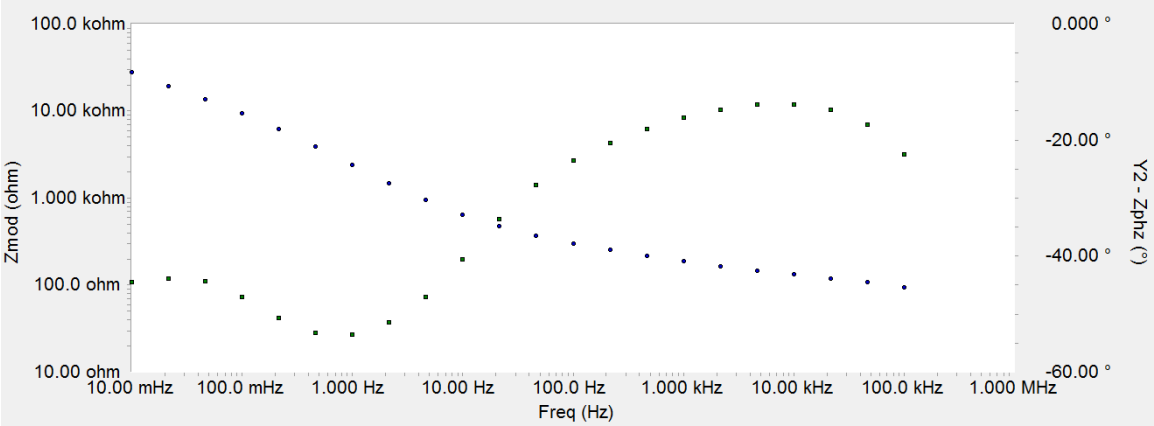

Test f (1.03 days)

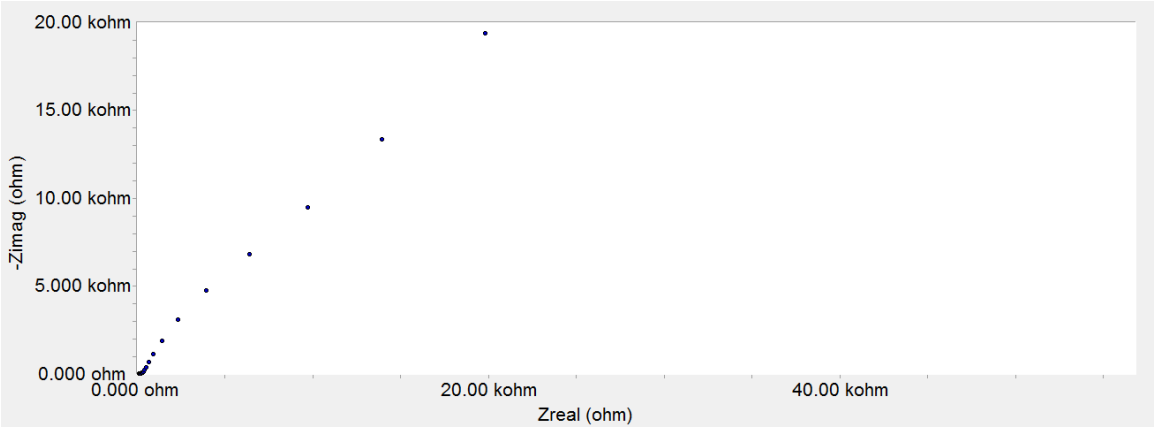

Test f (1.03 days)

Figure 93: Bode and Nyquist Diagrams for YG7 at 1.03 Days of Exposure.

Appendix 1: (Continued)

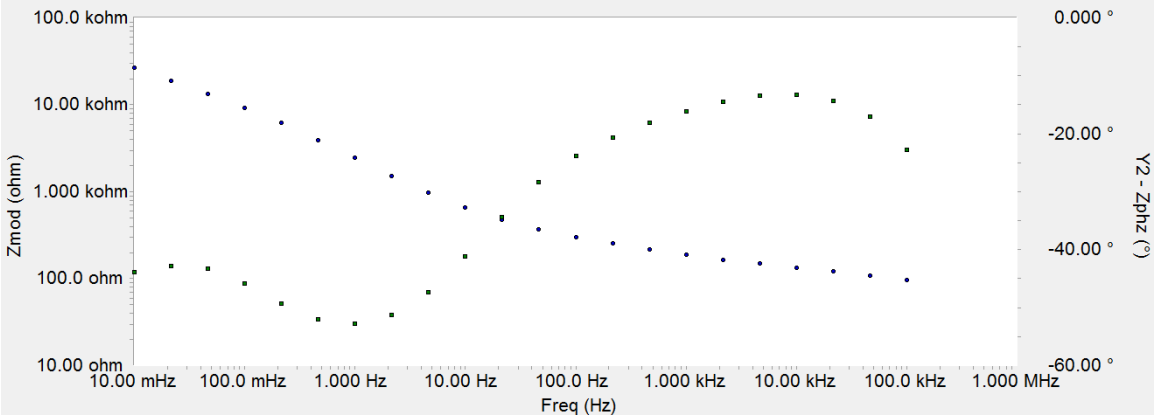

Test g (1.19 days)

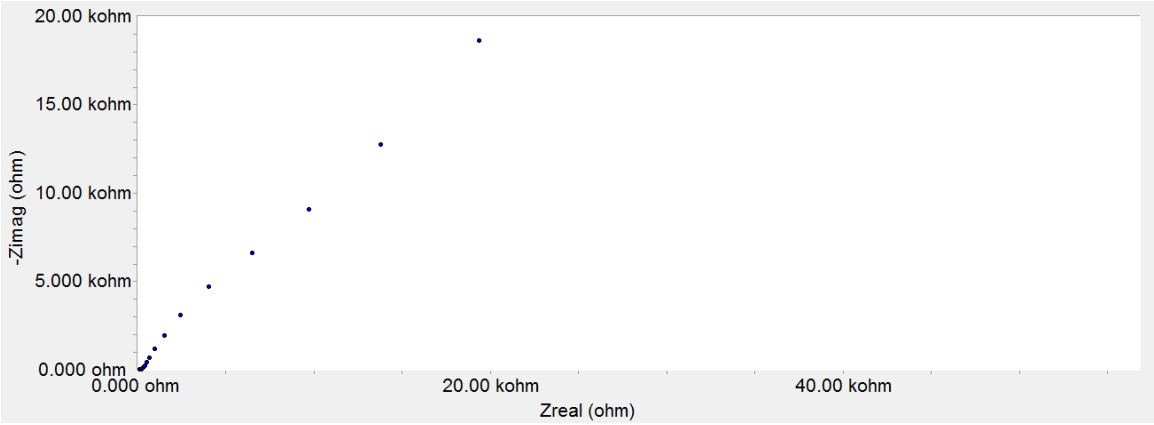

Test g (1.19 days)

Figure 94: Bode and Nyquist Diagrams for YG7 at 1.19 Days of Exposure.

Appendix 1: (Continued)

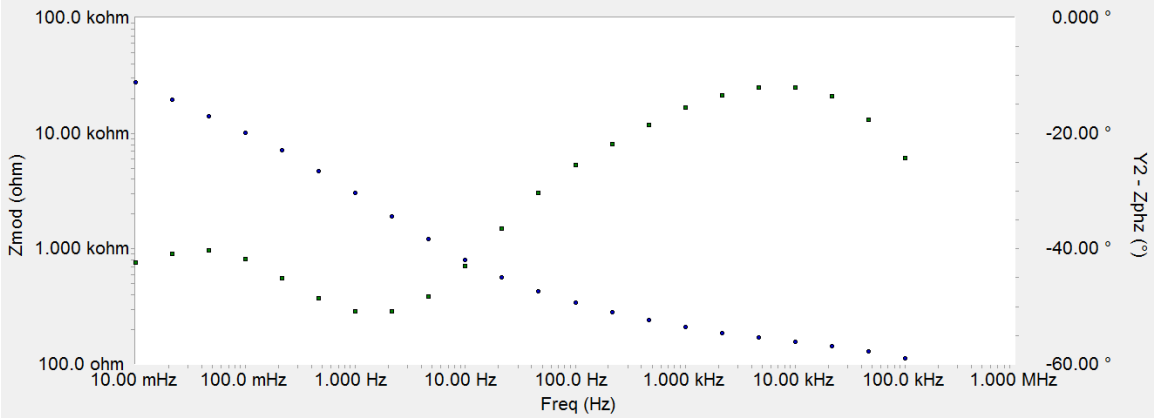

Test h (2.01 days)

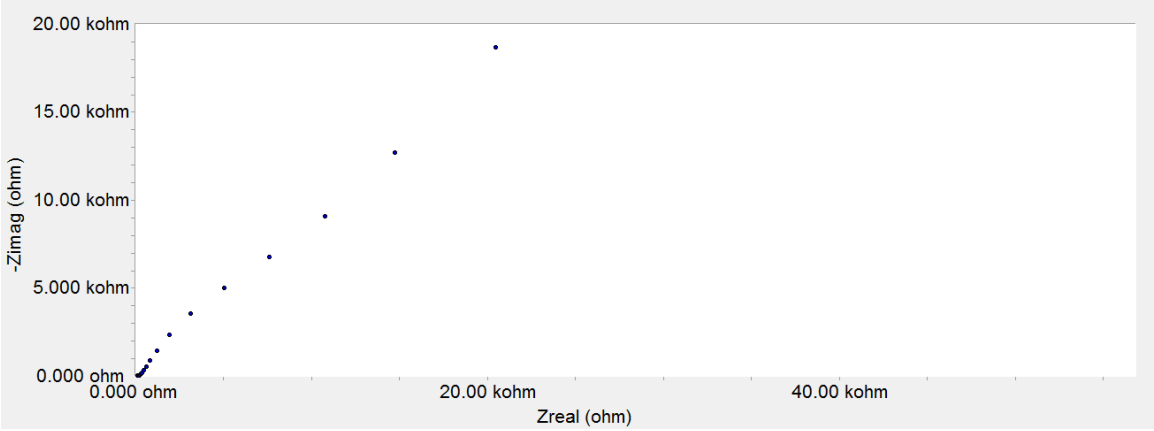

Test h (2.01 days)

Figure 95: Bode and Nyquist Diagrams for YG7 at 2.01 Days of Exposure.

Appendix 1: (Continued)

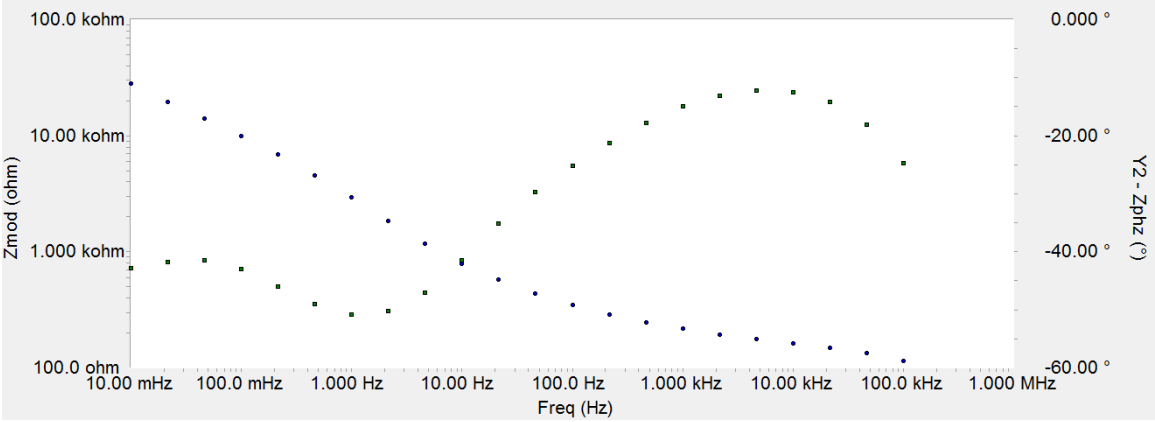

Test i (2.95 days)

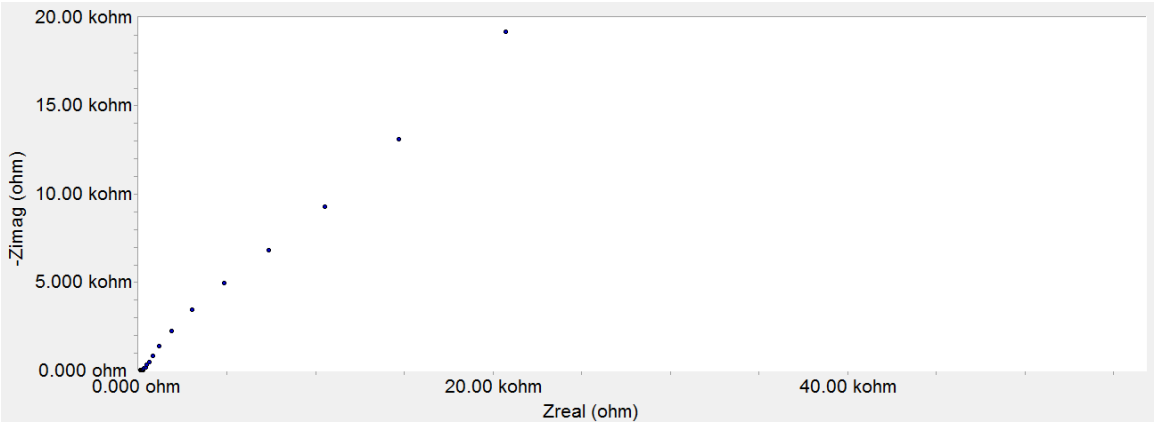

Test i (2.95 days)

Figure 96: Bode and Nyquist Diagrams for YG7 at 2.95 Days of Exposure.

Appendix 1: (Continued)

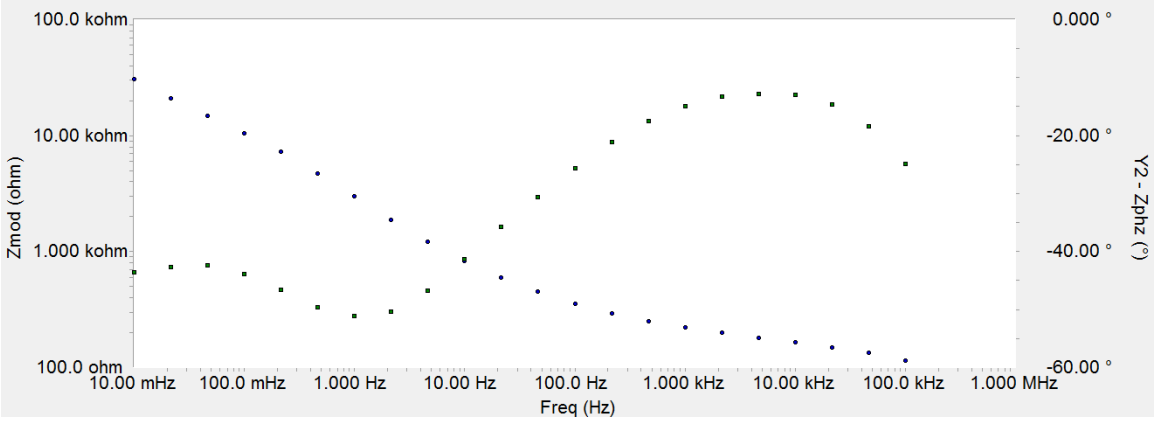

Test j (5.94 days)

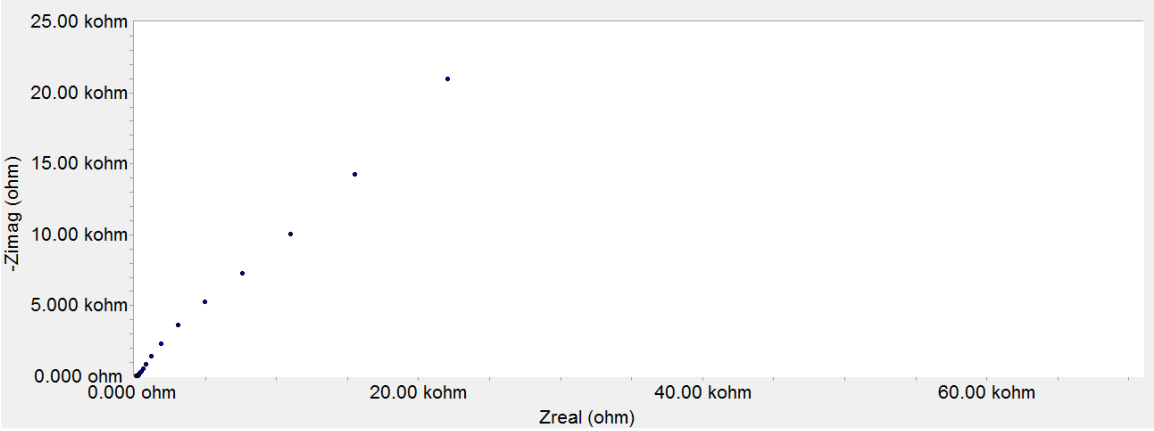

Test j (5.94 days)

Figure 97: Bode and Nyquist Diagrams for YG7 at 5.94 Days of Exposure.

Appendix 1: (Continued)

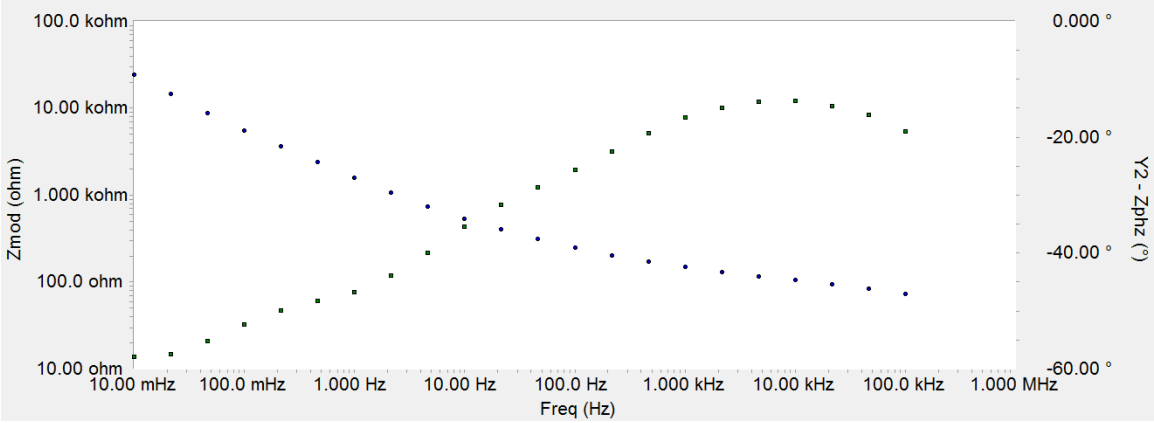

Test k (7.01 days)

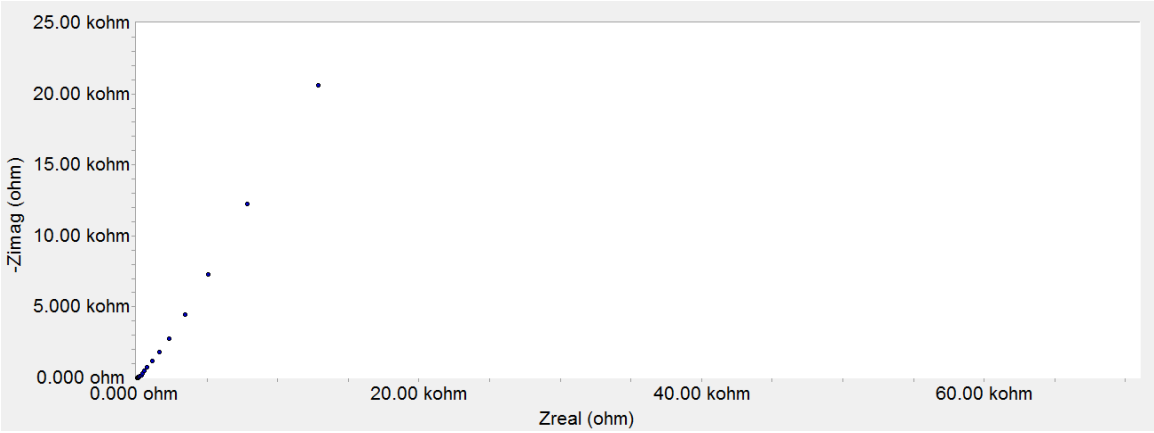

Test k (7.01 days)

Figure 98: Bode and Nyquist Diagrams for YG7 at 7.01 Days of Exposure.

Appendix 1: (Continued)

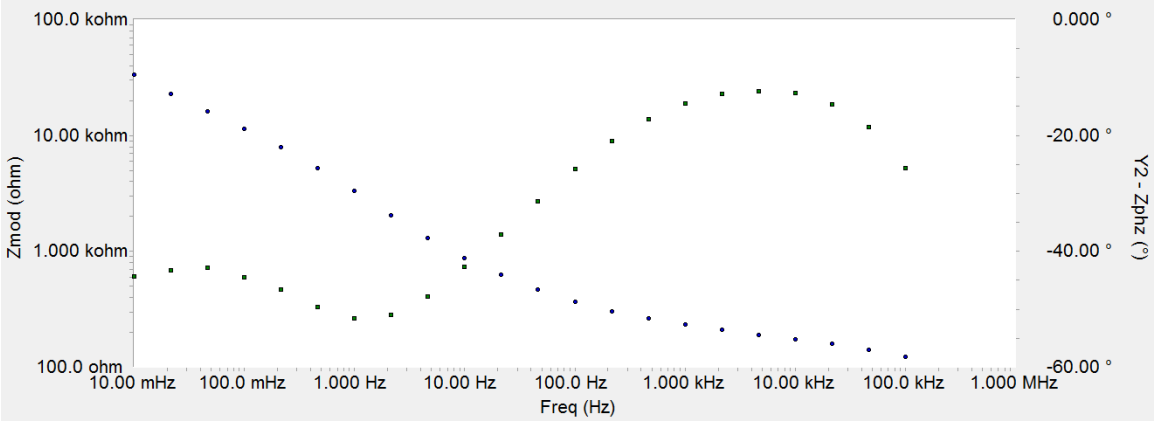

Test l (7.96 days)

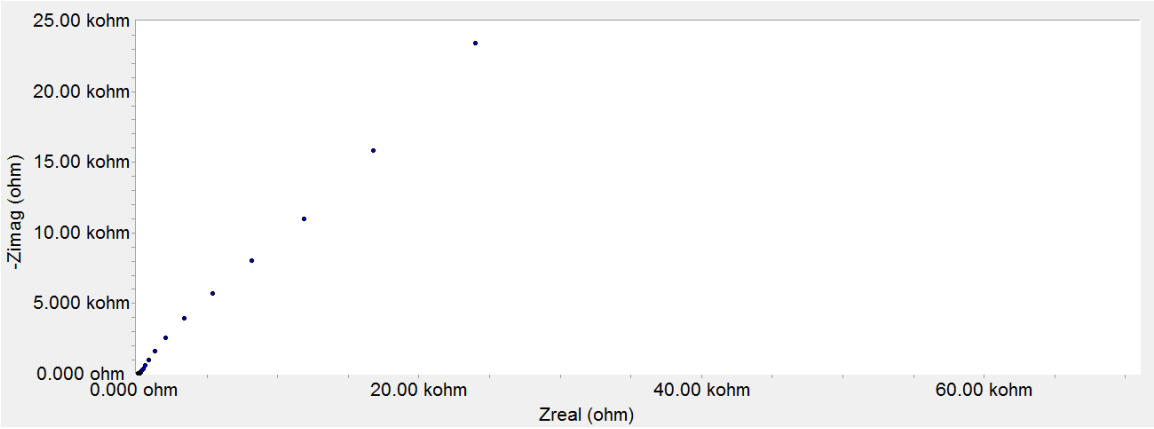

Test l (7.96 days)

Figure 99: Bode and Nyquist Diagrams for YG7 at 7.96 Days of Exposure.

Appendix 1: (Continued)

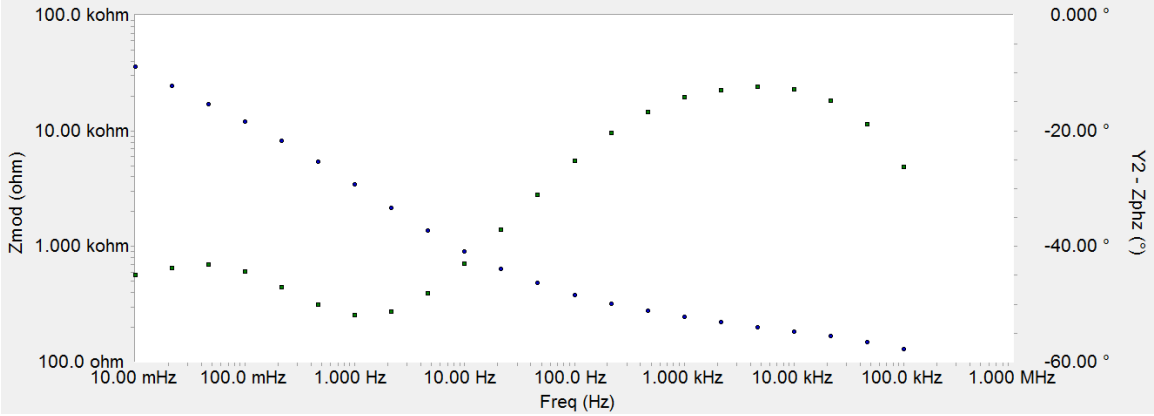

Test m (9.94 days)

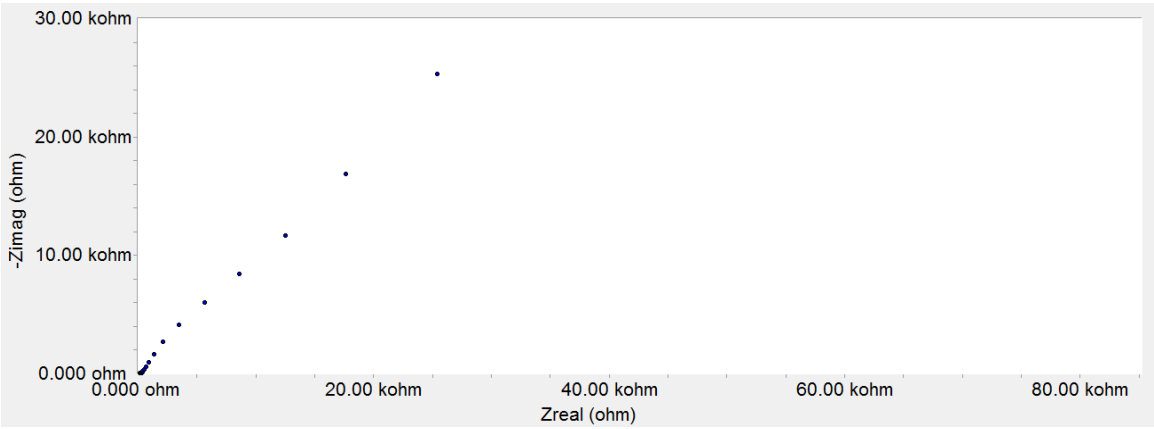

Test m (9.94 days)

Figure 100: Bode and Nyquist Diagrams for YG7 at 9.94 Days of Exposure.

Appendix 1: (Continued)

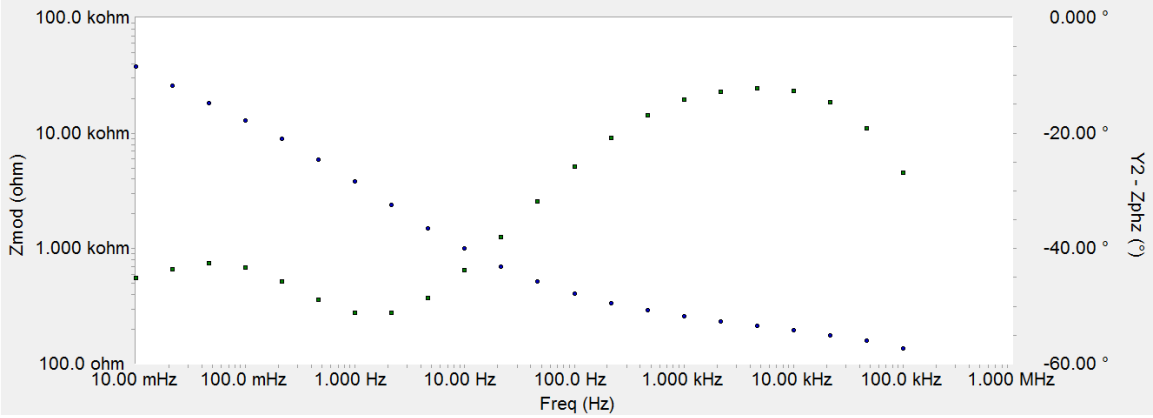

Test n (10.94 days)

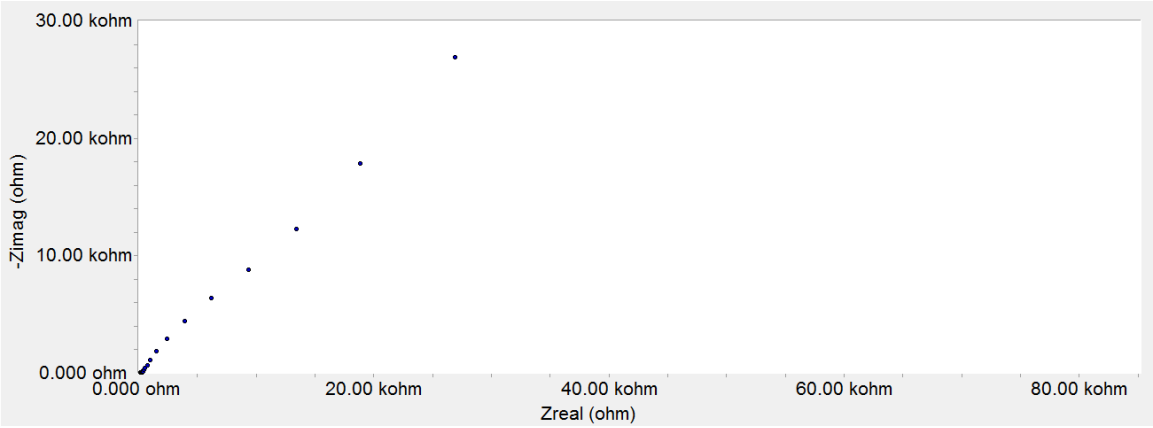

Test n (10.94 days)

Figure 101: Bode and Nyquist Diagrams for YG7 at 10.94 Days of Exposure.

Appendix 1: (Continued)

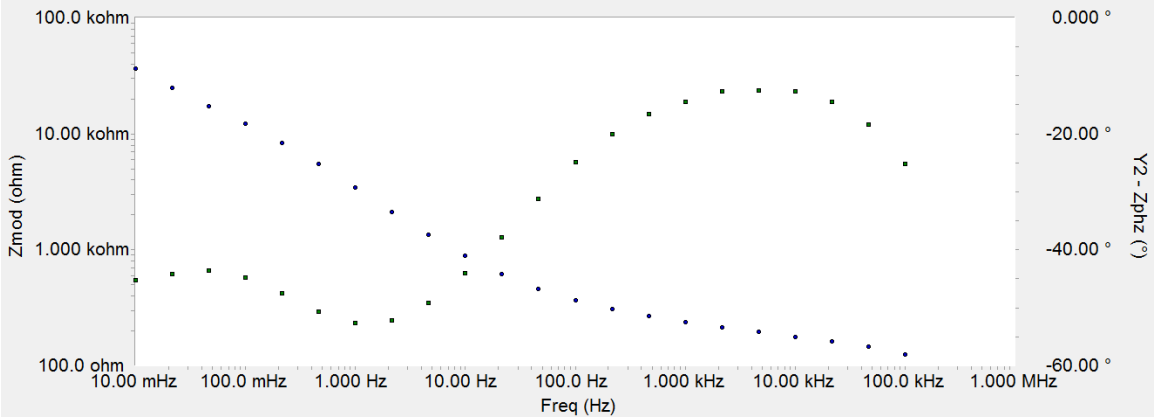

Test o (12.95 days)

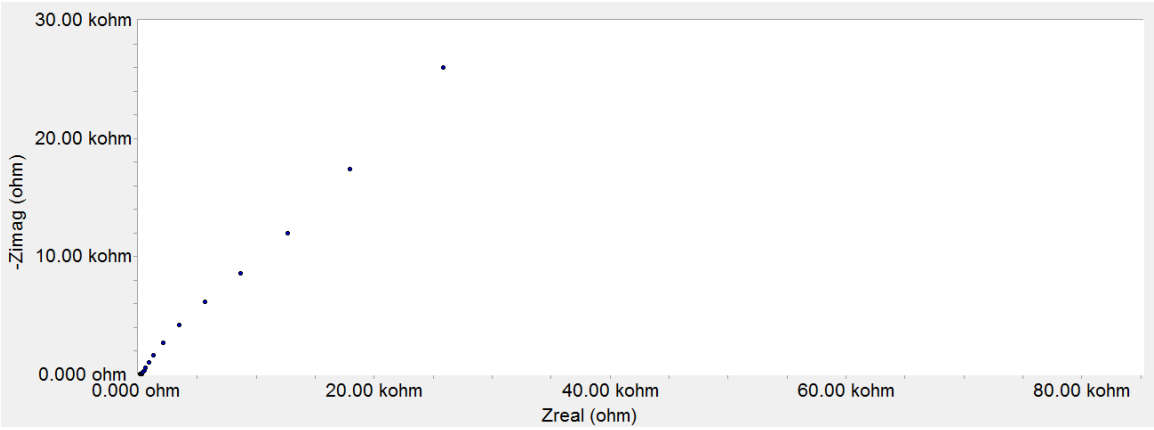

Test o (12.95 days)

Figure 102: Bode and Nyquist Diagrams for YG7 at 12.95 Days of Exposure.

Appendix 1: (Continued)

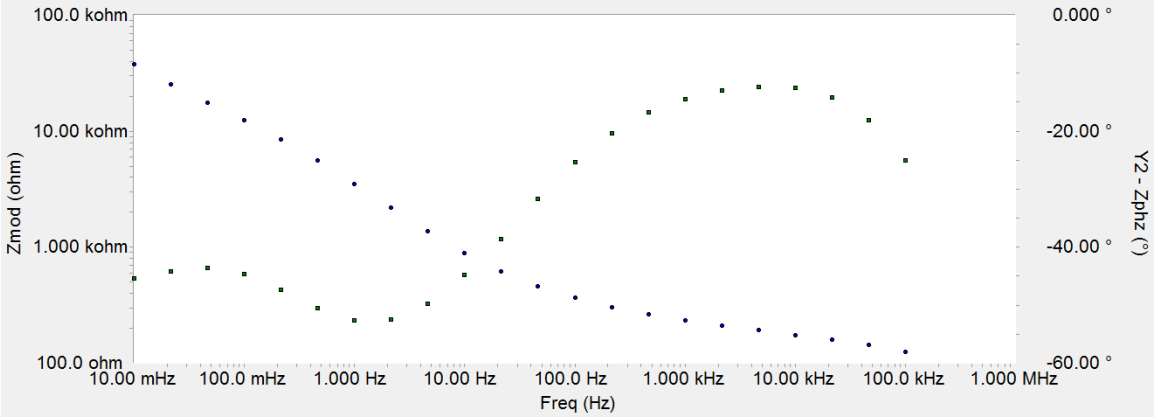

Test p (14.06 days)

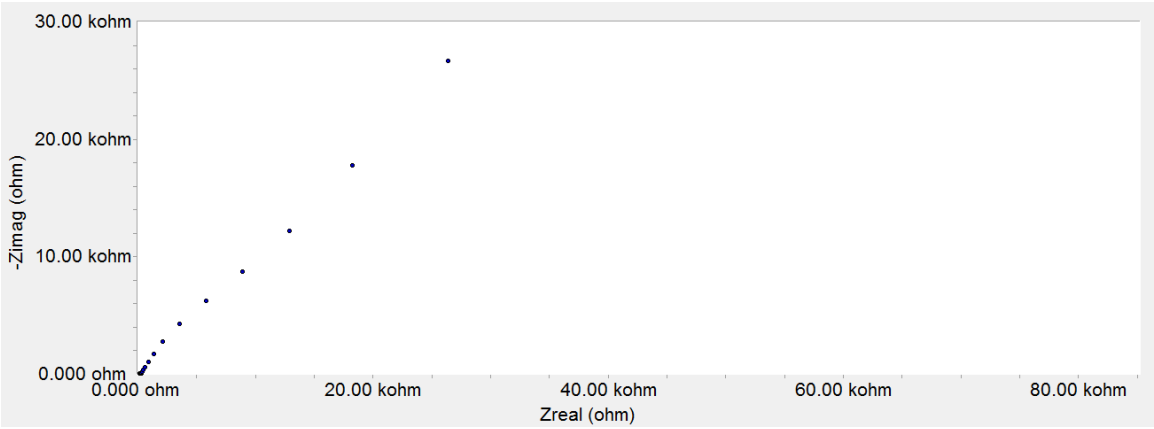

Test p (14.06 days)

Figure 103: Bode and Nyquist Diagrams for YG7 at 14.06 Days of Exposure.

Appendix 1: (Continued)

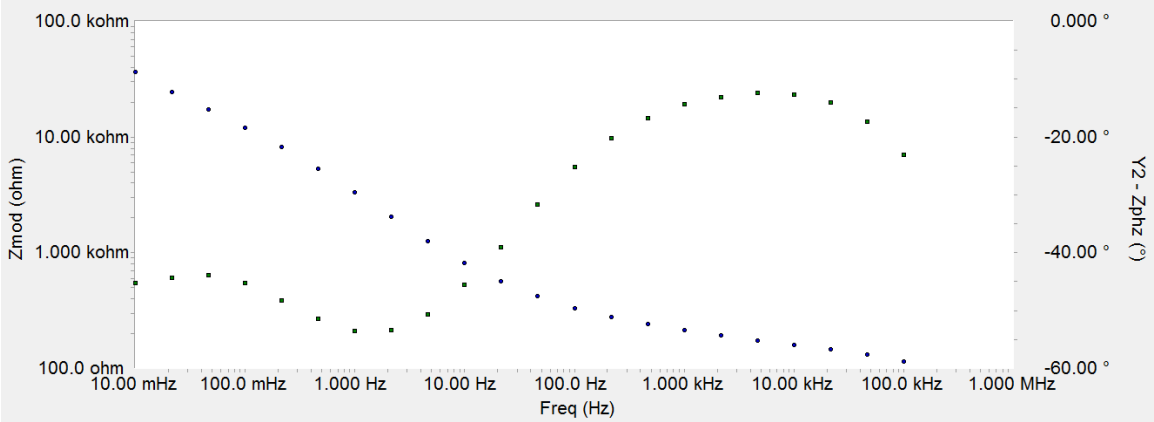

Test q (16 days)

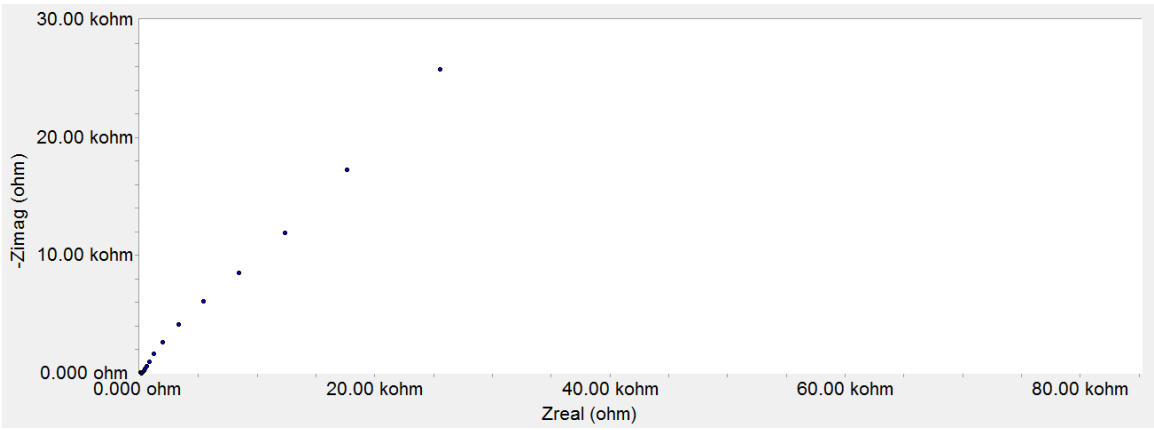

Test q (16 days)

Figure 104: Bode and Nyquist Diagrams for YG7 at 16 Days of Exposure.

Appendix 1: (Continued)

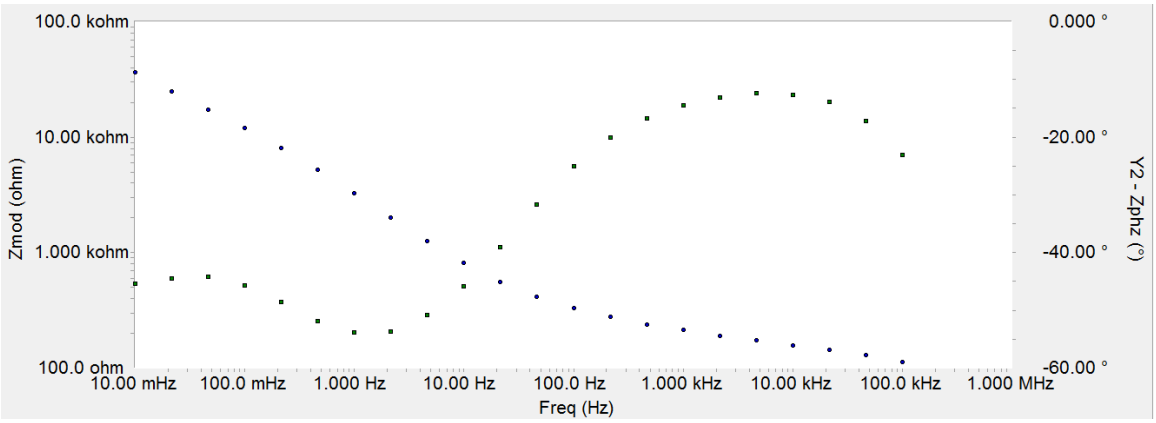

Test r (16.96 days)

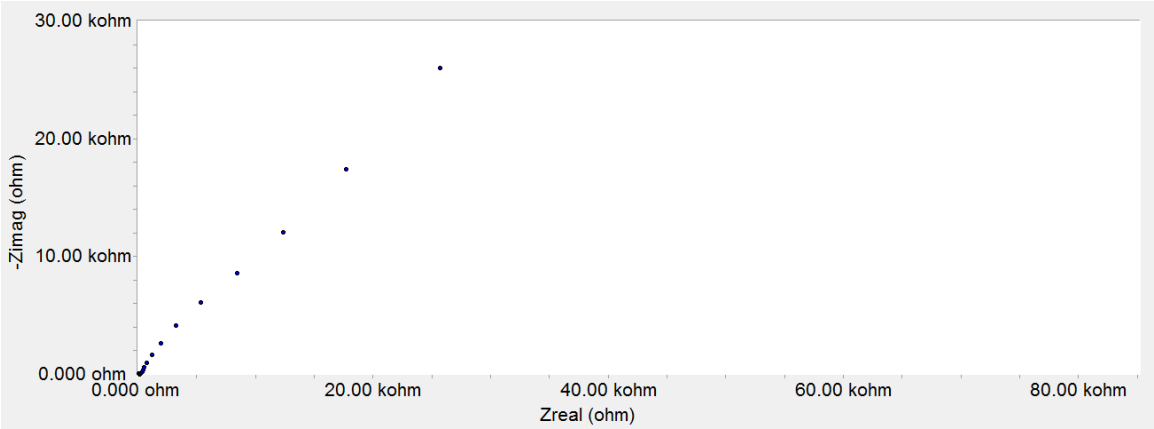

Test r (16.96 days)

Figure 105: Bode and Nyquist Diagrams for YG7 at 16.96 Days of Exposure.

Appendix 1: (Continued)

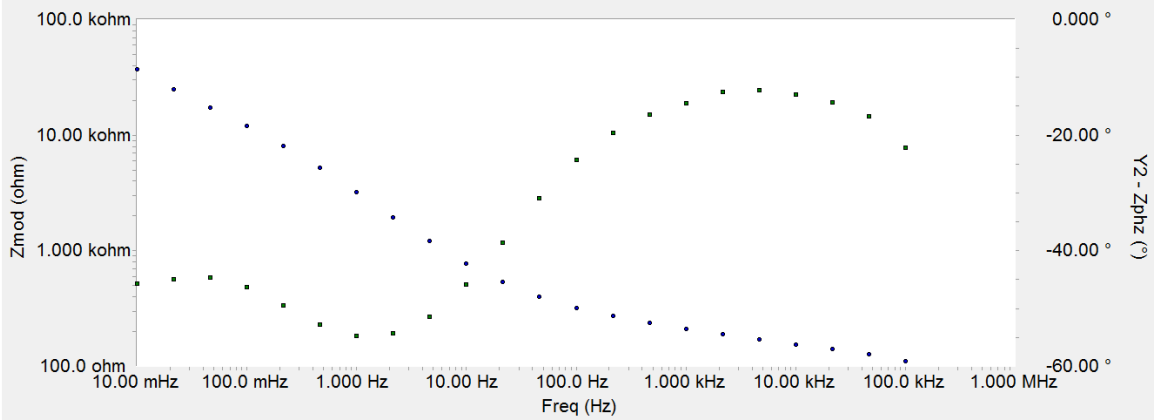

Test s (19.95 days)

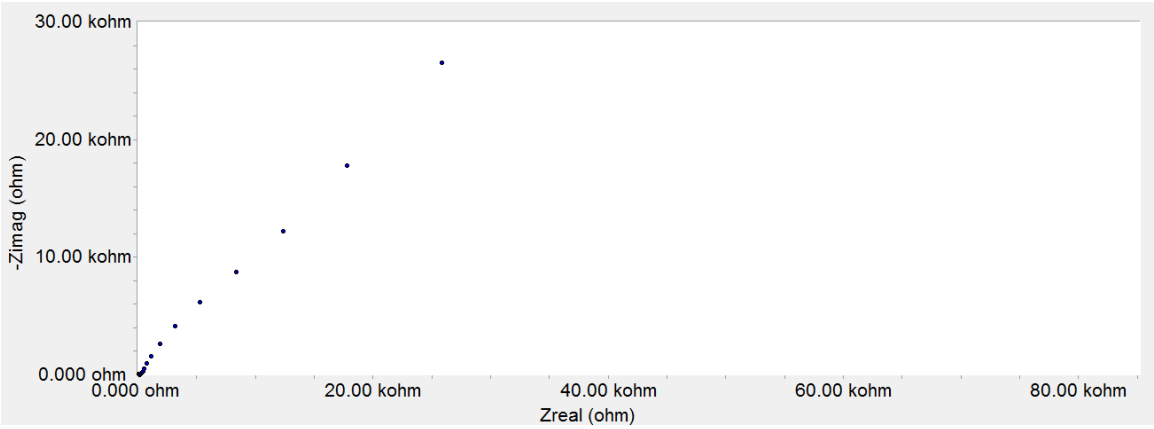

Test s (19.95 days)

Figure 106: Bode and Nyquist Diagrams for YG7 at 19.95 Days of Exposure.

Appendix 1: (Continued)

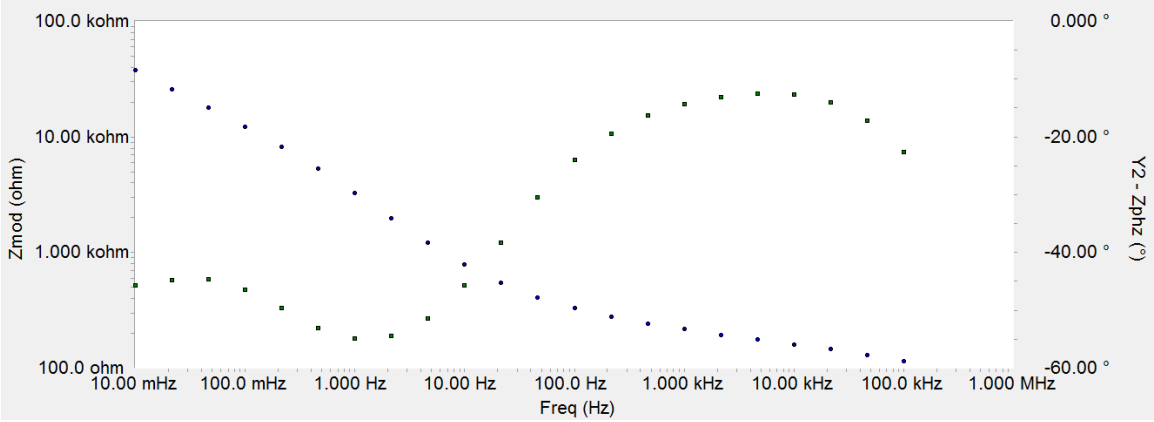

Test t (21.02 days)

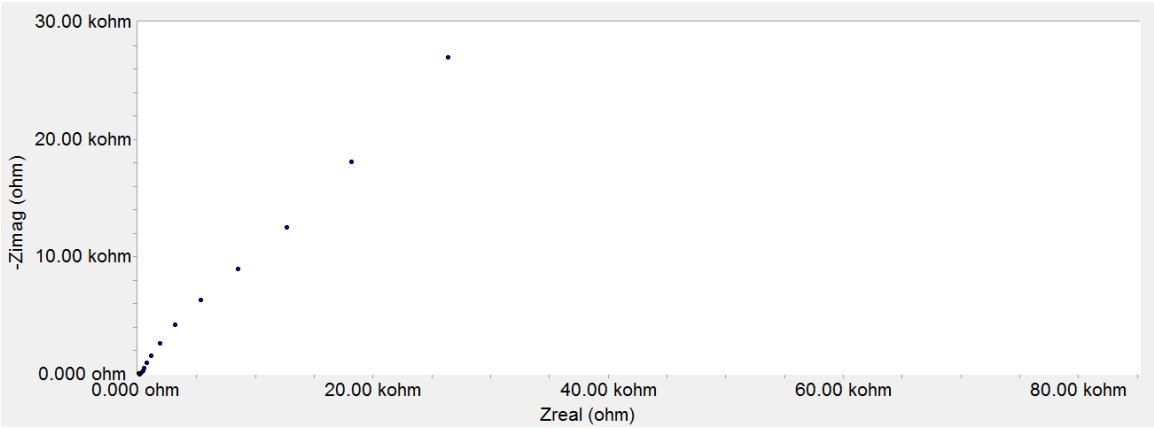

Test t (21.02 days)

Figure 107: Bode and Nyquist Diagrams for YG7 at 21.02 Days of Exposure.

Appendix 1: (Continued)

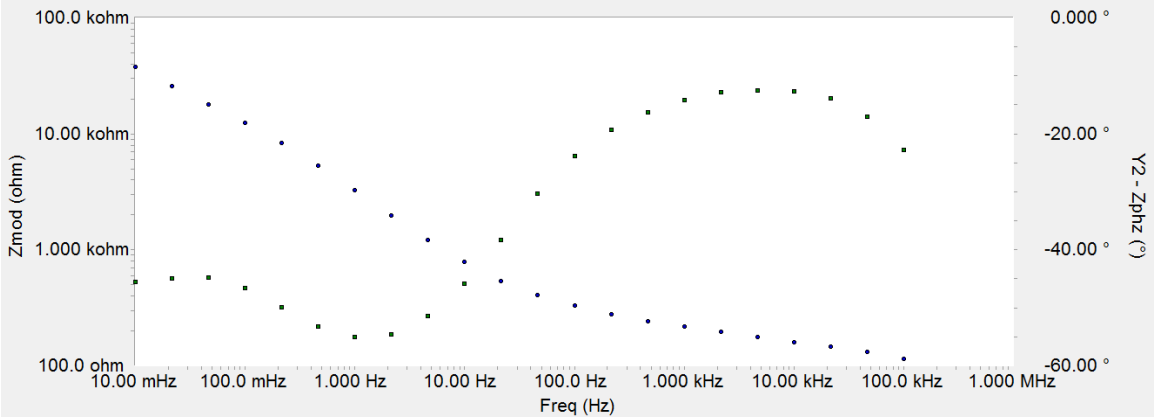

Test u (21.94 days)

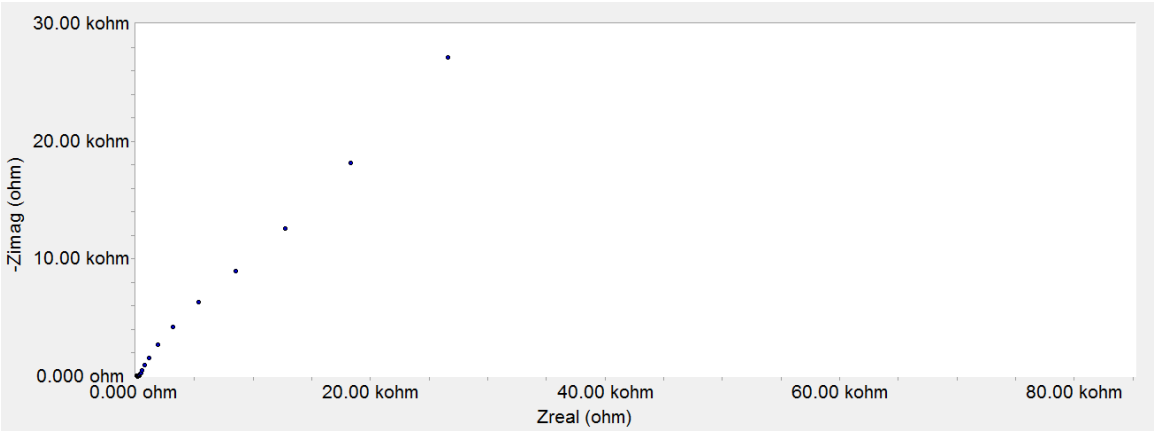

Test u (21.94 days)

Figure 108: Bode and Nyquist Diagrams for YG7 at 21.94 Days of Exposure.

Appendix 1: (Continued)

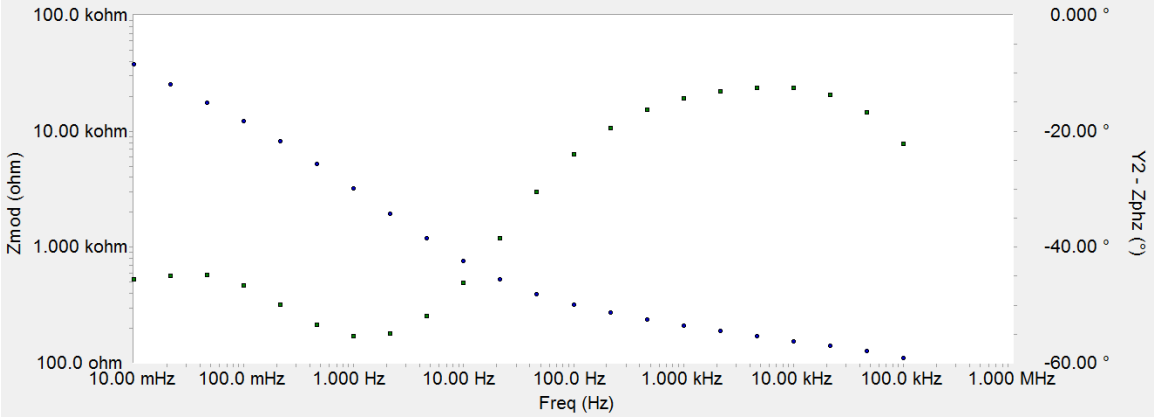

Test v (23.09 days)

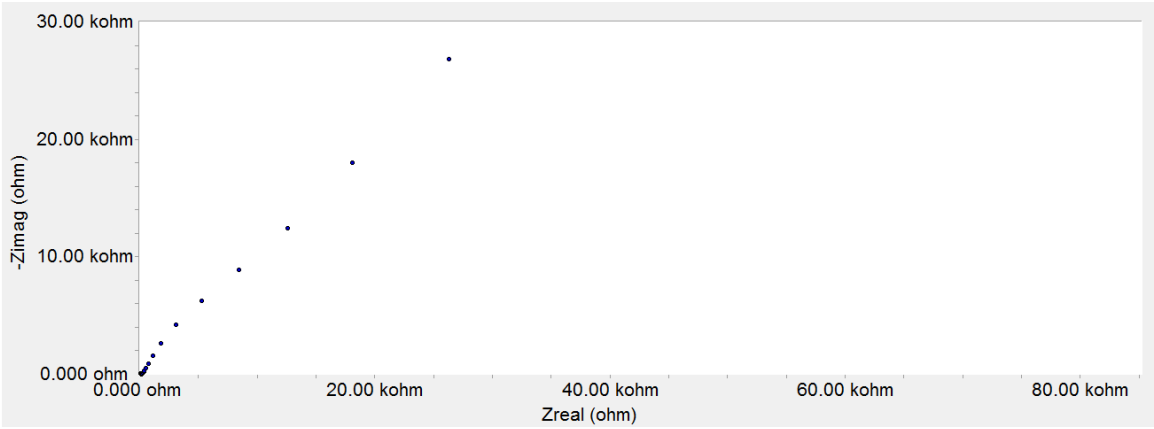

Test v (23.09 days)

Figure 109: Bode and Nyquist Diagrams for YG7 at 23.09 Days of Exposure.

Appendix 1: (Continued)

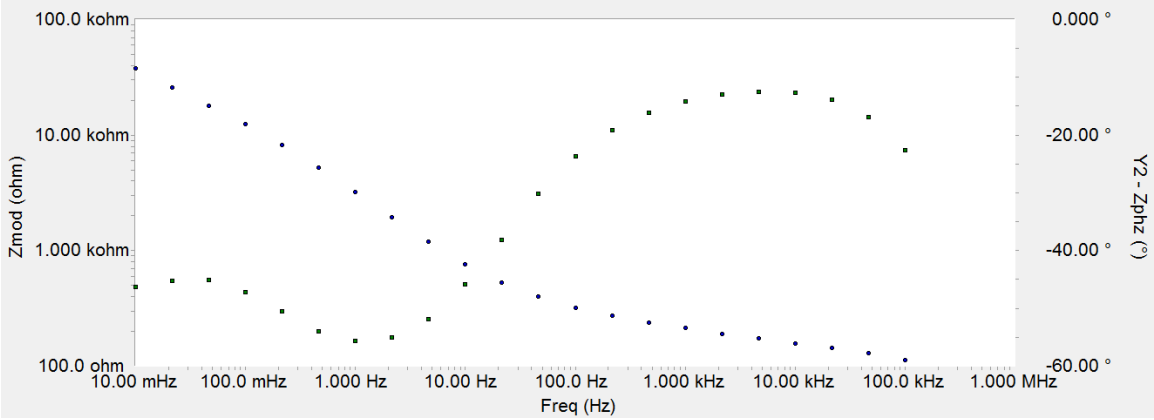

Test w (24.16 days)

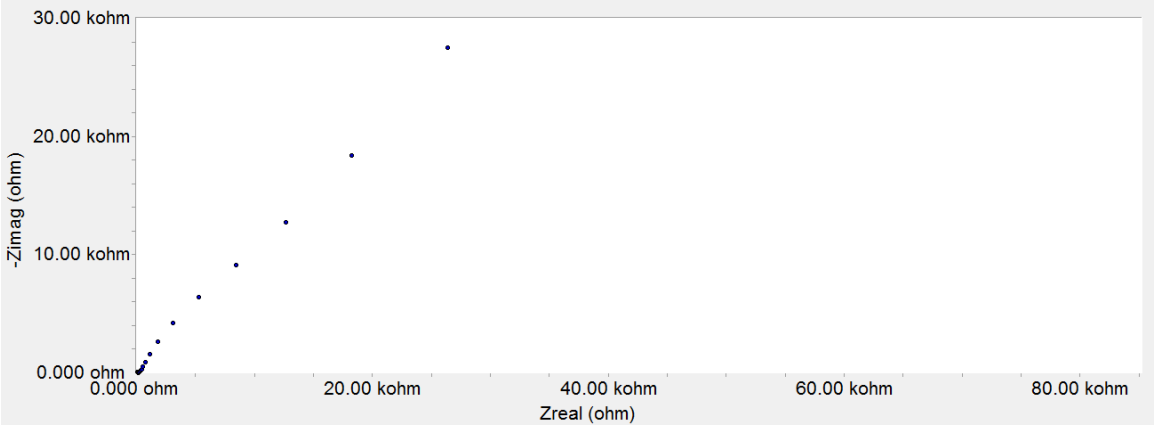

Test w (24.16 days)

Figure 110: Bode and Nyquist Diagrams for YG7 at 24.16 Days of Exposure.

Appendix 1: (Continued)

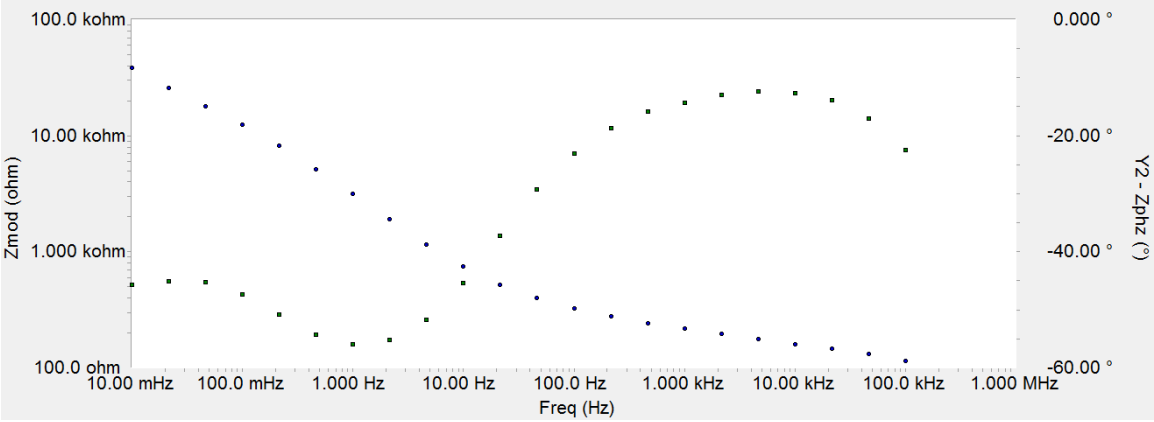

Test x (27.04 days)

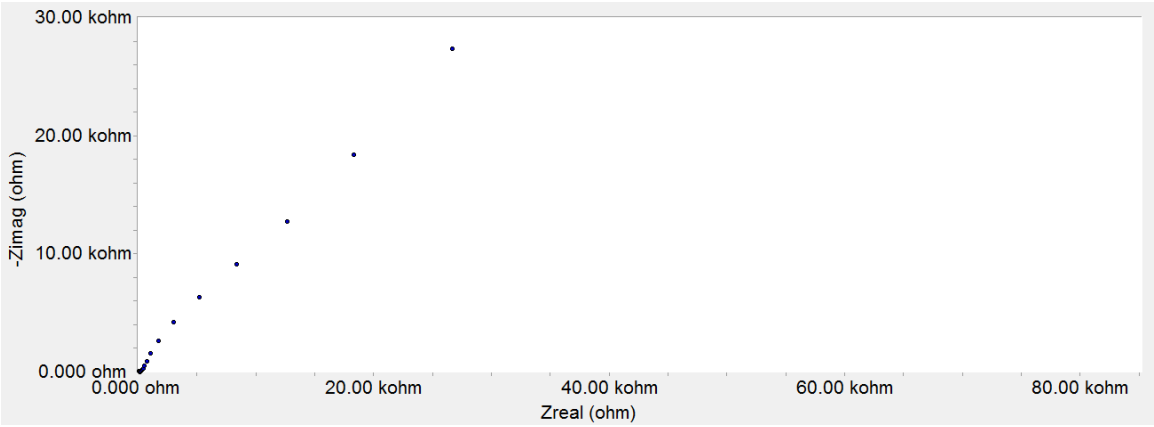

Test x (27.04 days)

Figure 111: Bode and Nyquist Diagrams for YG7 at 27.04 Days of Exposure.

Appendix 1: (Continued)

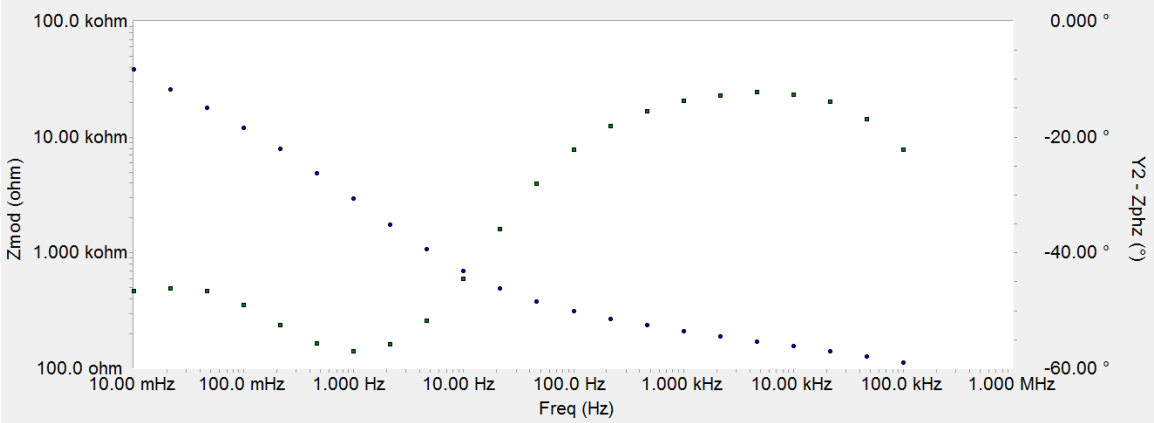

Test y (34.03 days)

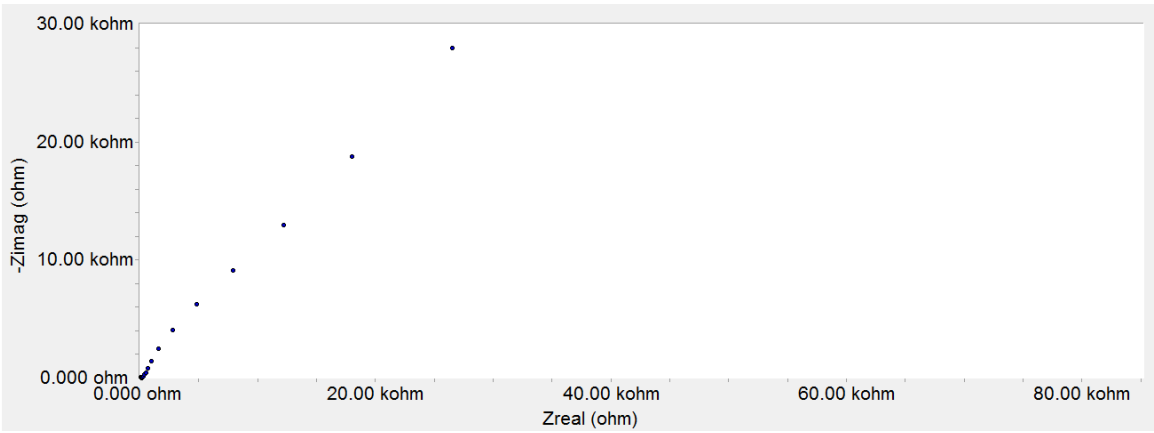

Test y (34.03 days)

Figure 112: Bode and Nyquist Diagrams for YG7 at 34.03 Days of Exposure.

Appendix 1: (Continued)

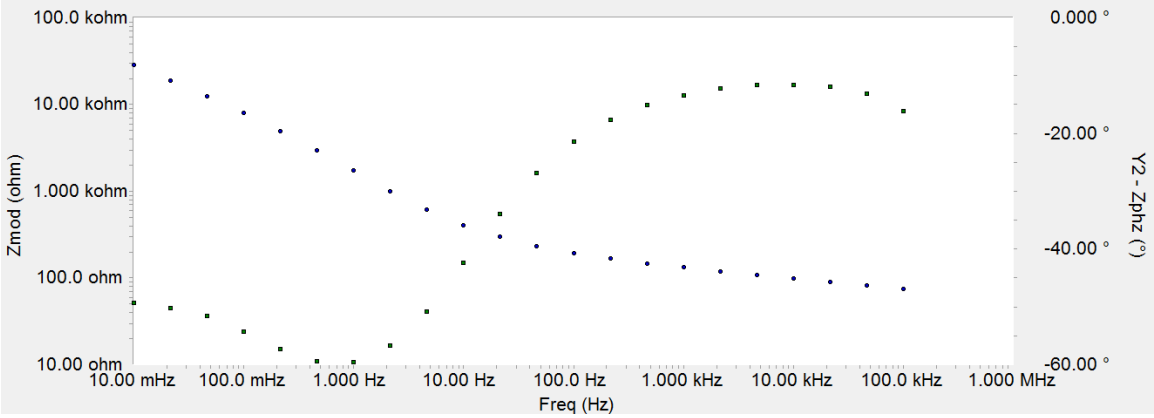

Test z (63.08 days)

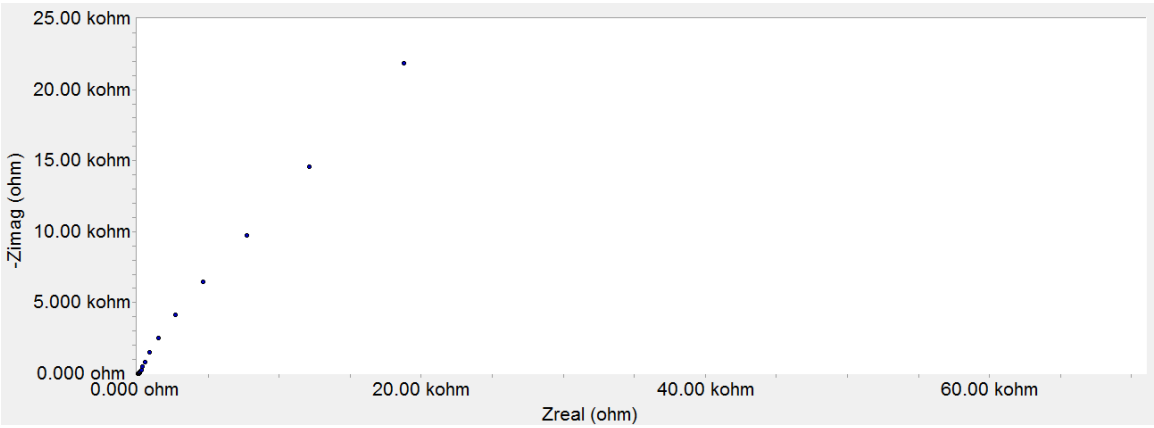

Test z (63.08 days)

Figure 113: Bode and Nyquist Diagrams for YG7 at 63.08 Days of Exposure.

Appendix 1: (Continued)

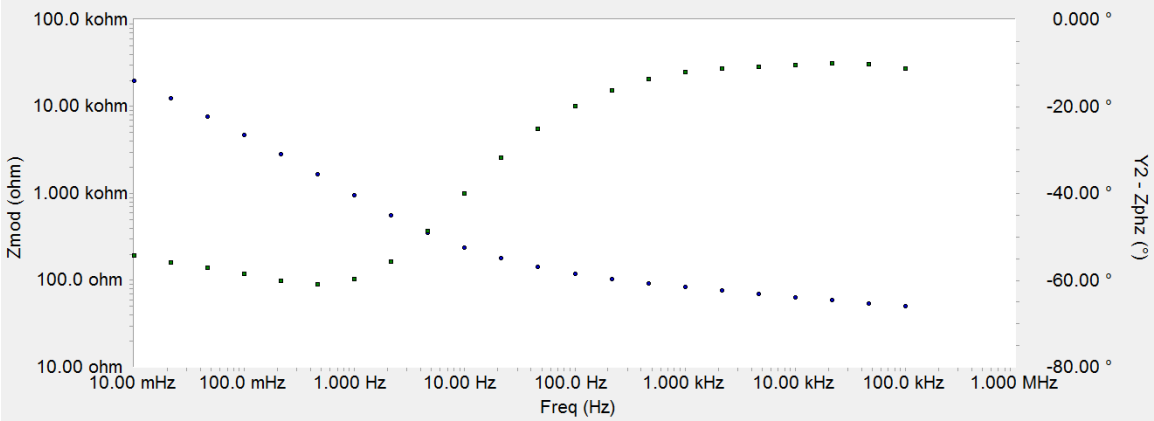

Test aa (97.93 days)

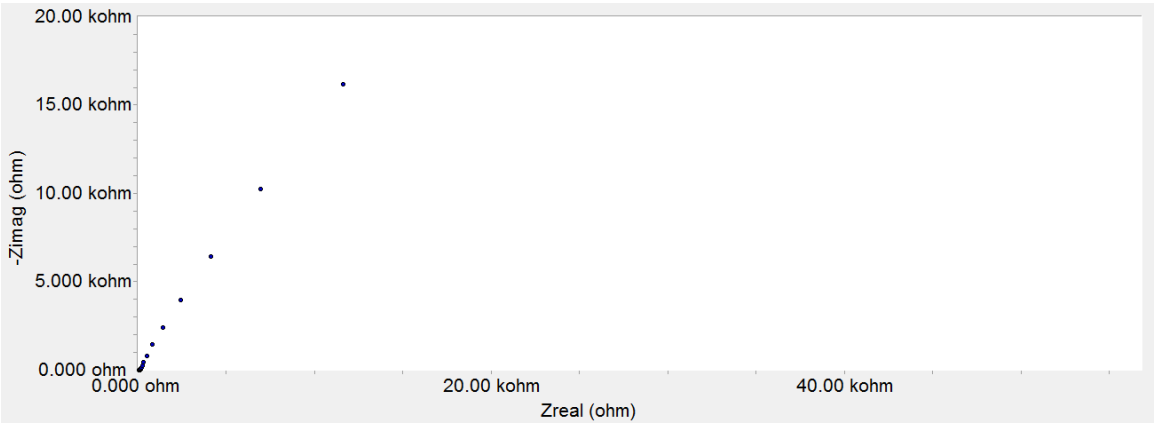

Test aa (97.93 days)

Figure 114: Bode and Nyquist Diagrams for YG7 at 97.93 Days of Exposure.

Appendix 2: Metallographic Pictures

The following contains metallographic pictures of specimens. The magnification is 15x except where noted. The locations pictured are on the defect and off the defect as illustrated below. These will allow a comparison of zinc thickness between that on the defect surface and that under the coating.

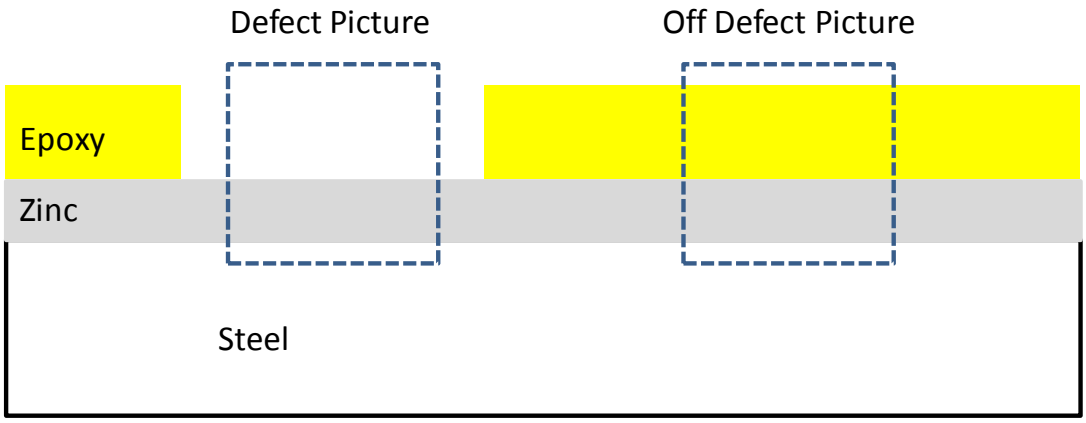

Figure 115: Metallographic Picture Location Diagram

Appendix 2: (Continued)
OCP No-chloride

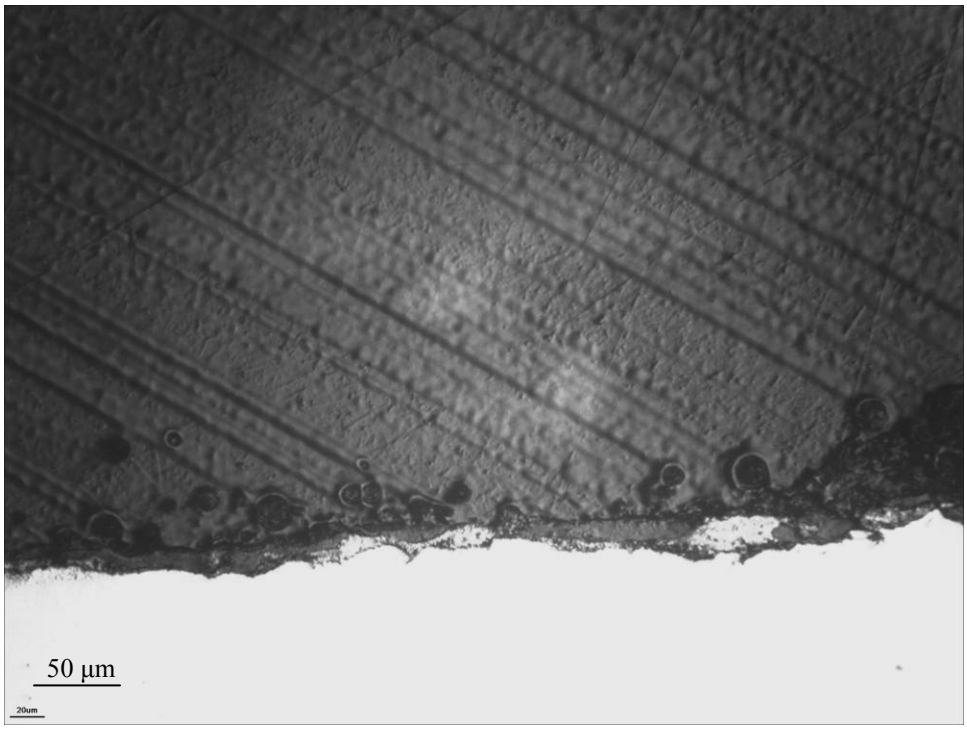

Figure 116: YG7 defect

Figure 117: YG7 off defect

Appendix 2: (Continued)
+100 mV No-chloride

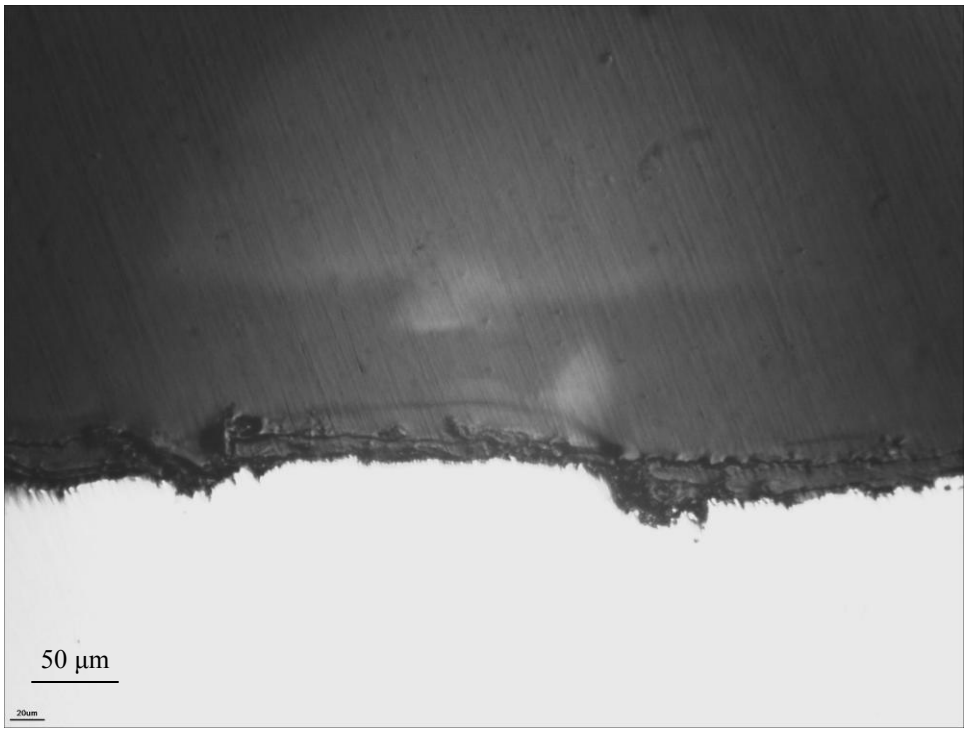

Figure 118: YG2 defect

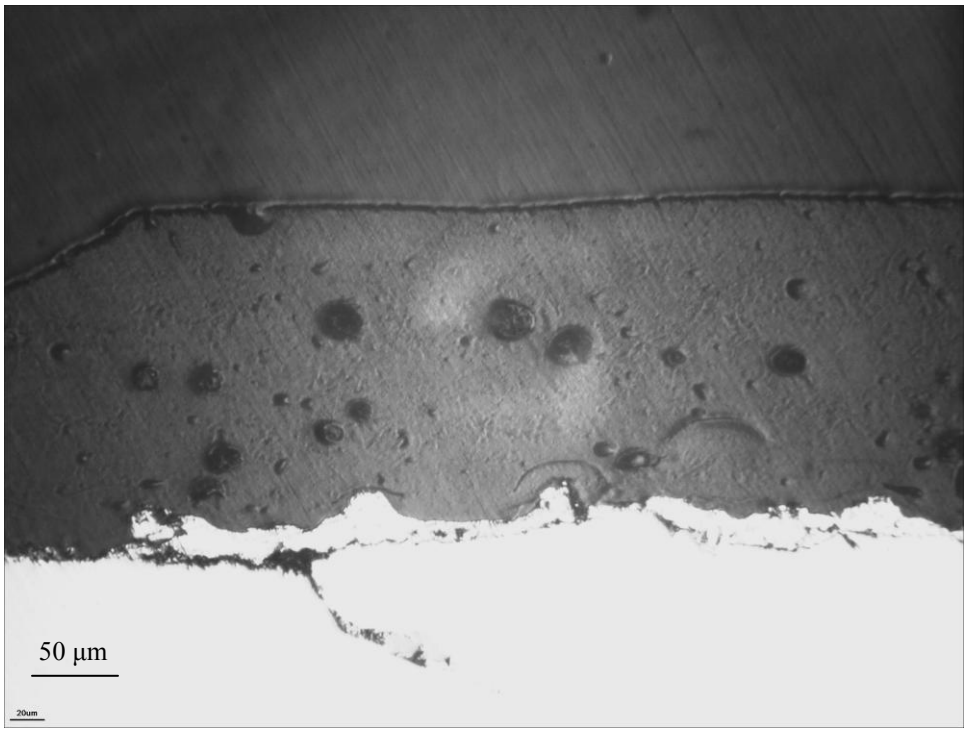

Figure 119: YG2 off defect

Appendix 2: (Continued)
-500 mV No-chloride

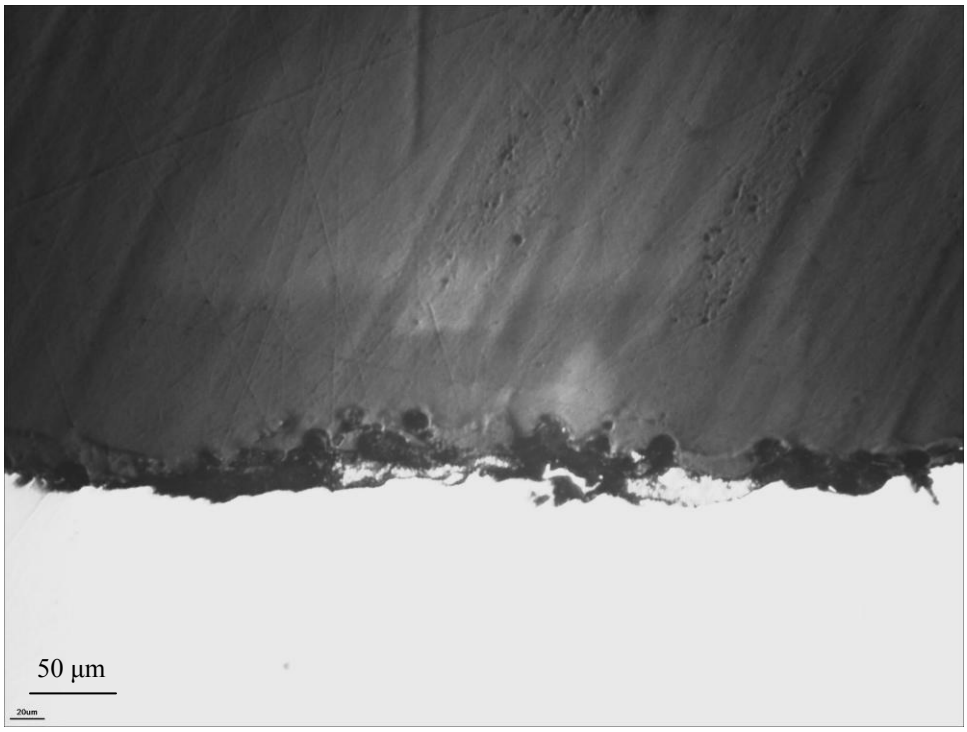

Figure 120: YG4 defect

Figure 121: YG4 off defect

Appendix 2: (Continued)
-1000 mV No-chloride

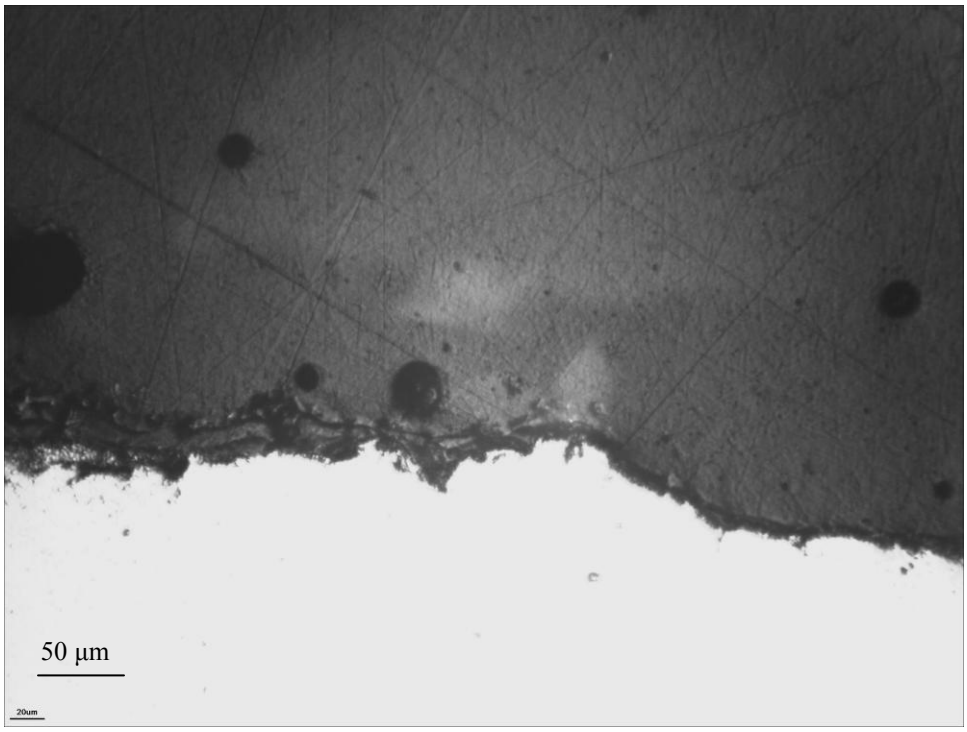

Figure 122: YG18 defect

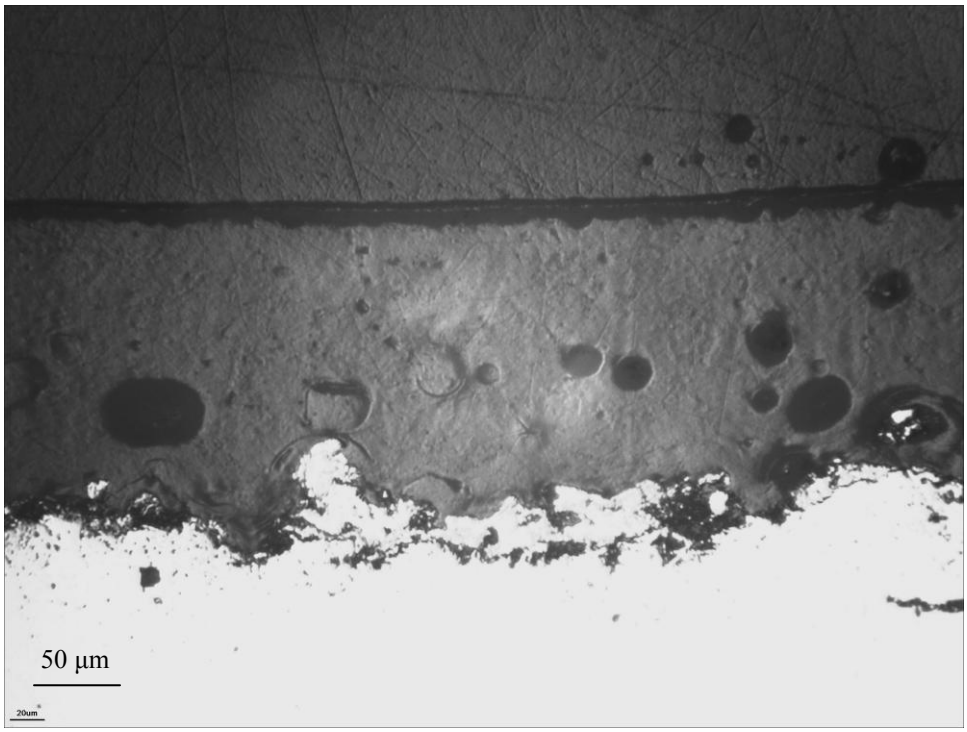

Figure 123: YG18 off defect

Appendix 2: (Continued)
OCP Chloride

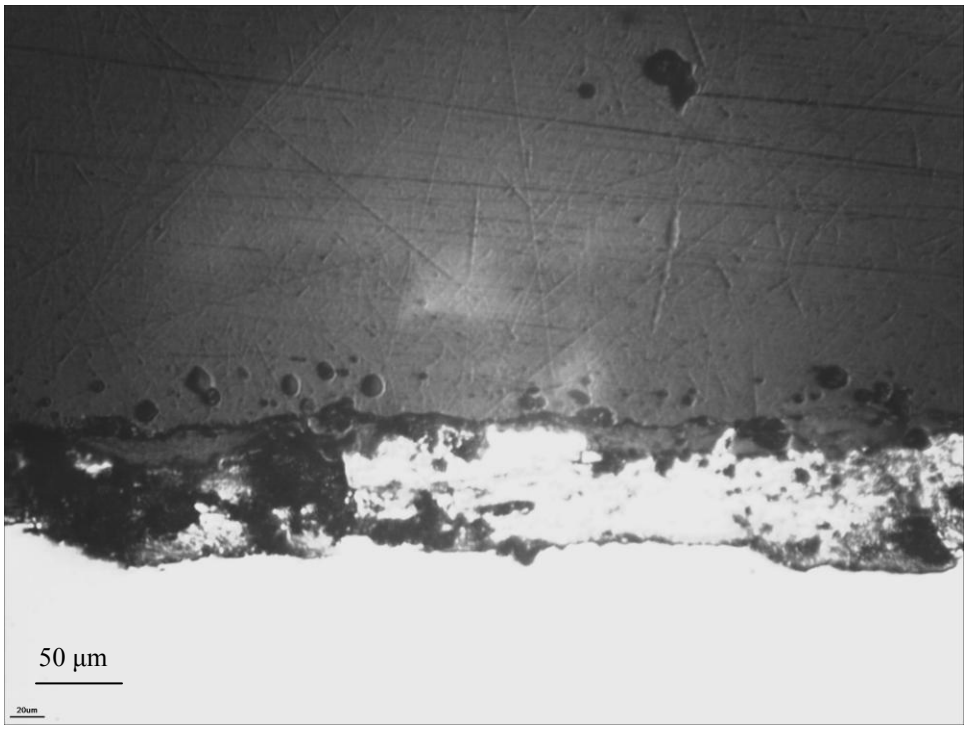

Figure 124: YG6 defect

Figure 125: YG6 off defect

Appendix 2: (Continued)
+100 mV Chloride

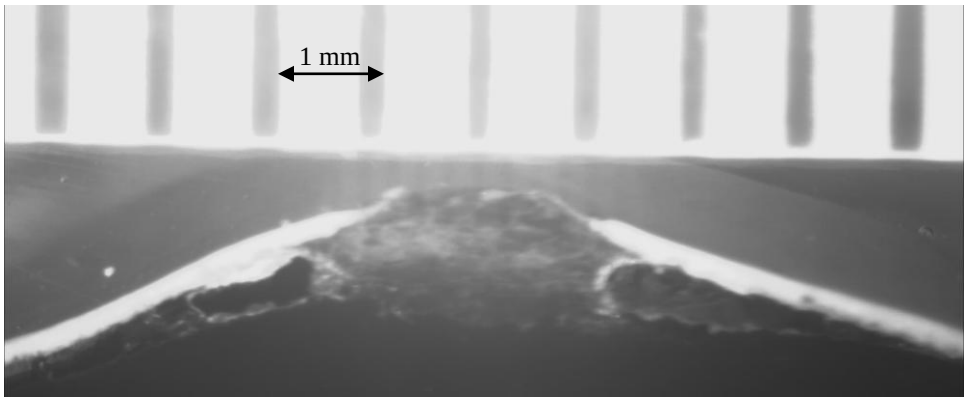

Figure 126: YG3 defect

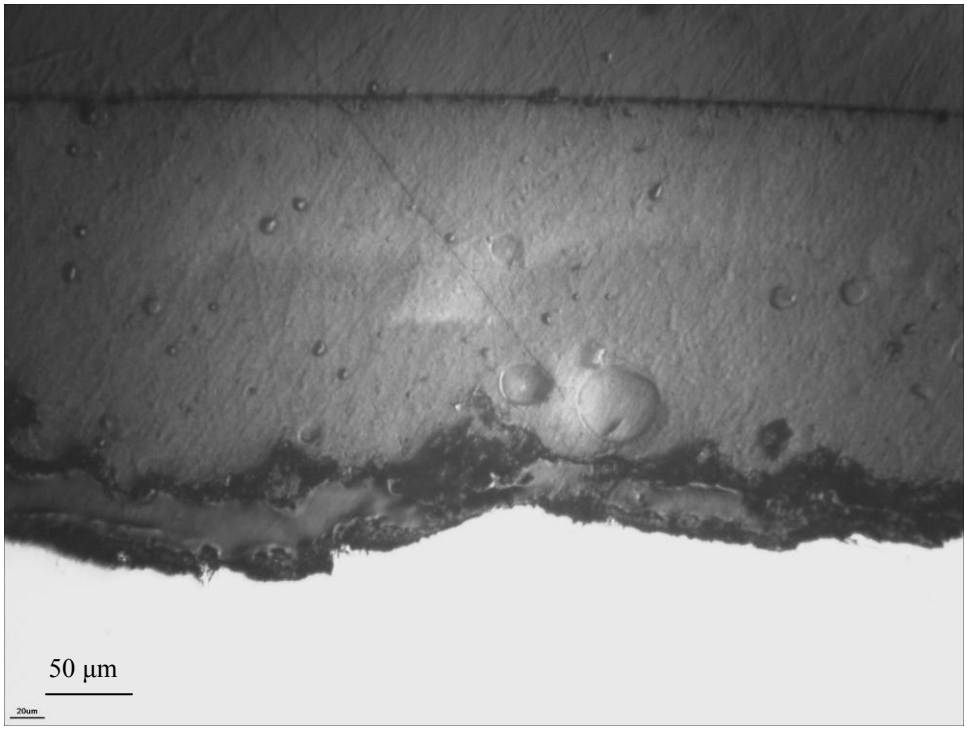

Figure 127: YG3 off defect

Appendix 2: (Continued)
-500 mV Chloride

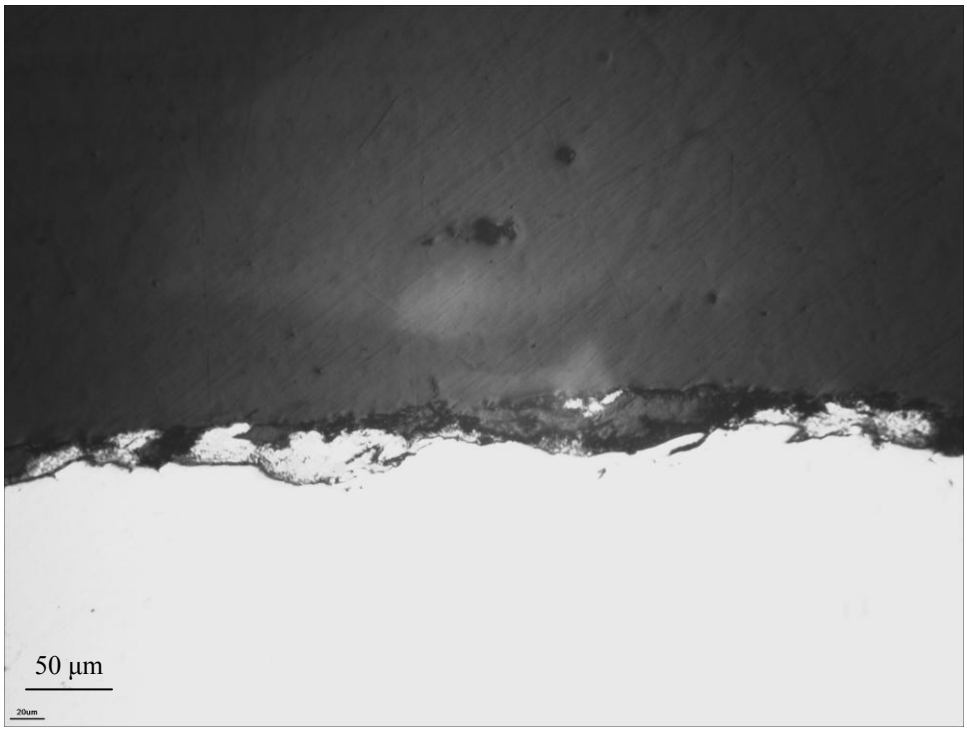

Figure 128: YG11 defect

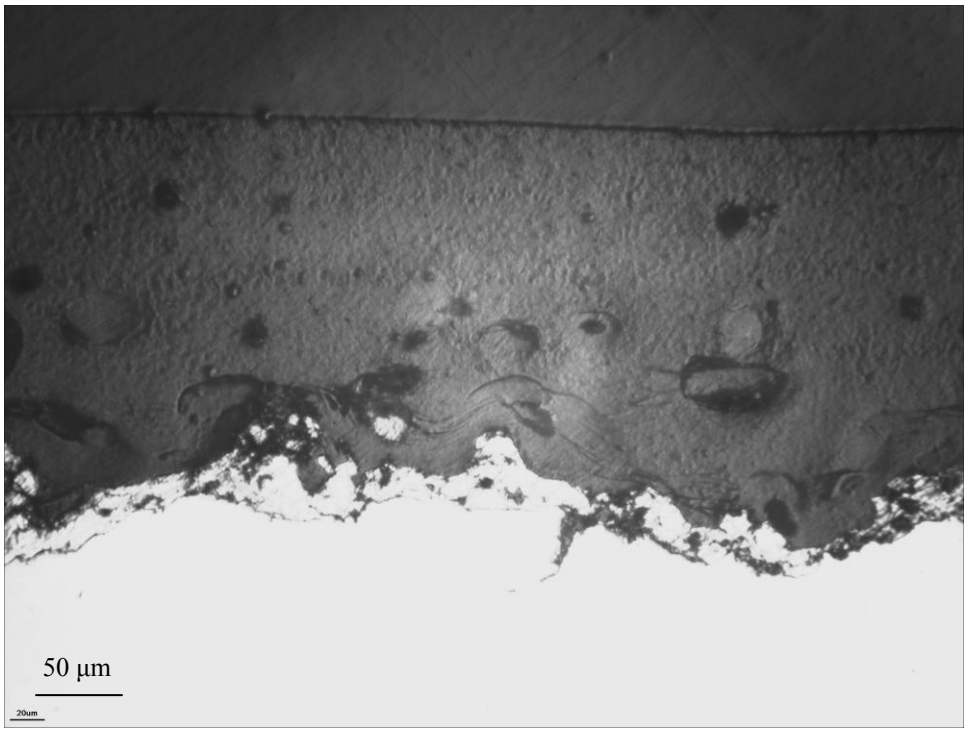

Figure 129: YG11 off defect

Appendix 2: (Continued)
-1000 mV Chloride

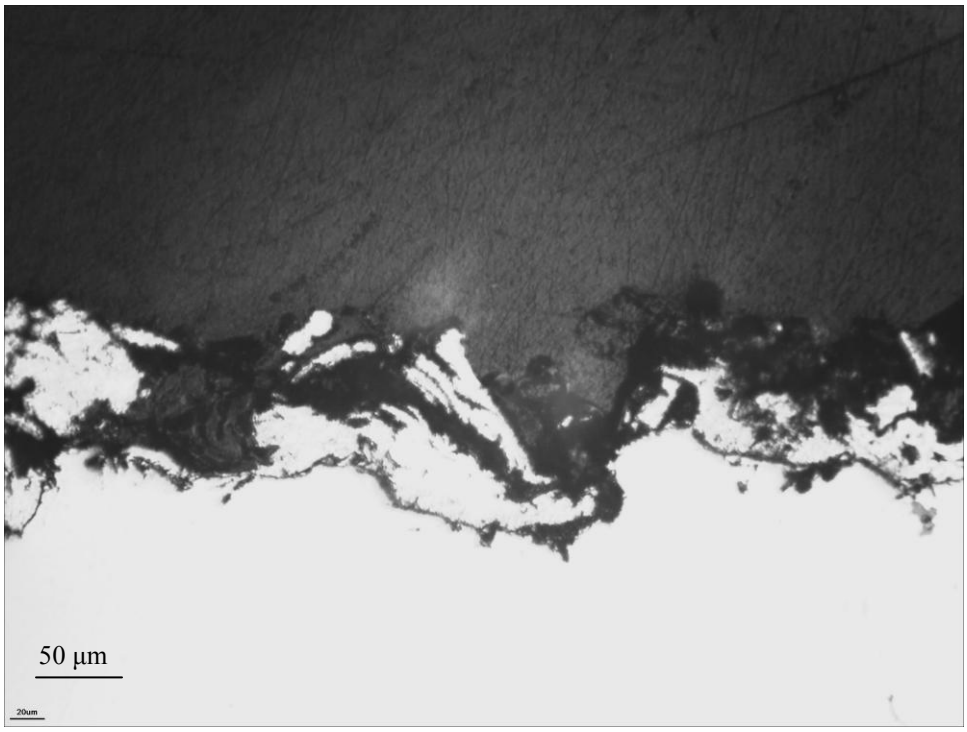

Figure 130: YG8 defect

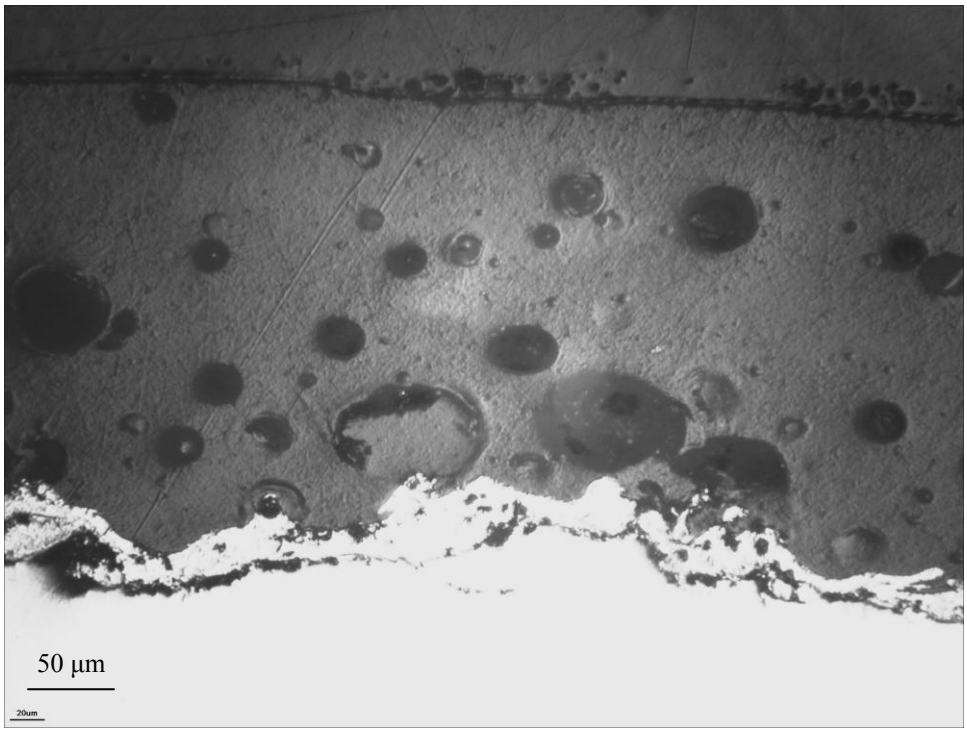

Figure 131: YG8 off defect